Wind stress forcing of the freshwater distribution in the Arctic and North Atlantic Oceans

by

Tamás Kovács

a Thesis submitted in partial fulfillment
of the requirements for the degree of

Doctor of Philosophy
in Geosciences

Approved Dissertation Committee

Prof. Dr. Rüdiger Gerdes
(Jacobs University Bremen; Alfred Wegener Institute)

Prof. Dr. Joachim Vogt
(Jacobs University Bremen)

Prof. Dr. Gerrit Lohmann
(Alfred Wegener Institute)

Dr. Michael Karcher
(Alfred Wegener Institute)

Dr. Benjamin Rabe
(Alfred Wegener Institute)

Date of Defense: November 18, 2019

Department of Physics & Earth Sciences

Statutory Declaration

Family Name, Given/First Name	Kovács, Tamás
Matriculation Number	20331752
Kind of thesis submitted	PhD-Thesis

English: Declaration of Authorship

I hereby declare that the thesis submitted was created and written solely by myself without any external support. Any sources, direct or indirect, are marked as such. I am aware of the fact that the contents of the thesis in digital form may be revised with regard to usage of unauthorized aid as well as whether the whole or parts of it may be identified as plagiarism. I do agree my work to be entered into a database for it to be compared with existing sources, where it will remain in order to enable further comparisons with future theses. This does not grant any rights of reproduction and usage, however.

The Thesis has been written independently and has not been submitted at any other university for the conferral of a PhD degree; neither has the thesis been previously published in full.

German: Erklärung der Autorenschaft (Urheberschaft)

Ich erkläre hiermit, dass die vorliegende Arbeit ohne fremde Hilfe ausschließlich von mir erstellt und geschrieben worden ist. Jedwede verwendeten Quellen, direkter oder indirekter Art, sind als solche kenntlich gemacht worden. Mir ist die Tatsache bewusst, dass der Inhalt der Thesis in digitaler Form geprüft werden kann im Hinblick darauf, ob es sich ganz oder in Teilen um ein Plagiat handelt. Ich bin damit einverstanden, dass meine Arbeit in einer Datenbank eingegeben werden kann, um mit bereits bestehenden Quellen verglichen zu werden und dort auch verbleibt, um mit zukünftigen Arbeiten verglichen werden zu können. Dies berechtigt jedoch nicht zur Verwendung oder Vervielfältigung.

Diese Arbeit wurde in der vorliegenden Form weder einer anderen Prüfungsbehörde vorgelegt noch wurde das Gesamtdokument bisher veröffentlicht.

....

Date, Signature

Abstract

Observations from recent decades suggest an opposing variability between salinity anomalies in the Arctic Ocean and in the Subarctic North Atlantic, often expressed as changes in their freshwater budgets. However, due to the still too short time periods covered by observations, the temporal robustness of this covariability remains an open question. Moreover, certain patterns of freshwater variability have been linked to different atmospheric circulation regimes, but the drivers of freshwater redistribution between the two basins are still not completely understood.

The hypothesis of this study was that there is a potential for an oscillating covariability between the freshwater content of the Arctic Ocean and the Subarctic North Atlantic, and the redistribution between their basins is governed by wind stress forcing associated with large-scale patterns of atmospheric variability. In order to test this hypothesis, numerical model simulations were performed with different coupling configurations of the Max Planck Institute Earth System Model (MPI-ESM) with the objectives to 1) analyze the link between Arctic and Subarctic North Atlantic freshwater anomalies, to 2) identify key patterns of atmospheric variability that govern these anomalies through wind forcing, and to 3) explain the physical mechanisms of coupling between freshwater and near-surface winds associated with these key patterns.

The results showed that even though there is a stable sign of freshwater redistribution between the Arctic and the Subarctic North Atlantic on a multidecadal time scale, this sign is mostly obscured by large anomalies in the North Atlantic that are transported from the south, and are not directly related to the freshwater exchange with the Arctic Ocean. This suggests that the observed anticorrelation is not likely to persist in the future, but can possibly occur again for a period of a few decades.

A comprehensive statistical analysis revealed that although the Arctic Oscillation or the North Atlantic Oscillation describe the main statistical modes of the large-scale atmospheric variability, they do not represent those modes that are best connected to freshwater anomalies. Such modes were identified in this work by performing a redundancy analysis of atmospheric variability and freshwater content, separately for its liquid and solid components.

The impact of wind stress forcing was demonstrated by further simulations. These used prescribed wind data based on observations, but unlike the otherwise identically set-up unconstrained fully coupled runs, they could reproduce the observed freshwater anomalies of the 1990s. This confirmed the key role of wind stress forcing. Additional experiments with prescribed idealized wind perturbations enabled the isolation of the effect of certain wind forcing patterns on freshwater variability. The results showed that liquid freshwater is accumulated in (released from) the Beaufort Gyre that inflates (deflates) due to Ekman dynamics driven by an overlying anticyclonic (cyclonic) wind regime. Changes in this wind regime over the Canada Basin were also found to affect Arctic sea ice distribution, favoring the accessibility of either the Northeast or the Northwest Passage against the other, but did not result in anomalous export of freshwater into the Subarctic North Atlantic. This is suspected to be driven rather by the local cyclonic wind system over the Greenland Sea, but the simulated linear response to perturbations of its strength was unclear and inconsistent. Only in the Nordic Seas could a robust response be evaluated, where an overlying anticyclonic wind anomaly leads to a significant increase in the extent and volume of sea ice.

Table of Contents

x

1. Introduction

The structure of this thesis is centered around the presentation of results that are shown in three different chapters where they are discussed and summarized separately. These are framed by further chapters providing a general introduction and a final collective summary.

Chapter 1 gives a broad overview of the main characteristics of the Arctic and North Atlantic Oceans, and provides a detailed description of their sea ice cover and salinity distribution by introducing the measure of *freshwater content*. After reviewing the current state of the art in its research, Chapter 2 identifies key knowledge gaps in freshwater variability and its atmospheric momentum forcing, and states the main objectives of this study. These are followed by the introduction of the methods, including the description of the applied numerical model and the experiment design.

Chapters 3–5 present the results, separated according to the three main objectives of this study. Chapter 6 summarizes the main findings of this thesis, and gives suggestions for future studies that could further deepen our understanding of the freshwater variability in the Arctic and North Atlantic Oceans, its driving forces and its possible atmospheric feedbacks.

1.1. Main Characteristics of The Arctic and North Atlantic Oceans

The northern polar region of Earth is mostly covered by a large water body enclosed by continents from almost all sides. This mediterranean sea is bordered by the Bering Strait from the Pacific and by the Davis Strait and the Greenland-Scotland Ridge from the Atlantic Ocean, and is often referred to as the Arctic Mediterranean. As described by Sverdrup et al. (1942), this term includes the waters of the Canadian Arctic Archipelago and Baffin Bay, as well as the Nordic Seas (a collective name for the Greenland, Iceland, and Norwegian Seas) in addition to the Arctic Ocean. Although this is considerably smaller than the definition given by the International Hydrographic Organization that includes even the Hudson Bay as part of the Arctic Ocean (IHO, 2002), this study follows its nomenclature, and considers the Arctic Ocean as the waters bounded by the Bering Strait, the Canadian Arctic Archipelago, Fram Strait, and the Barents Sea Opening.

The Subpolar North Atlantic Ocean in this study means the waters between America and Europe, bounded by the Canadian Arctic Archipelago and the Greenland-Scotland Ridge on the north, and the 50°N latitude on the south, and thus it includes the Hudson and Baffin Bays, but not the Nordic Seas. For the analysis of freshwater content and fluxes this study also uses the term Subarctic North Atlantic. This domain consists of the Subpolar North Atlantic Ocean, and the Nordic Seas and the North Sea and the Baltic Sea as well.

1.1.1. Bathymetry

The Arctic Ocean is the smallest and shallowest of the world oceans. Its bathymetry, along with the nomenclature of its most prominent features is presented on Figure 1.1. The basin of the Arctic Ocean covers an area of roughly 9.4 million km^2 and consists of the deep Arctic Basin, and shelf areas not deeper than 300 meters. These shelf seas are the Barents Sea, the Kara Sea, the Laptev Sea, the East Siberian Sea, and the Chukchi Sea. The deep basin is divided into the Eurasian Basin and the Canadian or Amerasian Basin by the Lomonosov Ridge, an underwater ridge that crosses the Arctic with a highest point at 1600 meters below sea level. The Eurasian Basin is further separated by the Gakkel Ridge into the 4000 meters deep Nansen Basin and the 4500 meters deep Amundsen Basin. The Amerasian Basin is also divided into two parts by the Alpha Ridge and the Mendeleyev Ridge. These are the Makarov Basin with a maximum depth of 4000 meters, and the Canada Basin, the largest and shallowest basin with a maximum depth of 3800 meters (Rudels, 2009).

The Arctic Ocean is mostly enclosed by continents and has a limited connection to other oceans. It is connected to the Pacific Ocean through the shallow (50 m) and narrow (85 km) Bering Strait. The connection to the Atlantic Ocean is through the Canadian Archipelago west of Greenland linking the Arctic Ocean to Baffin Bay and to the North Atlantic Ocean through Davis Strait (1030 m deep, 330 km wide). East of Greenland, it is connected to the Nordic Seas through the much deeper (2600 m) and wider (580 km) Fram Strait and the Barents Sea Opening (480 m deep, 820 km wide). Through these gates the Arctic Ocean exchanges water (and ice) with the world oceans (Haine et al., 2015).

The domain of the Nordic Seas is part of the Arctic Mediterranean, and is situated east of Greenland between the Arctic Ocean and the Subpolar North Atlantic Ocean (Figure 1.1). It is separated from the Arctic Ocean by the Fram Strait between Greenland and Svalbard, and by the Barents Sea Opening between Svalbard and Scandinavia. The Nordic Seas comprise the Greenland Sea, the Iceland Sea, and the Norwegian Sea, covering a total area of 2.5 million km^2 (Drange et al., 2005). Its deepest point, about 4800 meters underwater is located in the Greenland Sea, although on average the Norwegian Sea is the deepest, with a mean depth of about 2000 meters. The Iceland Sea is

the smallest and shallowest part of the Nordic Seas. On the south, the Nordic Seas are bound by the shallow waters of the North Sea, and on the southwest by the Greenland-Scotland Ridge that forms a natural barrier between the Nordic Seas and the Subpolar North Atlantic Ocean (Blindheim and Østerhus, 2005).
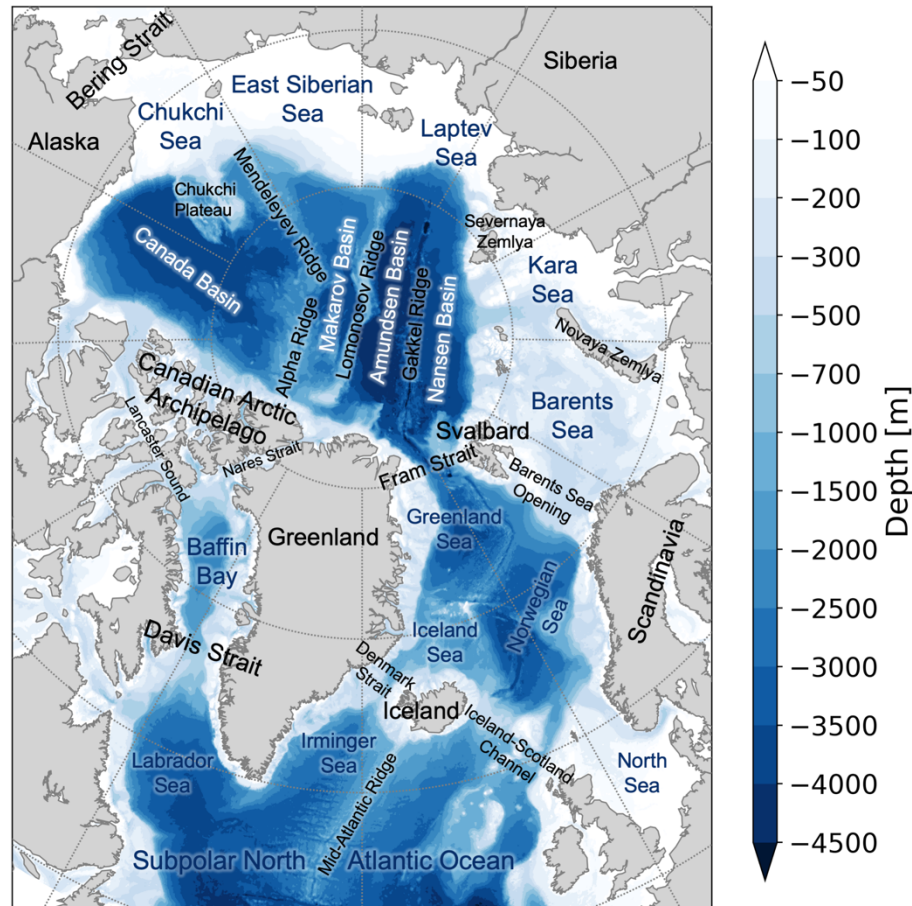

Figure 1.1. The Arctic Mediterranean and the Subpolar North Atlantic. Bathymetry data is from ETOPO1 Global Relief Model (Amante and Eakins, 2009).

The Atlantic Ocean is the second largest ocean enclosed between the American continents from the west, and Europe and Africa from the east. It is open to the south to the Southern Ocean, while in the north it is connected to the Arctic Ocean through several straits. Here focus is on its northern subpolar part and on the complex system it forms with the Arctic Ocean. The main features of its bathymetry can be seen on Figure 1.1.

The long basin of the Atlantic Ocean is divided into a western and eastern part by the Mid-Atlantic Ridge situated about 2000 meters underwater, following the border between divergent tectonic plates. The highest point of this ridge reaches a depth of 1000 meters. It acts as a divider between the deep basins on either sides, and therefore has a significant effect on the circulation of deeper waters. Both the western and the eastern basins have a depth of around 4–5000 meters, but they are shallower at higher latitudes, where their marginal seas are located. The Labrador Sea is situated in the northwest, connecting the

North Atlantic Ocean to the Arctic through Baffin Bay. It is more than 3000 m deep in the south and becomes shallower as it narrows towards Davis Strait. On the eastern side of Greenland is the Irminger Sea, bordered by Greenland, Iceland, and the northern part of the Mid-Atlantic Ridge called the Reykjanes Ridge. On the northeast the North Atlantic Ocean is open to the Nordic Seas through the Greenland-Scotland Ridge. The opening between Greenland and Iceland is called the Denmark Strait, and it has a sill depth of approximately 600 meters. The water is somewhat shallower between Iceland and the Faroe Islands (400 m), and deeper in the Faroe Bank Channel (800 m), between the Faroe Islands and Scotland.

1.1.2. Main Currents

Most of the water in the Arctic Ocean is of Atlantic origin, especially the mid-depth and deep waters, but a substantial part of the water in the Amerasian Basin also comes from the Pacific Ocean. This is possible due to a network of currents transporting large volumes of water at different depths. The main surface currents of the Arctic Mediterranean and the Subpolar North Atlantic Ocean are shown on Figure 1.2.
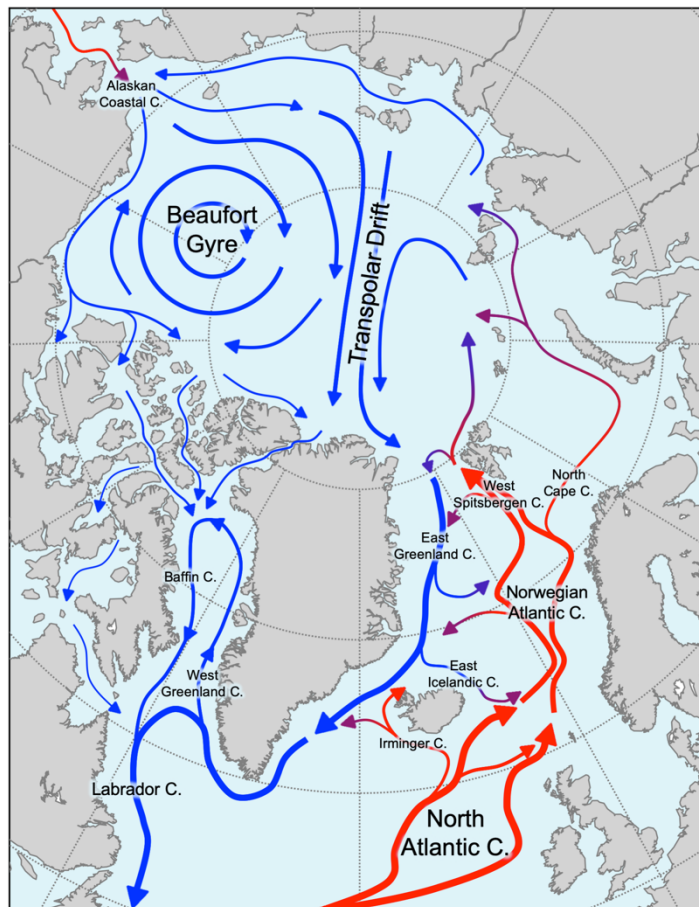

Figure 1.2. *Surface currents in the Arctic Mediterranean and in the Subpolar North Atlantic Ocean.*

In the North Atlantic Ocean, warm and saline water is transported northwards by the Gulf Stream, a strong western boundary current. Reaching the latitude of about 40°N, it detaches from the American coast and turns eastwards. This part of the stream, called the North Atlantic Current, crosses the Atlantic and transports a large amount of tropical water that is significantly warmer than its surroundings towards Europe. It is characterized by a meandering flow that carries about 20 Sv (Sverdrups; 1 Sv = 10^6 m^3s^{-1}) of water across the Mid-Atlantic Ridge (Rossby, 1996). The North Atlantic Current forms the northern part of the subtropical gyre, a large-scale quasi-permanent anticyclonic circulation at mid-latitudes, mainly in the upper 1000 meters depth range. At the same time, it forms the southern part of the cyclonic subpolar gyre, (Schmitz, 1996).

Flowing towards Europe, the North Atlantic Current gradually weakens as other streams branch from it before it reaches the Nordic Seas. A total amount of about 8 Sv crosses between Greenland and Scotland: 1 Sv carried by the Irminger Current across Denmark Strait, and 7 Sv carried by the North Atlantic Current split between the two parts of the Iceland-Scotland Channel. Altogether, the Faroe-Scotland branch carries almost half of the water into the Nordic Seas, and it is also warmer and more saline than the others; therefore it is the most dominant in terms of Atlantic Water import (Hansen and Østerhus, 2000).

After entering the Nordic Seas, Atlantic Water continues flowing northeast in two branches of the Norwegian Atlantic Current. Part of the eastern branch crosses the Barents Sea Opening, carrying about 2 Sv of Atlantic Water into the Arctic Ocean, where it continues as the North Cape Current (Skagseth, 2008). The rest of the eastern branch flows northwards and joins the western branch that also loses water to westward recirculating branches in the Iceland and Greenland Seas. By the time it reaches Fram Strait, the amount of Atlantic Water carried by the West Spitsbergen Current is about 3 Sv, roughly half or third of the total water flux of the current (Beszczynska-Möller et al., 2012).

Part of the Atlantic water crossing Fram Strait also recirculates westwards and joins the East Greenland Current, while most of it enters the Arctic Ocean. This warm and relatively saline surface water cools and freshens as it encounters and melts sea ice, and flows eastwards along the continental slope. It sinks underneath the cold and fresher surface water there, and continues its way northeast while joining with part of the water entering from the Barents Sea Opening that also goes through sinking as it becomes denser due to heat loss to the atmosphere and brine rejection during ice formation in winter. Flowing further eastwards, these waters of Atlantic origin spread to large depths and reach the lower regions of the entire Arctic Basin, ultimately penetrating both the Eurasian and the Amerasian Basins (Jones, 2001; Rudels, 2009).

There is also a significant inflow of water crossing the Bering Strait, where about 1 Sv of Pacific Water enters the Arctic Ocean through the Chukchi Sea (Woodgate, 2018). This water is relatively fresh, especially in comparison with Atlantic Water, therefore it mostly

stays closer to the surface, as it continues to flow in multiple directions. Part of it enters the East Siberian Sea, its central branches penetrate the Amerasian Basin, while its easternmost part flows along the American continent as the Alaskan Coastal Current (Rudels, 2009).

The central Arctic Ocean has two main features of water flow on the surface, namely the Beaufort Gyre and the Transpolar Drift. The Beaufort Gyre is a large anticyclonic circulation cell in the Canada Basin, whose strength and extent varies greatly, as it is driven by wind forcing associated with an atmospheric pressure pattern that is dominated by alternating regimes. (Proshutinsky and Johnson, 1997). The Transpolar Drift is a surface current that transports water from the Siberian shelf seas across the Arctic towards Greenland and Fram Strait. It is also mainly wind-driven, and shows similarly large variations in its position and strength associated with patterns of atmospheric variability (Mysak, 2001). The role of atmospheric forcing is presented in detail in Chapter 1.2.3—Atmospheric Forcing as a Driver of Freshwater Anomalies. The flow in the deeper layers of the Arctic Ocean is characterized by cyclonic circulation cells in the four deep basins.

Balancing the inflow of Atlantic and Pacific Water, there is also a southward export of cold and relatively fresh Arctic Water into the Nordic Seas and the North Atlantic Ocean. Most of the water that crosses the Arctic along the Transpolar Drift is carried into the Nordic Seas by the East Greenland Current, a strong western boundary current that transports about 11 Sv of water southwards through Fram Strait (Marnela et al., 2013). In addition to this outflow, there is also a significant export of sea ice to lower latitudes. This is discussed in Chapter 1.2—Freshwater Content and Fluxes. The top layers (down to 200 meters depth) of the East Greenland Current comprise predominantly fresh and cold Arctic Water, but at intermediate depths (200–1000 m) it carries recirculating Atlantic Water (Rudels et al., 2005). As it flows southwards, some part of it repeatedly recirculates to the east in branches in the Greenland Sea and in the Iceland Sea that are ultimately entrained in the West Spitsbergen and Norwegian Atlantic Currents. However, most of the water continues to flow southwards and enters the North Atlantic Ocean as an outflow in the top layers of about 1.3 Sv across Denmark Strait, and also as an overflow of intermediate waters of about 3-3 Sv respectively across Denmark Strait and the Iceland-Scotland Channel (Hansen and Østerhus, 2000). The East Greenland Current then continues to flow southwards until it rounds the southern tip of Greenland. There it follows the shore and turns northwards as the West Greenland Current, most of which branches westwards, while some of it continues flowing into the Baffin Bay. Here it meets Artic Water exported through the Canadian Arctic Archipelago.

Water from the Arctic Ocean that is primarily of Atlantic origin is exported through Fram Strait (and a much smaller amount through the Barents Sea Opening), while most the water of Pacific origin leaves the Arctic Ocean through the narrow and shallow

pathways across the Canadian Arctic Archipelago. The major pathways are the Nares Strait and Lancaster Sound, where fluxes are generally difficult to measure due to the harsh conditions of their remote locations. The volume flux across Nares Strait varies between 0.7–1.0 Sv, depending on the mobility of the ice cover (Münchow, 2015). The mean transport across Lancaster Sound is about 0.5–0.7 Sv (Prinsenberg et al., 2009; Peterson et al., 2012). These, and also water from the recirculating West Greenland Current join in the Baffin Current, and flow southwards. By the time it reaches Davis Strait, this volume flux is about 1.6 Sv (Curry et al., 2014). Flowing southwards, the Baffin Current joins with the water of the West Greenland Current, and continues to flow southwards along the North American coast as the Labrador Current. After passing Newfoundland it continues to flow along the shore, while a part of it recirculates and gets entrained in the North Atlantic Current to begin its journey across the Atlantic towards the Arctic Ocean across the Nordic Seas.

1.1.3. Hydrography

The Arctic Ocean has a relatively low salinity in comparison with other oceans. This is a result of multiple sources low salinity water, or freshwater. Continental runoff from surrounding land surfaces contributes significantly to the freshness of the Arctic Ocean, since its upper layer accounts for 0.1% of the global ocean volume but receives 11% of global river discharge (Fichot et al., 2013). The inflow through Bering Strait is also relatively fresh. Moreover, in the Arctic the amount of precipitation exceeds evaporation, resulting in a net inflow of freshwater over the entire Arctic Ocean (Aagaard and Carmack, 1989).

In their fundamental study on Arctic salinity balance, Aagaard and Carmack (1989) estimated the mean salinity of the Arctic Ocean as 34.8. This value is widely accepted and used in the literature as a reference (Serreze et al., 2006). However, for a detailed investigation, the regional and vertical differences must also be considered. According to the PHC3.0 climatology of Steele et al. (2001), the largest spatial differences are observed at the surface. Excluding the immediate vicinity of major river mouths, where the surface can be almost completely fresh, the Arctic Ocean has a surface salinity between 29.5 and 35, but some of the Siberian shelf seas are even fresher. In general, the Amerasian Basin has lower surface salinity (29.5–31) than the Eurasian Basin (31–34.5), as its surface water is mostly of Pacific origin, while the latter is dominated by the inflow of high salinity Atlantic Water. The highest surface salinity is present in the Barents Sea, where its value can reach 35.

The Arctic Ocean is strongly stratified, and its water mass shows different characteristics at different depths. Rudels (2009) distinguishes five separate layers of Arctic Water:

- The Polar Mixed Layer is a 50 meters thick layer with low salinity (Amerasian Basin: 30–32, Eurasian Basin: 32–34). This upper layer is homogenized during winter by freezing, brine release and haline convection, while in summer the upper 10–20 m becomes freshened and stratified through dilution by sea ice meltwater. If forms the Polar Surface Water together with the halocline below.

- The halocline is 100–250 meters thick (thicker in the Amerasian Basin, thinner in the Eurasian Basin), and is characterized by a strong vertical gradient of salinity (32.5–34.5). Its temperature is close to freezing.

- The layer of Atlantic Water below the halocline is 400–700 meters thick with a salinity between 34.5 and 35, and a potential temperature above 0°C.

- The Intermediate Water in the deeper regions which can still cross the Lomonosov Ridge with a salinity between 34.87 and 34.92, and a potential temperature between -0.5 and 0°C.

- The deep and bottom waters fill the deepest basins. These are also of Atlantic origin, and have a salinity of between 34.92 and 34.96 and a potential temperature between -0.55 and -0.5°C in the Amerasian Basin. The typical values for the Eurasian Basin are 34.92–34.945 and -0.97– -0.5°C.

The surface waters of the Nordic Seas region are characterized by large salinity and temperature differences associated with the flow of warm and salty Atlantic Water in the southeast, and cold and fresh water exported from the Arctic along the coast of Greenland in the west. The typical surface salinity is between 32 and 35.2, with the higher values in the Norwegian Sea, and the lower values in the Greenland Sea, where the westernmost part of the East Greenland Current is even fresher than 30 near the coast. The surface temperature shows a similar pattern, with higher values up to 10°C in the southeast, and below 0°C in the northwest (PHC3.0 climatology of Steele et al. (2001)).

Atlantic Water entering the Nordic Seas through the Greenland-Scotland Channel fills some of the Iceland Sea and much of the Norwegian Sea down to a depth of about 500 meters. This Atlantic Water has a potential temperature between 7 and 10.5°C, and a salinity between 35.1 and 35.45. This water continues to flow northwards, while some of it recirculates in the Iceland and Greenland Seas, where it is situated below the top layers of cold and fresh waters of Arctic origin that have similar properties as the Polar Surface Water. From the Arctic there is also an export of deep water through Fram Strait at the depths of 1500–2500 meters. It has a potential temperature between -0.5 and -0.9°C, and a

salinity of 34.92–34.93, depending on whether it is coming from the Amerasian or the Eurasian Basin. But this is only one source of the intermediate and deep waters of the Nordic Seas, as there is also a local formation of deep water in the Greenland and Iceland Seas. Mixing together with the deep waters from the Arctic, this deep water in the Greenland Sea has a potential temperature below 0°C and salinity of 34.88–34.90. These deep waters then also fill the other deep basins of the Nordic Seas (Blindheim and Østerhus, 2005).

Deep water is formed locally in the Nordic Seas, which makes the Nordic Seas a key region for the global ocean circulation (Rudels and Quadfasel, 1991). Normally, the strong density gradients do not permit the vertical exchange of water in the ocean, thus insulating the deep ocean from the surface. Only in shelf areas at high latitudes, where the density can increase due to heat loss to the atmosphere and brine rejection during ice formation, can surface water sink to lower depths. However, there is another process, called open ocean convection. This can happen in weakly stratified water that is exposed to buoyancy loss to the atmosphere, and is characterized by a cyclonic circulation pattern that results in the doming of isopycnals. This favors the rising of weakly stratified underlying water to the surface. There it is readily exposed to intense surface forcing that in winter can significantly lower its temperature. This increases its density, so that it sinks, feeding a cycle of convection that can reach depths greater than 2000 meters (Marshall and Schott, 1999). In the Nordic Seas all the above conditions are met, and convection takes place in the Greenland and Iceland Seas. This forms deep water, which then spreads to great distances, filling the deep basins of the Arctic Ocean, and also ventilating the North Atlantic (Aagaard et al., 1985). Besides the Nordic Seas, the only location in the Northern Hemisphere where deep water formation takes place is the Labrador Sea in the North Atlantic.

The Subpolar North Atlantic Ocean is characterized by an east-west gradient of surface salinity and temperature due to the dominance of the warm and salty North Atlantic Current in the east and the cold and fresh Labrador Current in the west. Therefore, both surface salinity and temperature are lower in the western basin, where near the coast along the Labrador Current they can be lower than 32 and 2°C, respectively. The values quickly increase off the shore, and the typical values in the open western basin are 34–35 for salinity, and 4–9°C for temperature. In the eastern basin the surface salinity reaches 35.4 and the temperature reaches 13°C close to Ireland (PHC3.0 climatology of Steele et al. (2001)).

1.1.4. Sea Ice

The polar regions of the Earth are exposed to harsh conditions, including extremely low temperatures. At high latitudes, cold air causes the sea surface to freeze, creating a layer

of sea ice that forms at the boundary of ocean and atmosphere. Sea ice can grow to a thickness of multiple meters, and covers part of the Arctic Ocean throughout the year. Its physical properties differ from those of water, therefore it plays an important role as a mediator that can influence the interactions between ocean and atmosphere.

Ice forms when the water temperature reaches its freezing point. In clear, fresh water this is at 0°C, but in seawater with a salinity of 32, which is typical for the surface layers in the polar regions, freezing starts at -1.8°C. The ice that forms has lower salinity; while seawater freezes, most of the salt in it is rejected, leaving behind water with a high salt concentration called brine. Some salt does get trapped in the forming ice, but it gradually drains over time. Therefore, the mean salinity of younger (0.5 m thick) sea ice is around 7, and thicker multi-year Arctic ice has a salinity of about 3 (Cox and Weeks, 1974). Sea ice floats on the water surface and can drift to large distances driven by ocean currents and the wind (see Chapter 1.2.3.1—Wind Stress). When the ice melts, the meltwater is much fresher and thus lighter than the water from which the ice formed. This means that it stays on the surface, insulated from deeper waters by a strong halocline. This explains the strong stratification in the Arctic Ocean, where sea ice is forming and melting following the seasonal cycles.

The extent of sea ice, which is the area with at least 15% of ice concentration, exhibits a strong seasonal variability. This can be seen on Figure 1.3 which presents the mean ice extent of the winter maximum (blue line) and the summer minimum (orange line) in the Arctic and the North Atlantic Ocean during the period 1979–2000. In winter, sea ice covers almost the entirety of the Arctic Ocean, with the exception of a large part of the Barents Sea. There is an extensive sea ice cover in the Nordic Seas, mostly along the pathway of the Arctic sea ice export following the East Greenland Current. This can extend as far south as the southern tip of Greenland. Baffin Bay is also completely frozen over in winter, and the ice edge is in the Labrador Sea, and even further south along the continent where the cold Labrador Current dominates. In summer, most of the sea ice outside the Arctic Ocean melts. Only in the Canadian Arctic Archipelago and in the western Greenland Sea some ice remains. Within the Arctic Ocean, the ice also melts along the continents and in some of the shelf seas, while the central Arctic has a permanent, year-round ice cover. Due to the lack of seasonal melt, this ice is thicker, as it can be seen on Figure 1.3 that also shows the mean sea ice thickness for March in the period 2011–2017. The thickest ice is observed north of the Canadian Arctic Archipelago and Greenland, where it extends to 3.5 meters, but a large part of the central Arctic has an ice cover thicker than 2 meters. In the shelf seas the typical maximum thickness is 1–1.5 meters, except for the Kara Sea (0.5–1 m) and the Barents Sea which is mostly ice-free even in winter. The ice exported through Fram Strait contains a large amount of multiyear ice, therefore the mean thickness is rather high (up to above 3 m) along the East Greenland Current. In other lower latitude seas, the thickness usually does not exceed 1 meter.
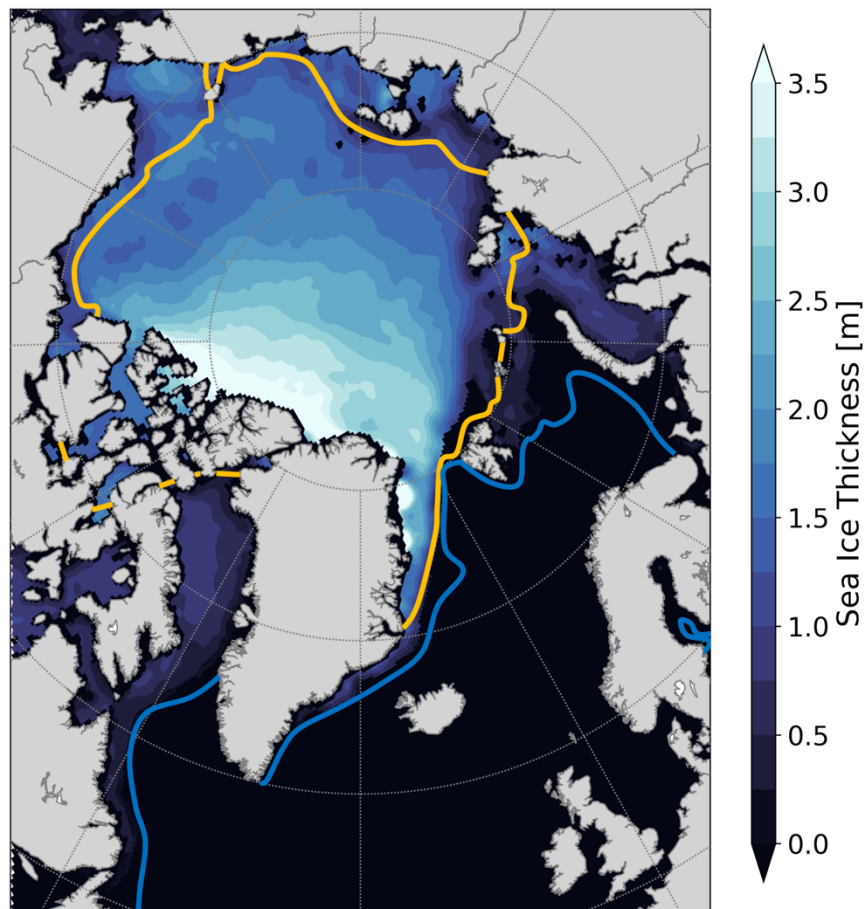
Figure 1.3. *Arctic and North Atlantic sea ice cover. The lines contour the average winter maximum (blue) and summer minimum (orange) extent of sea ice during the period 1979–2000 based on data from the National Snow and Ice Data Center. The map shows average March sea ice thickness during the period 2011–2017 based on CryoSat-2/SMOS data downloaded from www.meereisportal.de (Grosfeld et al., 2016).*

The seasonal changes and time series of sea ice extent in the Northern Hemisphere are plotted on Figure 1.4. The large seasonality is clearly visible on the left panel, as the maximum extent in March (almost 16 million km^2) is twice the size of the September minimum (7.3 million km^2). The right-side panel depicts temporal changes of the March maximum and the September minimum from 1979 until 2016. Both show a decreasing trend that is also stronger in the last two decades than before. The summer extent has been declining at a higher rate than the winter extent. Overall, observations show that Arctic sea ice is retreating, with less ice forming in winter, and more ice melting during summer, as the same reduction has been observed for the ice thickness and thus the total volume of the ice (Kwok et al., 2009).
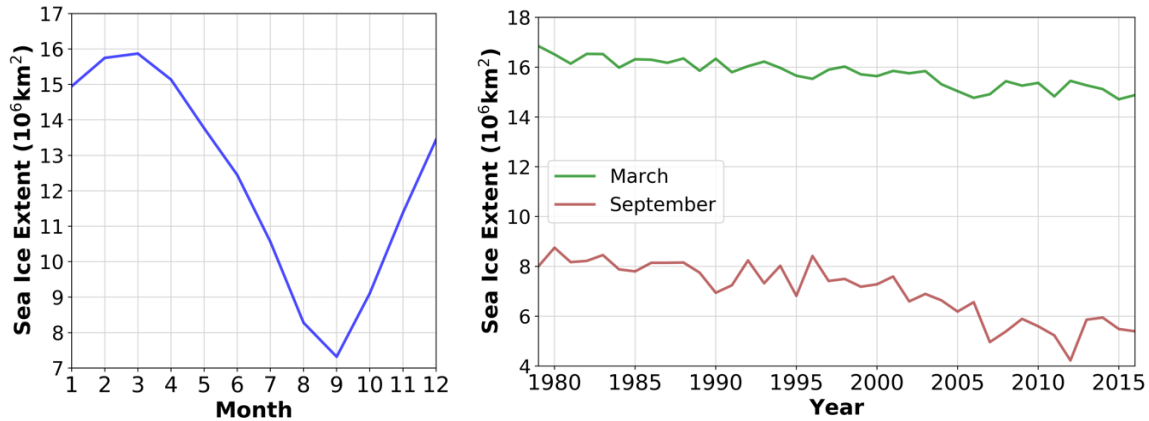
Figure 1.4. *Sea Ice Extent in the Northern Hemisphere. Left: seasonal cycle averaged over 1979–2010. Right: time series of March and September means. Data is based on EUMETSAT OSI SAF ice concentration (Tonboe et al., 2016).*

The strong seasonal cycle of sea ice influences the salinity of the upper water layers as the process of freezing extracts freshwater from the ocean, while the melting provides a source of it. Sea ice can drift to great distances and can melt in a different region than where it was formed, thus it also plays an important role as a freshwater vector in the ocean. The following chapter introduces the concept of oceanic *freshwater content*, and reviews the state of the art of its research in the Arctic and North Atlantic Oceans.

1.2.   Freshwater Content and Fluxes

The salinity of a water solution can be modified by adding or subtracting either salt or water. In the world oceans the total amount of salt varies very little and only very slowly, and therefore can be considered constant even on millennial time scales. Although the total volume of water can change faster by the build-up and melt of great ice sheets during glacial and interglacial periods, they can be ignored here as this study investigates variability in decadal time scales, over which these processes are not significant. On decadal time scales the total volume of water is also very stable due to a global balance of sources (river runoff and precipitation) and sinks (evaporation). However, on a regional scale these are often not balanced.

In the North Atlantic Ocean evaporation exceeds precipitation, removing freshwater and thus increasing salinity. In the Arctic Ocean it is the other way around; river runoff and precipitation supply much more freshwater than what is removed by evaporation, contributing to a low salinity. These differences are somewhat balanced by the exchange of water. The transport of Atlantic Water brings saltier water into the Arctic Ocean, from where fresher Arctic Water is exported to the North Atlantic. Local variations in the salinity, especially in the upper layers, are thus driven by changes associated with river runoff, precipitation, evaporation, oceanic currents—fluxes of water. That is why it is

useful to define a metric for salinity that makes the contribution of these sources and sinks easier to assess. This metric is the oceanic freshwater content.

1.2.1. Concept

The general concept of oceanic freshwater content is that the salinity of a volume of sea water is described by how much freshwater is stored in it, including the amount stored in sea ice. These two phases (liquid and solid freshwater content) are investigated separately in this study, because of the differences in their variability and their driving forces.

Liquid freshwater content is the amount of zero salinity water that is required to reach to observed salinity of a volume of seawater starting from a reference salinity. It is essentially an alternate metric for salinity, and does not assume a body of actual freshwater within the seawater, but illustrates how much fresher or saltier the sample of seawater is compared to a reference salinity. Freshwater content can also be negative, when the sample is saltier than the reference. It is a useful metric because freshwater anomalies have a very limited effect on the mean salinity even locally, but they play an important role in a wide range of physical and biogeochemical processes in the ocean with local and global consequences. A few examples are stratification, vertical mixing, deep convection, ocean heat flux, sea ice formation, and also nutrient supply, primary production, ocean acidification (Carmack et al., 2016).

Liquid freshwater content ($LFWC$) in a volume of water with a surface A and depth z can be calculated according to the following formula:

$$LFWC = \oint \int_{z=0\,m}^{h} \frac{S_{ref} - S}{S_{ref}} dz\, dA \tag{1.1}$$

where the vertical integration is from the surface ($z = 0$ m) down to depth level h, S is the observed salinity, and S_{ref} is the reference salinity. Similarly, the freshwater flux ($LFWF$) across an oceanic section A is defined as the equivalent flux of zero salinity water, and is given by

$$LFWF = \int v \frac{S_{ref} - S}{S_{ref}} dA \tag{1.2}$$

where v is the velocity component normal to the section A.

As it is apparent from both Equations (1.1) and (1.2), the value of freshwater content and flux depend on the choice of h and S_{ref}. While calculating the freshwater content, h is usually selected as the depth where $S = S_{ref}$., therefore the integration in the vertical is done in the upper layers where the salinity is lower than the reference. In this case the

freshwater content is non-negative. Another common value for h is the full depth of the water column. In this case the freshwater content can be negative as well, when $S > S_{ref}$ in a large part of the water column. The choice of S_{ref} affects both the freshwater content and fluxes as well. In their fundamental study of Arctic freshwater content, Aagaard and Carmack (1989) used $S_{ref} = 34.8$ based on an approximate value of mean Arctic salinity. This is the most commonly used reference (Serreze et al., 2006), although there are studies that use different values for the freshwater content, such as for example 35.0 (Rabe et al., 2014) and for the fluxes, for example 34.9 (Holfort and Meincke, 2005) or 35.2 (Dickson et al., 2007).

The impact of the applied reference salinity is particularly important for the calculation of freshwater fluxes. According to Tsubouchi et al. (2012), the ideal choice is to use a reference salinity that equals to the mean salinity of the investigated ocean basin. Although an arbitrary S_{ref} in the denominator of Eq. (1.2) violates the conservation of mass, this leads to an insignificant error while calculating the total net flux for an enclosed region. This is because when all the boundaries are considered in the integration, an underestimation in one direction is compensated by an overestimation in another direction. In this case, the range of error in the total net freshwater flux arising from using different reference values (within reasonable limits, for example $34.8 < S_{ref} < 35.2$) is within 1%, and therefore can be ignored. But as pointed out by Tsubouchi et al. (2012), there is no compensation for the error when a single freshwater flux is calculated across a section, and in that case reference salinity must be chosen with care. The ideal choice is the mean salinity of the investigated flux, which varies from section to section.

The amount of freshwater stored in sea ice is referred to as solid freshwater content. Its value depends on the volume and the age of the ice, as generally the salinity of frozen seawater is gradually declining over time as it continues to grow (Cox and Weeks, 1974). Likewise, drifting sea ice is considered a solid freshwater flux.

1.2.2. Observed mean values

A complete freshwater budget of the Arctic Ocean is provided by Haine et al. (2015). As they state in their introduction, the global cycle of water in the atmosphere is characterized by a high rate of evaporation in the tropics, a transport of moisture to higher latitudes, and precipitation in the polar regions. This makes the Arctic Ocean a terminus of the atmospheric water circulation, which leads to the accumulation of freshwater.
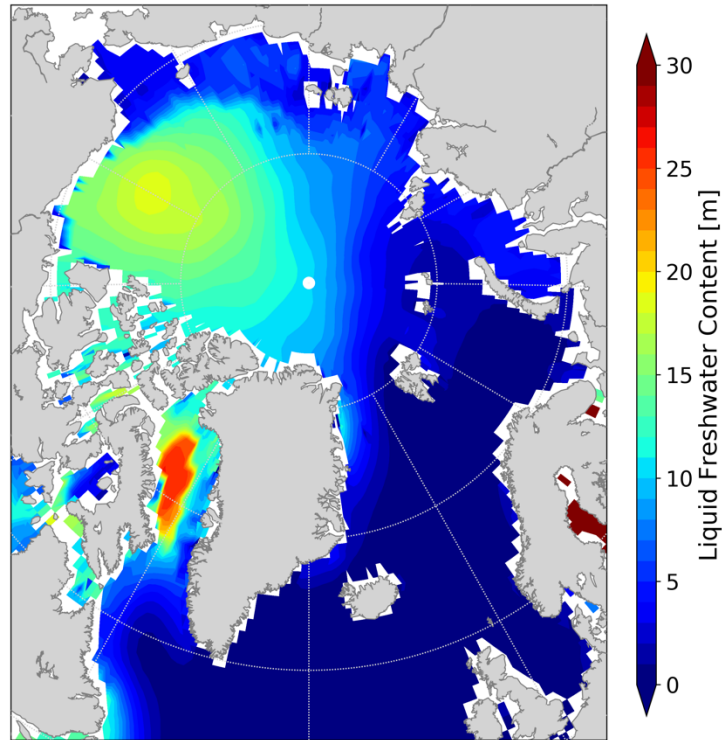
Figure 1.5. *Liquid freshwater content (S_{ref} = 34.8, integrated from surface down to S_{ref}) in the Arctic Ocean and in the Subarctic North Atlantic. Calculated from salinity data from PHC3.0 climatology (Steele et al., 2001).*

The Arctic Ocean (plus Baffin Bay) holds about 93,000 km³ of liquid freshwater relative to a reference salinity of 34.8 (Haine et al., 2015). The spatial distribution of this amount is depicted on Figure 1.5, which shows the thickness of a freshwater layer whose volume is equivalent to the freshwater content integrated in the water column below. Most of the liquid freshwater is stored in the Amerasian Basin, where values reach 18 meters in the Beaufort Gyre, a major reservoir of freshwater. Although their surface salinity is lower, the shelf seas contain much less freshwater due to their shallow depths. There are lower values in the Eurasian Basin too (2–9 m), due to the dominance of high salinity Atlantic Water inflow. Most of the Subarctic North Atlantic contains no freshwater, as the local surface salinity is higher than 34.8. Only along the export pathway of Arctic Water is some freshwater present, for example along the East Greenland Current (2–10 m) and in the coastal regions of the Labrador Sea (3–12 m).

	Mean values for 1980–2000
Freshwater content [km^3]	
Liquid	93,000
Solid	17,800
Net freshwater flux [km^{3}yr^{-1}]	
River runoff	3900 $\pm$ 390
Precipitation - Evaporation	2000 $\pm$ 200
Bering Strait liquid	2400 $\pm$ 300
Bering Strait solid	140 $\pm$ 40
Greenland ice melt	330 $\pm$ 20
Davis Strait liquid	-3200 $\pm$ 320
Davis Strait solid	-160 $\pm$?
Fram Strait liquid	-2700 $\pm$ 530
Fram Strait solid	-2300 $\pm$ 340
Barents Sea Opening	-90 $\pm$ 90
Fury and Hekla straits	-200 $\pm$?
Total fluxes [km^{3}yr^{-1}]	
Inflow sources	8800 $\pm$ 530
Outflow sinks	-8700 $\pm$ 700

Table 1. *Freshwater budget of the Arctic Ocean relative to a reference salinity of 34.8. Negative values indicate southward transport. From Haine et al. (2015).*

The contribution of the solid component (sea ice) in most parts of the Arctic Ocean is smaller. On average there is about 17,800 km^3 of freshwater stored in sea ice (Haine et al., 2015). Assuming an average salinity of 5, the freshwater content of a 1 meter thick ice is 0.76 meters. Considering the typical mean ice thickness of 1–2 meters, this translates to a 0.7–1.5 meters thick layer of freshwater, which is about an order of magnitude smaller than the liquid component.

The individual components of sources and sinks of Arctic freshwater are listed in Table 1. The largest source of freshwater is river runoff, discharging about 3,900 km^3 of freshwater into the Arctic Ocean per year. In the Arctic, precipitation exceeds evaporation; their net rate yields a freshwater supply of 2,000 km^{3}yr^{-1}. Considering the lateral fluxes, the inflow of Pacific Water through Bering Strait carries 2,400 km^{3}of freshwater annually. Together with a few minor components, the total inflow adds up to about 8,800 km^{3}yr^{-1}. Balancing this inflow, there is a significant export of freshwater from the Arctic to lower latitudes, into the Nordic Seas and the North Atlantic Ocean. The largest outflow component is the liquid freshwater flux through Davis Strait, about 3,200 km^{3}yr^{-1}. The solid component in this section is not significant (160 km^{3}yr^{-1}). The other major export pathway is on the eastern side of Greenland, through Fram Strait. Here the liquid component (2,700 km^{3}yr^{-1}) is comparable to that of the Davis Strait, but the total export is

even higher, as Fram Strait is the main gateway for the Arctic sea ice export. Together with the solid component the total freshwater flux is about 5,000 km³yr⁻¹. The sum of freshwater sinks, including those through the Barents Sea Opening and some further minor sections in the Canadian Arctic Archipelago, is about 8,700 km³yr⁻¹.

Comparing the sources and the sinks a dynamic balance is apparent. However, it must be noted that the harsh conditions of the above locations make observations challenging, and in some cases they have considerable uncertainties. Furthermore, all the above freshwater content and fluxes are mean values for the period 1980–2000. As reviewed by Haine et al. (2015), the observational estimates for 2000–2010 show significant changes. This is particularly true for the solid components that show a negative trend due to the gradually shrinking Arctic sea ice cover. River runoff and precipitation are increasing. Recent observations suggest that the sources increased and the sinks decreased in the period of 2000–2010, with a residual of 1,200 km³yr⁻¹ freshening the Arctic Ocean.

In recent decades there has been a growing interest in observing and also modeling the Arctic Ocean freshwater budget, and the anomalies of its components. The variabilities of the system have been the focus of many studies, but there is still much that is not understood. What is the relationship of the Arctic freshwater system to anomalies observed in the Subarctic North Atlantic, its main export target? What are the key physical processes governing Arctic freshwater storage and release? In particular, what are the driving forces of the observed anomalies? The next chapter briefly reviews the state of the art in Arctic and North Atlantic freshwater research with a focus on wind stress forcing associated with large-scale modes of atmospheric variability.

1.2.3. Atmospheric forcing as a driver of freshwater anomalies

1.2.3.1. Wind stress

Air-sea interactions play a critical role in the climate system. Winds with a characteristic horizontal speed two orders of magnitude higher than that of the water surface below exert a strong momentum forcing on the ocean due to friction. This wind stress forcing drives an ocean circulation from local to global scales (Munk, 1950).

During his pioneering Arctic expedition, Nansen (1902) noted that the speed of sea ice drift was 2% of the wind speed, and its direction deviated to the right from the wind direction. Motivated by these observations, Ekman (1905) described the physics of the wind-driven transport near the ocean surface as the effect of wind forcing, ice-water stress, and the Coriolis force. This atmospheric momentum forcing can be estimated by a quadratic drag formula. According to Yang (2006), when wind directly blows over the water, the air-water stress is described by

$$\tau_a = \rho_a C_d |u_{aw}|(u_{aw}) \tag{1.3}$$

where ρ_a is the density of air (1.25 kgm⁻³) and C_d is a drag coefficient (0.00125). The term u_{aw} is the relative velocity between the wind and the water at the surface: $u_{aw} = u_{air} - u_{water}$. As u_{water} is much smaller than u_{air}, it can be ignored for large-scale studies (but should be taken into account for coastal currents, in fronts, and in some channels and straits).

The formula is different when sea ice is present. In this case, it is not the air, but the sea ice that directly drags the water. The ice-water stress is described by

$$\tau_i = \rho_w C_{iw} |u_{iw}|(u_{iw}) \tag{1.4}$$

where ρ_w is the water density, C_{Di} is a drag coefficient (0.0055). The relative velocity in this case is between the ice and the surface water: $u_{iw} = u_{ice} - u_{water}$. Here u_{water} must not be ignored, as its characteristic values are comparable to those of u_{ice}.

In the Arctic Ocean, the water surface is often not fully ice-free or completely frozen over; sea ice concentration (α) can vary between 0 and 100%. Therefore, the total surface stress can be written as

$$\tau = \alpha \tau_i + (1 - \alpha)\tau_a \tag{1.5}$$

The effect of wind stress on the velocity in the Ekman layer, which is the upper water column where the effect of wind stress forcing is the most dominant, is calculated by the following equations:

$$-f v_{Ek} = \frac{\tau_x}{\rho D_E} \quad and \quad f u_{Ek} = \frac{\tau_y}{\rho D_E} \tag{1.6}$$

where f is the Coriolis parameter ($f = 2\Omega sin\varphi$, Ω is the rotation rate of the Earth, φ is the geographical latitude), about 1.45 x 10⁻⁴ s in the Arctic Ocean. The parameter D_E is the Ekman layer depth, typically around 20 meters in the Arctic Ocean (Hunkins, 1966). As the wind stress and the Ekman velocity are co-dependent, the equations (1.3), (1.4), and (1.6) are solved iteratively.

The wind-driven Ekman transport occurs at an angle to the wind forcing. In the Northern Hemisphere, the transport vector deviates about 45° to the right at the surface, and about 90° in the total vertical column of the Ekman layer. This means that the curl in the forcing wind field creates vertical motion. Negative wind stress curl in an anticyclone leads to convergent Ekman transport. Convergent water domes and is also pushed

downwards. This wind-driven vertical motion is called Ekman pumping. The opposite is called Ekman suction, when the divergent Ekman transport leads to upwelling in the upper water layers. The rate of this vertical motion (w_{Ek}) depends on the curl of the wind stress:

$$w_{Ek} = \frac{(\nabla \times \tau)}{\rho f} \tag{1.7}$$

where ρ is the density of the water and f is the Coriolis parameter.

Wind on a small scale is rather turbulent, but on a larger scale it follows the spatial trends of sea level pressure, driven by a geostrophic balance between the pressure gradient force and the Coriolis force. The large, basin-scale wind-driven structures in the ocean are driven by these geostrophic winds; therefore, for the investigation of wind-driven anomalies in the ocean, the understanding of the large-scale variability of atmospheric sea-level pressure is essential.

1.2.3.2. Large-scale Atmospheric Variability

Features of the large-scale atmospheric variability are presented through variations of sea-level pressure, due to its relevance for geostrophic winds that drive the basin-scale transport of upper layer waters in the ocean. Although variations of sea-level pressure show no particular periodicity, there are certain hemispheric patterns of its dominant modes. These often resemble teleconnections between different centers of action, and are described by oscillation indices. In the Northern Hemisphere, the most robust are the Arctic Oscillation (AO) and the North Atlantic Oscillation (NAO).

The AO is the main mode of variability in the Arctic troposphere that strongly affects Arctic circulation. In this study, the AO was calculated following the definition of Thompson and Wallace (1998): it was based on a principal component analysis or an Empirical Orthogonal Function analysis (EOF; see details in the Appendix) of the detrended November–April seasonal mean sea-level pressure anomaly field north of 20°N. Its pattern and time series are presented on Figure 1.6. The AO is characterized by a pattern of sea level pressure that has a center of action over the Arctic Ocean, and counterparts of opposite sign at lower latitudes in the Northern Pacific and Atlantic. This pattern can be interpreted as the surface signature of the variations in the polar vortex. Its strength is described by and index, whose time series show high correlations with hemispheric geopotential height and Eurasian surface air temperature anomalies on an interannual time scale (Thompson and Wallace, 1998).

During the negative phase of the AO, air pressure is high across the Arctic, which is associated with a strong Beaufort High, a prominent anticyclone over the Amerasian

Basin. This leads to the strengthening of the Beaufort Gyre that can store freshwater more efficiently due to enhanced Ekman transport from stronger anticyclonic winds inflating it. River runoff from Siberia is directly transported towards Fram Strait by a strong Transpolar Drift. During a positive phase of the AO, air pressure is lower in the Arctic. Siberian river runoff is brought towards the Amerasian Basin before leaving the continental shelf. At the same time, stored freshwater volume reduces in the Beaufort Sea, as the Beaufort Gyre is typically weaker (Mauritzen, 2012). As Haine et al. (2015) concludes, these processes suggest that the AO and the Beaufort High control the interannual variability of the freshwater system. The surface circulation redistributes freshwater by changing its pathways and residence times: the AO determines the freshwater source and delivery to the Amerasian Basin while the Beaufort High determines the freshwater storage of the Beaufort Gyre. This is consistent with the Arctic liquid freshwater content anomalies reported by Rabe et al. (2014), as their time series show a high correlation with the so-called Arctic Ocean Oscillation, a measure for the wind stress curl in the Arctic (Proshutinsky and Johnson, 1997). This suggests that the changes in Arctic liquid freshwater content are connected to regional changes in sea-level pressure fields rather than hemispheric-scale changes described by the AO.
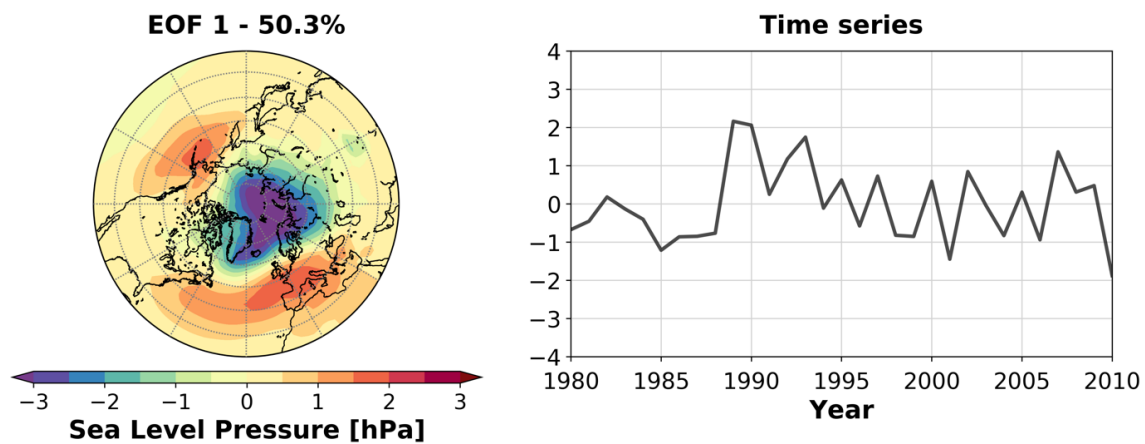

Figure 1.6: *Arctic Oscillation (AO) for winter (November–April) in NCEPcfsr reanalysis (Saha et al., 2010) as the (left) eigen vector and (right) principal component time series of the first empirical orthogonal function (EOF) of Northern Hemispheric sea-level pressure for the period 1980–2010.*

The Arctic Oscillation is closely related to the atmospheric pressure differences of the North Atlantic that also show a distinct pattern (Figure 1.7). This is called the North Atlantic Oscillation, a major source of low-frequency atmospheric variability in the North Atlantic that describes the co-variability of the strength of the Icelandic Low and the Azores High (Hurrell, 1995).

There are different methods to calculate an index that describes the North Atlantic Oscillation, but they are similar in that they derive the NAO index from normalised sea-level pressure time series of the North Atlantic sector (Greatbatch, 2000). Here it was

calculated following Hurrell et al. (2003) as the leading EOF mode of sea-level pressure variability in the region 20°N–70°N, 90°W–40°E (Figure 1.7). This method uses detrended sea-level pressure anomalies of the winter season (mean of December–February), as this teleconnection is present throughout the year, but its effects are most significant in winter (Barnston and Livezey, 1987).
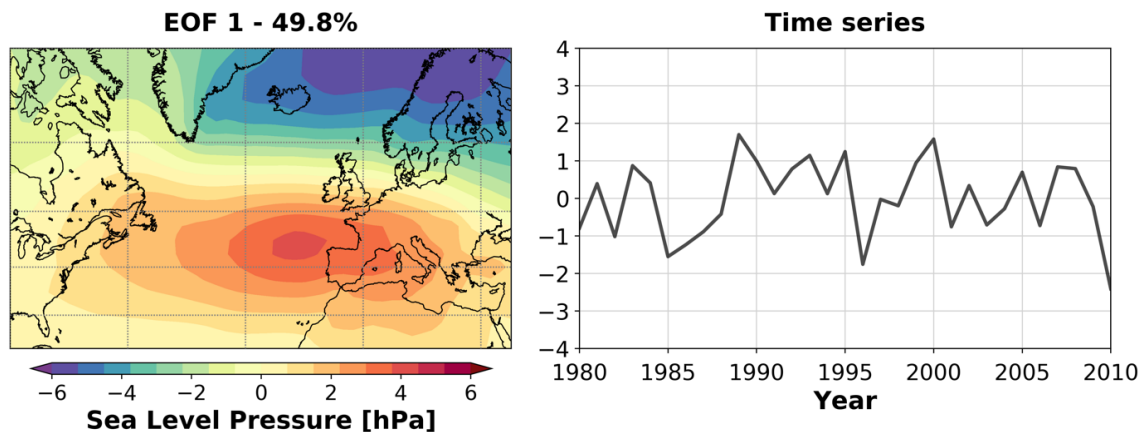

Figure 1.7: *North Atlantic Oscillation (NAO) for winter (December–February) in NCEPcfsr reanalysis (Saha et al., 2010) as the (left) eigen vector and (right) principal component time series of the first empirical orthogonal function (EOF) of Northern Hemispheric sea-level pressure for the period 1980–2010.*

The variability of the NAO influences the climate of the North Atlantic region, the underlying ocean, and the surrounding continents on interannual to decadal time scales (Marshall et al., 2001). The NAO can be interpreted as a measure of the strength of the westerly winds blowing across the North Atlantic Ocean. A high NAO situation means stronger than average westerly winds that especially in winter cause a negative temperature anomaly in the Canadian Arctic, and bring warmer than normal conditions over the Eurasian continent (Greatbatch, 2000). The NAO has a significant impact on oceanic processes as well. The long-term fluctuations of the sea surface temperature (SST) of the North Atlantic region correspond to atmospheric fields of sea-level pressure and surface winds (Kushnir, 1994). The NAO influences convection and deep water forming in the North Atlantic Ocean and the Nordic Seas (Dickson et al., 1996), as well as the North Atlantic gyre circulation (Curry and McCartney, 2001; Bersch et al., 2007). It also affects the transport of Atlantic Water into the Arctic, and affects temperature, salinity, sea ice cover, and thus freshwater in the Arctic Ocean (Dickson et al., 2000; Kwok, 2000).

The AO and the NAO have a high temporal correlation and are nearly indistinguishable (Deser, 2000). Considering their structure and applicability, the statistical arguments of Huth (2007) suggest that for interpreting the hemispheric circulation variability, the NAO should be preferred. Other studies also suggest that the AO is a rather statistical artifact, and the NAO is more physically consistent (Ambaum et

al., 2001), although the non-winter AO might be a true teleconnection separate from the NAO (Rogers and McHugh, 2002). Either AO or NAO, the large-scale wind variations are strongly associated with patterns of atmospheric sea-level pressure variability. The corresponding changes in oceanic circulation can among others impact salinity and sea ice, thus ultimately the freshwater content. The following chapter presents the state of the art of the research in the anomalies of Arctic and North Atlantic freshwater with a focus on their wind stress forcing associated with the above patterns of atmospheric variability.

1.2.3.3. Freshwater anomalies and the role of wind stress forcing

Observations from recent decades show significant anomalies in the freshwater content of the Arctic Ocean (Rabe et al., 2014) and also the Subarctic North Atlantic (Boyer et al., 2007). The anomalies in these two domains have a corresponding size and time scale. Moreover, the annual amount of freshwater communicated between their basins mostly through Fram Strait (Spreen et al., 2009; Rabe et al., 2013) and the Canadian Arctic Archipelago and Davis Strait (Curry et al., 2014) is also of similar order.

Synthetizing previous studies, (Aagaard and Carmack, 1989) created the first complete freshwater budget of the Arctic Ocean, and discussed its role in the regional and global circulation. The following advances in research were summarized by Serreze et al. (2006) combining terrestrial and oceanic observations, reanalysis data, and model results of Arctic freshwater, and by Dickson et al. (2007) reviewing the observations of its fluxes through the Arctic Ocean and subarctic seas. An overview of the growing attention to Arctic freshwater is presented by recent reviews focusing on its export to lower latitudes (Haine et al., 2015), on its role in the marine system (Carmack et al., 2016), and on modeling activities in its research (Lique et al., 2016).

Studies on the mechanisms controlling Arctic freshwater storage suggest the importance of wind stress forcing. Modeling the response of the Arctic Ocean to changes in atmospheric sea-level pressure, Proshutinsky and Johnson (1997) identified two wind-driven circulation regimes alternating with a period of 10-15 years. During an anticyclonic regime freshwater accumulates in the Beaufort Gyre, and it is released during a cyclonic regime (Proshutinsky et al., 2002). This is due to the varying strength of the Ekman pumping of freshwater, dependent on the wind field associated with the strength of the Beaufort High, a prominent anticyclone over the Amerasian Basin (Serreze and Barrett, 2011). The strength of the Beaufort High is also associated with the AO. In the Atlantic sector the AO is represented by the NAO, to which variations of Arctic freshwater have also been linked (Dickson et al., 2000). The effects of the AO and the NAO are rather similar since they are closely related (Deser, 2000). Overall, freshwater distribution in the Arctic Ocean is controlled by the combined effect of these features. The source of

freshwater and its pathways are determined by the AO, while the rate of its accumulation in the Beaufort Gyre depends on the strength of the Beaufort High (Mauritzen, 2012).

Proshutinsky et al. (2002) hypothesized a connection between Arctic freshwater content and export driven by atmospheric circulation regimes. It has been confirmed that the storage and export of both Arctic sea ice and liquid freshwater are linked and they are influenced by said regimes reminiscent of the AO (Zhang et al., 2003) and the NAO (Condron et al., 2009). Recent coupled model studies suggest their relationship and its link to atmospheric forcing. According to Lique et al. (2009) there is no significant correlation between liquid freshwater fluxes across the two pathways, although their volume transports are strongly anti-correlated. Jahn et al. (2010) showed that liquid freshwater export though the Canadian Arctic Archipelago and Fram Strait follow Arctic atmospheric circulation changes associated with the AO in 1 and 6 years, respectively, and discussed the major role that large-scale wind forcing plays by modifying sea surface height and freshwater content upstream in the Arctic. Wang et al. (2017) found this forcing to be associated with the fluxes being out of phase in the Canadian Arctic Archipelago and Fram Strait.

Changes in Arctic freshwater export can be connected to anomalies in lower latitudes. Variabilities in the Nordic Seas and the Subpolar North Atlantic Ocean are characterized by major freshening episodes in recent decades (Curry and Mauritzen, 2005), the first of which happened in the 1970s and was named the Great Salinity Anomaly (GSA) by Dickson et al. (1988). Aagaard and Carmack (1989) reported that the origin of this event must have been an anomalously large Arctic freshwater (both sea ice and liquid) discharge through Fram Strait. This was confirmed by Häkkinen (1993) using a coupled ocean-sea ice model, who also identified high latitude wind field changes as a source of this discharge anomaly. The 1970s GSA was followed by similar events in the 1980s (Belkin et al., 1998) and the 1990s (Belkin, 2004). According to Haak et al. (2003), these anomalies were also a result of an excess of Arctic freshwater export mainly through Fram Strait due to wind forcing. Karcher et al. (2005) also linked the 1990s GSA to an increased freshwater export through Fram Strait, and showed that it was a response to the prolonged high NAO state of the early 1990s.

But even if the link between the Arctic and the Subarctic North Atlantic freshwater contents is accepted, it is still not clear what drives the redistribution within their joint system, as its response to atmospheric forcing on a longer time scale is still not fully understood. The freshwater content of the Beaufort Gyre seems to have stabilized at a high level in recent years (Zhang et al., 2016), concurrent with an unusually long anticyclonic circulation pattern in the Arctic (Proshutinsky et al., 2015). Some studies found that an eventual switch to a cyclonic regime could result in its release, possibly causing another GSA (Giles et al., 2012; Stewart and Haine, 2013). Past GSAs have mostly been associated with changes in large-scale Arctic circulation, especially in the wind field over the Beaufort

Gyre, but this link is still not clearly understood. For example, the 1970s event occurred during an anticyclonic regime, and as Dickson et al. (2000) concludes, an anomalous freshwater export from the Arctic can occur during both extrema of the NAO.

Nevertheless, the size and timing of observed freshwater anomalies in the Arctic Ocean and in the Subarctic North Atlantic during the last 20 years might suggest a multi-decadal oscillation between their basins (Horn, 2018), although it is difficult to assess due to the still too short history and the uncertainty of observations. The fluxes between their basins are also particularly difficult to measure. To overcome these limitations there have been successful attempts at simulating their freshwater content with forced ice-ocean models (e.g. Häkkinen, 1993; Gerdes and Koberle, 1999; Haak et al., 2003; Karcher et al., 2005; Gerdes et al., 2008; Stewart and Haine, 2013), but still not sufficient research has been done considering them together as a joint system using fully coupled models with a dynamic atmospheric component.

2. Objectives and Methods

This chapter briefly summarizes the knowledge gaps in Arctic and Subarctic North Atlantic freshwater covariability and its atmospheric drivers. This is followed by stating the center hypothesis and the main objectives of this study. Then an introduction of the applied model is provided, including a detailed description of its partially coupled configuration, followed by the presentation of the experiment design.

2.1. Objectives

The previous chapter presented the general knowledge regarding freshwater content and fluxes in and between the Arctic Ocean and the Subarctic North Atlantic, including its variability and its possible drivers. It is well established that the Arctic Ocean is an important freshwater reservoir that is connected to the North Atlantic Ocean, and exchanges a large volume of water with it. Variations in the inflow of warm and saline Atlantic Water into the Arctic, and in the outflow of cold and fresh Arctic Water into the Subarctic North Atlantic can potentially cause large anomalies in the freshwater content of both domains. But the frequency and the amplitude of these variations are not clear due to insufficient length and uncertainties of observations. The contribution of the changes in different fluxes to anomalies of the total freshwater content of both basins is also not fully understood. The observations suggest a link between the Arctic and the Subarctic North Atlantic freshwater contents, but some of the large anomalies in the North Atlantic are attributed to other sources than an anomalous flush of freshwater from the Arctic.

Moreover, the drivers of these variations are also debated. One theory is that they are primarily driven by wind stress forcing. Variations of the wind in the Arctic, associated with alternating cyclonic or anticyclonic regimes, cause periodic accumulation and release of freshwater. During times of Arctic accumulation, salinity rises in the North Atlantic, and then drops when freshwater is released from the Arctic. The regimes and the freshwater anomalies are likely connected to variations in the large-scale atmospheric circulation, represented by oscillation indices, but it is not clear how. Observations show large anomalies in the freshwater fluxes during both extrema of the indices, and some of the variations in the North Atlantic content are possibly connected to local atmospheric forcing in the Labrador Sea, and thus do not originate in the Arctic.

Based on the current state of the art in research, the hypothesis of this study is that the freshwater contents of the Arctic Ocean and the Subarctic North Atlantic are connected, and form a joint system that has a potential for an oscillating covariability. The hypothesis also includes that this seesaw between the two basins is governed by wind stress forcing associated with large-scale patterns of atmospheric variability. Surface winds associated with these patterns (most likely the NAO or the AO) are the driving forces behind periods of freshwater accumulation in the Arctic, and periods of its release to the Subarctic North Atlantic, either in a form of an anomalous liquid freshwater flush, or sea ice export.

In order to test these hypotheses, the following objectives were set:

1. Simulate the oceanic circulation of the Arctic and Subarctic North Atlantic system with the fully coupled global Max Planck Institute Earth System Model (MPI-ESM), and analyse the freshwater budgets of their basins.

The MPI-ESM was selected because 1) other studies had already successfully used it to investigate freshwater content and sea ice in the Arctic Ocean and in the North Atlantic Ocean; 2) its model grid construction enables relatively high resolution simulations in these two domains and in particular in the key regions at their boundary; 3) a modified coupling configuration allows targeted experiments with prescribed wind forcing scenarios (see details in Chapter 2.2—Model Description). The goal was to evaluate whether a link between the Arctic and Subarctic North Atlantic freshwater contents is physically possible, and if yes, then how persistent it is in time. For this, the simulation period had to be significantly longer than that of the available observations. The contribution of liquid and solid freshwater content and their fluxes to the variability of the total content was also to be investigated.

2. Identify key patterns of atmospheric variability that govern the changes in Arctic and Subarctic North Atlantic freshwater content through wind forcing.

The aim was to derive the NAO and AO patterns from the fully coupled MPI-ESM results, and analyze the covariability of their time series with time series of the freshwater contents and fluxes by statistical methods. As the NAO and AO are derived from atmospheric sea-level pressure, possibly identified connections do not confirm the role of wind stress forcing. Therefore, the objective was also to rerun the model simulations with prescribed wind forcing based on observations, utilizing the partially coupled configuration of the model, and then compare the partially coupled results with the observed time series of freshwater content and fluxes.

3. Perform model experiments by perturbing the wind forcing associated
    with the identified key patterns of atmospheric variability.

The results of the previous objective are built on a statistical analysis of freshwater and sea-level pressure. In order to confirm the physical feasibility of the findings, in particular, the role of wind forcing, further model experiments were necessary. The aim of these experiments was to describe the mechanisms governing the freshwater variability by perturbing the wind field associated with the key large-scale patterns of atmospheric variability identified before. As the partially coupled configuration allowed the prescription of wind forcing while maintaining consistency of heat and energy exchanges between the atmosphere and the ocean, these experiments enabled the isolation of the wind forcing effect on freshwater variability.

The results section is separated into three main chapters corresponding to the three objectives outlined above.

2.2.   Model Description

The numerical experiments in this study were performed with the Max Planck Institute Earth System Model (MPI-ESM). The MPI-ESM covers the entire globe, and consists of model components simulating physical and biogeochemical processes of the atmosphere and the ocean. The model has been used in many studies of freshwater content and fluxes. For example of Arctic sea ice variability (Koenigk et al., 2009; Notz et al., 2013) and predictability (Tietsche et al., 2013), and seasonal heat and freshwater cycles (Ding et al., 2016). In the North Atlantic Ocean it has also been used to simulate the freshwater budget and circulation (Deshayes et al., 2014), and deep water formation and its role in the overturning circulation variability (Lohmann et al., 2014). There are examples of paleoclimatic studies using MPI-ESM to investigate water and heat transport through Fram Strait (Jungclaus et al., 2014) and the consequences of Arctic freshwater export to the North Atlantic (Moreno-Chamarro et al., 2017). Other studies focusing on the formation and propagation of GSAs (Haak et al., 2003) and North Atlantic climate variability including freshwater content and fluxes (Müller et al., 2014) have used its ocean component MPIOM.

In this study the MPI-ESM model version 1.2.00p4 was used in low resolution (LR). Despite its coarser horizontal grid in comparison with the mixed resolution (MR) version, it produces very similar atmospheric mean state and variability as the MR version. At the same time, it simulates oceanic processes in the North Atlantic and in the Nordic Seas even better, due to the horizontal grid design of the ocean component that allows for a better

representation of these regions that are in the focus of this work (Jungclaus et al., 2013). This study is built on model simulations with two different configurations of the MPI-ESM: its original fully coupled configuration, and a partially coupled configuration with prescribed wind forcing.

2.2.1. Model Components

The ocean component is the MPIOM, a free-surface model that solves the primitive equations for the ocean considering it a hydrostatic Boussinesq fluid (Marsland et al., 2003). It includes a dynamic thermodynamic sea ice model based on the viscous-plastic rheology of Hibler (1979). MPIOM has 40 unevenly spaced vertical levels and uses a curvilinear orthogonal grid in its LR version. This horizontal grid has a nominal resolution of 1.5° which means 15 km near the model poles and up to 185 km elsewhere. The two model grid poles are over land in Antarctica and Greenland, to avoid the short time steps otherwise required by small grid distances near the geographic poles. Although the model is not eddy-permitting in this resolution, it still allows proper representation of oceanic processes especially in the polar regions of the Earth and in key deep water formation regions in the Southern Ocean and in the North Atlantic (Jungclaus et al., 2013).

The atmospheric component ECHAM6 has a horizontal resolution of approximately 200 km, and 47 vertical levels resolving the atmosphere from the surface up to 0.01 hPa (Stevens et al., 2013). In the original fully coupled configuration, the wind field used to calculate the surface stress is that calculated by ECHAM6; however, in addition to this, this study used an alternative configuration as well with prescribed wind forcing of ocean and sea ice. This has been introduced by Thoma et al. (2015) as the Modini method, in which the model components are partially coupled.

2.2.2. Coupling

The model components of MPI-ESM are coupled, which means that there is an exchange of fluxes and state variables between them at given intervals. The coupling structure of the main physical components is shown on Figure 2.1. Time stepping occurs independently in ECHAM6 and MPIOM according to a parameter set in the namelist of the model components. This study used 45-minute intervals for the integration of the ocean component, and 7.5-minute intervals for the atmosphere.
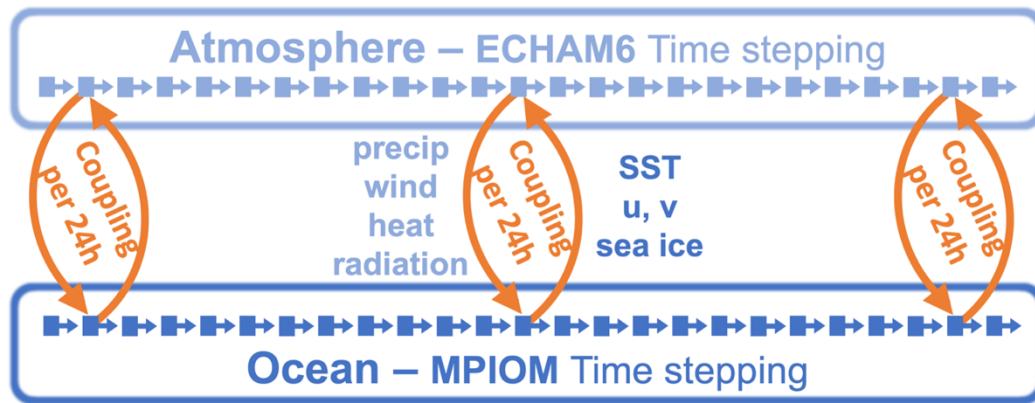
Figure 2.1. *Coupling of the main physical atmospheric and oceanic model components in the original fully coupled configuration of MPI-ESM. Time stepping of the atmosphere and the ocean is done independently between the coupling periods every 24 hours of model time.*

In MPI-ESM, coupling takes place every 24 hours of model time using the Ocean Atmosphere Sea Ice Soil (OASIS3) coupler (Valcke et al., 2003). During coupling, the following physical parameters are passed from the atmosphere to the ocean: precipitation (snow on ice surface separately), wind speed at 10 meters, wind stress (for sea ice and for open water surface respectively), heat fluxes, and surface net downward radiation flux. From the ocean the values of SST, ocean surface velocity, sea ice thickness and area fraction, and snow thickness on sea ice are passed to the atmosphere.

The momentum flux between ocean and atmosphere (i.e. the wind stress) is calculated based on the velocity difference between the wind and ocean surface velocity and ice speed, respectively. This provides a better simulation of ocean surface conditions in many regions compared to an only wind-dependent parametrization (Jungclaus et al., 2006).

River runoff is simulated in the land hydrology module of ECHAM6 that contains a river routing scheme. Freshwater flux from river discharge into the ocean is not coupled separately, but is added to the precipitation field, meaning that its full amount is inserted only over the top cell of the ocean grid. The residual of precipitation minus evaporation over ice sheets and glaciers is converted immediately into surface runoff (Jungclaus et al., 2013).

2.2.3. Modini Method

In addition to model runs with its original fully coupled configuration, this study also performed experiments with prescribed wind stress forcing. The tool for this was the Modini method, a partially coupling technique introduced to the MPI-ESM by Thoma et al. (2015a). This approach enables the ocean component MPIOM to be driven by wind stress estimated from an external source while maintaining consistency of heat and energy exchanges between the atmosphere and the ocean. It means that even though MPIOM uses

another source, the atmospheric component ECHAM6 still computes its own wind field according to the fully coupled dynamics. Moreover, the atmosphere can also respond to the external forcing in a self-consistent way by receiving exchanged parameters from MPIOM, since the rest of the coupling remains the same as in the original configuration (Figure 2.2)

Using reanalysis wind fields as external source, Thoma et al. (2015a) demonstrated the improved skill of Modini-MPI-ESM in simulating the observed timing of events associated with the internal variability of the climate, including a better representation of the observed NAO, Arctic sea ice, and the Atlantic Meridional Overturning Circulation in comparison with the fully coupled MPI-ESM. The hindcasts with MPI-ESM of Thoma et al. (2015b) after an initialization with the Modini approach also show considerable skill.
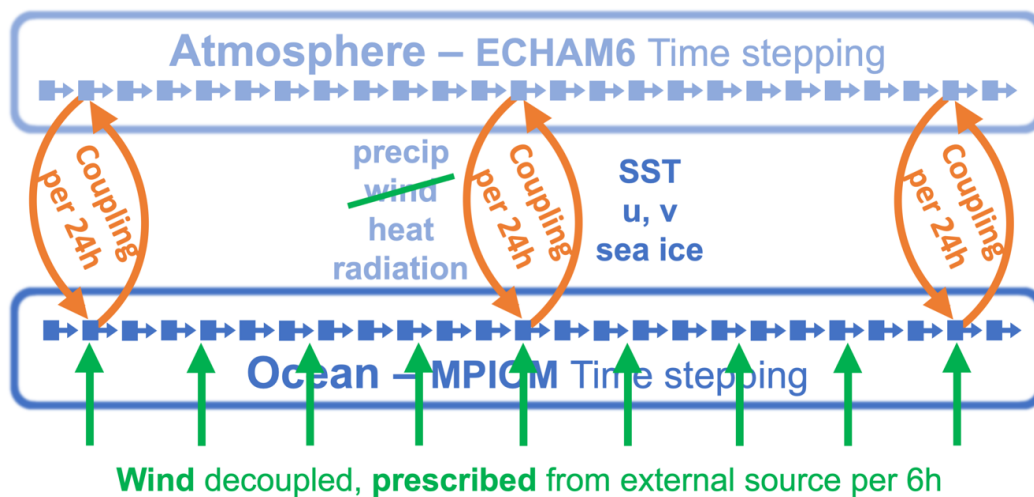
Figure 2.2. The partial coupling of the main physical atmospheric and oceanic components of Modini-MPI-ESM. The atmosphere-to-ocean momentum forcing is decoupled, and the ocean component receives wind stress data every 6 hours from a prescribed external source.

The flexibility of the Modini assimilation procedure enables the design of various experiments, as it allows the wind coupling to be switched on or off at any time. If the partial coupling is active, the wind stress is derived from the relative difference between the ocean surface (and sea ice) and the prescribed external wind speed. Switching the Modini-mode off, the model returns to the original fully coupled dynamics, and calculates the surface stress from the relative difference between the ocean surface (and sea ice) and the wind calculated by ECHAM6.

This flexibility regarding the constrain of momentum forcing allows the design of various types of experiments. A partially coupled spin-up of the model which is then run unconstrained improves the model performance (Thoma et al., 2015a) and has a promising forecast potential (Thoma et al., 2015b). Constraining the model with observed wind data can provide decadal hindcasts (Thoma et al., 2015b). The comparison of otherwise identical fully and partially coupled model runs allow the estimation of the role of wind

forcing in driving oceanic processes, and the perturbation of the prescribed wind data enables targeted studies of certain effects of wind forcing.

This study used the Modini method for the latter two purposes: for the estimation of the impact of atmospheric momentum forcing on Arctic and Subarctic North Atlantic freshwater variability in general, and for the study of the effect of specific modes of wind forcing variability by locally perturbing the prescribed wind forcing.

2.2.3.1. Forcing Data

The source of external wind data in this study was the NCEPcfsr (the National Centers for Environmental Prediction's Climate Forecast System Reanalysis (Saha et al., 2010)) dataset because it provided the best results for Modini-MPI-ESM compared to alternative sources in the analysis of Thoma et al. (2015a). Following their approach, the NCEPcfsr wind data was applied here as an anomaly forcing; the temporal variability of the 6 hourly NCEPcfsr wind field was extracted and applied as anomalies to the climatology of the fully coupled control runs to reduce shocks and drifts after switching on the Modini forcing.

2.3.   Experiment Design

This study used the MPI-ESM model version 1.2.00p4 in its low resolution. The experiment design for the first two objectives (for the simulation and analysis of the Arctic and Subarctic North Atlantic freshwater system, and for the identification of key patterns of atmospheric variability that drive their changes) is shown on Figure 2.3. As its construction was based on the results the second objective, the experiment design for the third objective (targeted model experiments with perturbed wind forcing) is presented at the beginning of the corresponding chapter (Chapter 5.1—Idealized Wind Forcing Scenarios, Experiment Design).

The basis of all model runs presented here was a 1000-year spin-up simulation performed at the Max Planck Institute with pre-industrial boundary conditions. In order to provide restart conditions for coupled simulations with as little model drift as possible, Jungclaus et al. (2013) started the spin-up simulation from temperature and salinity fields of previous CMIP3 preindustrial experiments, and integrated the model for 1900 years.

The fully coupled control simulations of this study were based on this long spin-up and used the same setup and atmospheric forcing as the historical-CMIP5 scenarios from 1850 to 2005, and an atmospheric forcing according to the RCP4.5 emission scenario until 2016. The total simulated period was thus 167 years for 1850–2016 (Figure 2.3). In order to assess the internal variability of the model system, an ensemble of 10 control members was created. These members were completely identical except for the perturbation of their

initial conditions. This was achieved by a lagged initialization: all members began in 1850, but the first member (CTRL_00) was restarted from the spin-up simulation, and the restart data of every subsequent member (CTRL_0x) was the result of the first member after x days. For example, the restart fields of CTRL_04 (started in 1850-01-01) were the results of CTRL_00 for 1850-01-04, redated to 1849-12-31. The 10 members represent a total of 1670 years of model simulation.

In addition to the fully coupled control runs, the model was also used in its partially coupled configuration. These partially coupled runs were also created as an ensemble, and all 10 members were restarted in 1979 based on their corresponding fully coupled control runs, and were identical to those except for the wind forcing. The run Modini_0x was therefore essentially a repeated CTRL_0x run for 1979–2016 with wind forcing based on the NCEPcfsr data base (Figure 2.3). The NCEPcfsr wind data ($\bar{v}_{NCEP} + v'_{NCEP}(t)$, mean for 1979-2016 plus temporal variability) was applied as an anomaly forcing ($v_{Modini\_0x}(t)$) derived for each Modini member, retaining the 1979–2016 wind climatology ($\bar{v}_{CTRL\_0x}$) of the corresponding control member: $v_{Modini\_0x}(t) = \bar{v}_{CTRL\_0x} + v'_{NCEP}(t)$ for each $x = 0..9$.
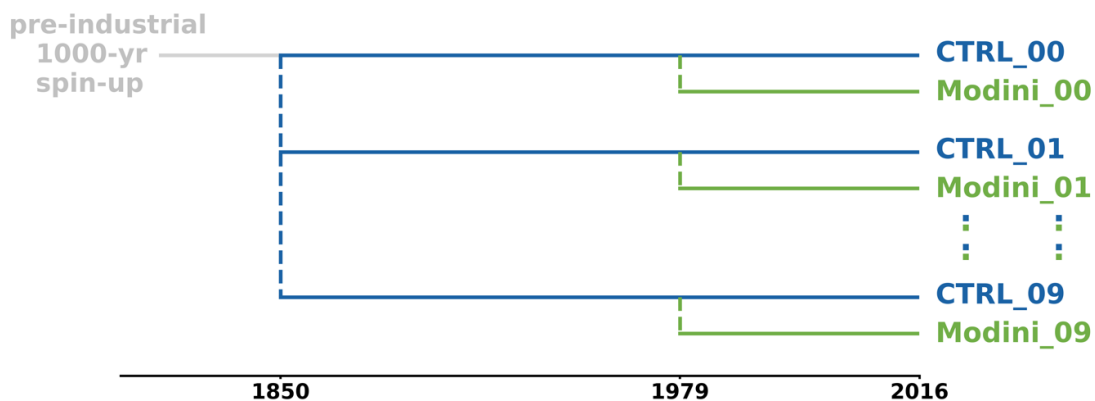

Figure 2.3. *Experiment design. CTRL_00–09 denotes the 10 members of the fully coupled control experiments for the period 1850–2016. The Modini_00–09 runs are corresponding reruns for the period 1979–2016 with prescribed wind forcing based on NCEPcfsr data.*

Key diagnostics in this study were the freshwater content and transport considering both its liquid and solid state. The domains used here for the Arctic Ocean and for the Subarctic North Atlantic are shown in blue and red on Figure 2.4, where the location of the oceanic sections bordering them are indicated as green lines. These were set as follows: the Bering Strait at 65.4°N between Siberia and Alaska; the Canadian Arctic Archipelago from 71.5°N to 78°N in northern Baffin Bay around 72-74°W; Fram Strait at 79°N between Greenland and Svalbard; the Barents Sea Opening from 70.0°N, 18.9°E to 76.6°N, 16.6°N between Svalbard and Norway; and the Atlantic 50°N section at 50°N between North America and Europe.
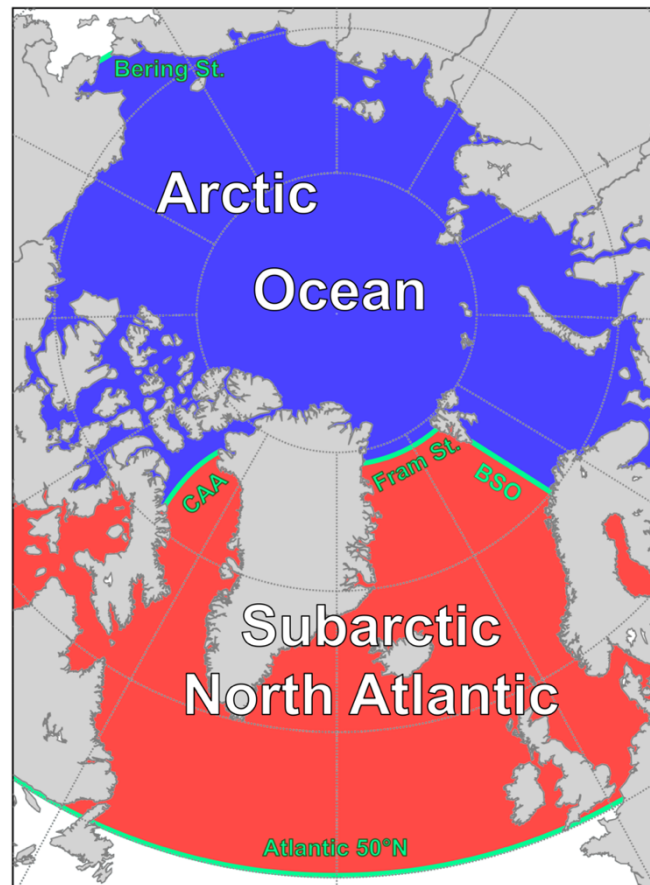
Figure 2.4. *The domains and sections used in this study. The blue area is the Arctic Ocean, the red is the Subarctic North Atlantic (comprising the Nordic Seas and the Subpolar North Atlantic Ocean north of 50°N). The green lines show the oceanic sections bordering their domains: Bering Strait, the Canadian Arctic Archipelago (CAA), Fram Strait, the Barents Sea Opening (BSO), and the Atlantic 50°N line.*

Unless otherwise stated, the reference salinity for this study was set as 34.8, and the liquid freshwater content was integrated in the total vertical column. The values of liquid freshwater content and fluxes were calculated according to equations (1.1) and (1.2) in Chapter 1.2.1—Freshwater Content and Fluxes, Concept. The solid freshwater content was calculated from simulated sea ice (with a constant salinity of 5 in MPI-ESM), including the amount of freshwater stored in snow on sea ice as well.

To analyze the large-scale variations in freshwater, this study focused on its annual means, as at high latitudes its intra-annual variability is dominated by the redistribution between its liquid and solid phases due to freezing and melting.

3. Arctic and North Atlantic Freshwater Covariability

The first objective of this work was to simulate the freshwater system of the Arctic and the Subpolar North Atlantic Oceans in the fully coupled MPI-ESM and to analyse their covariability.

In this section, model results of main oceanic parameters are presented with a focus on freshwater. Means and time series based on model results from a 10-member ensemble of more than 150-year long simulations are analysed in order to assess the spatial and temporal variability of both liquid and solid freshwater content and fluxes. Finally, the possible link suggested by observations from recent decades between the total freshwater content of the domains of the Arctic Ocean, and Subarctic North Atlantic (the Subpolar North Atlantic Ocean and the Nordic Seas) is evaluated to see whether the link can be simulated with the model and if so, then how robust it is over a longer time scale.

3.1. Simulated Oceanic Variability in MPI-ESM

The model simulates the main features of oceanic circulation in the Arctic Ocean and in the Subarctic North Atlantic relatively well. The large scale horizontal circulation in the ocean is illustrated by the vertically integrated barotropic streamfunction. This diagnostic visualizes simulated features of the mean circulation such as wind-driven gyres and boundary currents. In MPIOM, it is diagnosed from the vertically integrated horizontal flow. Figure 3.1 shows the ensemble mean of the mean barotropic streamfunction for the period 1980–2010 from the fully coupled control runs. On the plot negative values denote cyclonic circulation, and positive values represent anticyclonic circulation. The Arctic Basin is dominated by the clockwise circulation of the Beaufort Gyre, reaching a strength of 5 Sv. Towards the Eurasian Basin, the direction of the mean flow is from the Siberian shelf seas towards Greenland and Fram Strait, corresponding to the Transpolar Drift. About half of the Eurasian Basin is characterised by negative values denoting counter-clockwise cyclonic flow, indicating the pathway of Atlantic Water circulation. Lower latitude sub-Arctic waters have stronger cyclonic circulation. This is clearly visible in the Nordic Seas, and especially in the North Atlantic Ocean, where values reaching -28 Sv

mark the position of the Subpolar Gyre. The northernmost part of a Pacific Subpolar Gyre is visible south of the Bering Sea, too.
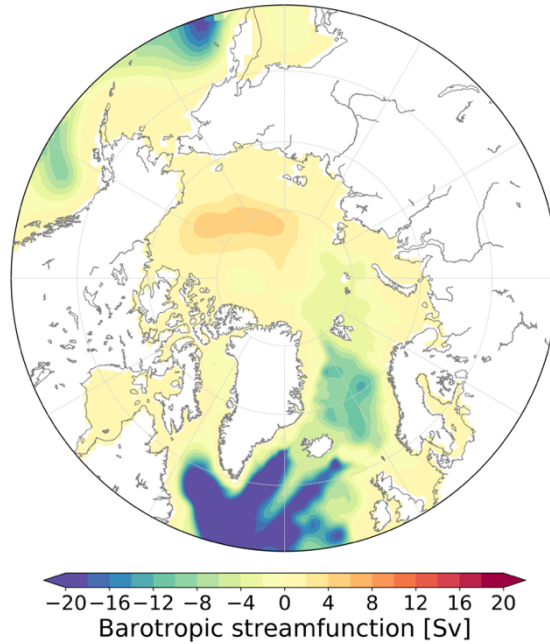

Figure 3.1. Mean barotropic streamfunction for the period 1980–2010. Ensemble mean of 10 fully coupled control runs. Negative values denote cyclonic circulation; positive values denote anticyclonic circulation.

For the analysis of the link between the Arctic Ocean and the Subarctic North Atlantic, the proper representation of water exchange between their basins is particularly important. The total net transports of water across sections bordering their domains is shown in Table 2 along with estimated values based on observations.

Section	Simulated net water transport [Sv]	Observed values
Bering Strait	0.68 ± 0.02	1.0 ± 0.05 (Woodgate, 2018)
Canadian Archipelago	-1.15 ± 0.08	-1.4 ± 0.2 [a]
Davis Strait	-1.16 ± 0.08	-2.3 ± 0.7 (B Curry et al., 2011)
Fram Strait	-3.22 ± 0.14	-1.75 ± 5.0 (Fieg et al., 2010)
Barents Sea Opening	3.54 ± 0.13	2.0 (Smedsrud et al., 2010)

Table 2. Characteristics of simulated oceanic flow across different sections for the period 1980–2010. Ensemble mean and standard deviation of 10 fully coupled control runs. The observed values are references closest to the 1980–2010 period. Negative values indicate southward transport.
[a] Approximated from the Nares Strait flux, -0.85 ± 0.1 (Münchow, 2015) and the Lancaster Sound flux, -0.53 ± 0.1 (Peterson et al., 2012).

According to Table 2, the simulated transports are close to observed values. The Bering Strait inflow and the Davis Strait outflow is weaker than observed, but they are both within the range of simulations with other models used for Arctic studies (Aksenov

et al., 2016). MPI-ESM overestimates the southward transport component in Fram Strait, although it is within the range of observational uncertainties. The simulated inflow of Atlantic Water into the Arctic through the Barents Sea Opening is also larger than observed, but it is also within the range of other model simulations (Muilwijk et al., 2019).

Sea surface temperature plays a significant role in the variability of atmosphere-ocean fluxes, therefore it is a very important parameter in coupled model simulations. A mean climatology for simulated sea surface temperature compared to the PHC3.0 climatology of Steele et al. (2001) is shown on Figure 3.2. The ensemble mean for the period 1980–2010 is at the freezing point of sea water in almost the entire Arctic Ocean, as well as in the sea ice covered Baffin Bay and along the eastern coastline of Greenland, similar to observations. There is a strong gradient indicating the inflow of relatively warm Atlantic Water in the Barents Sea where sea surface temperature rises up to 7°C and also in the Nordic Seas up to 10°C. Values in these regions are several degrees higher than observed. The Subpolar North Atlantic Ocean is characterised by an east-west gradient: the Labrador current has a surface temperature of below 3°C, and the Labrador Sea is around 7°C. There is a gradual increase eastward up to 13°C in the eastern basin close to Ireland similar to observations, although a warm bias is present in the northernmost parts of the North Atlantic (close to Greenland and Iceland). Further south in the western basin there is a cold bias in the model simulations.
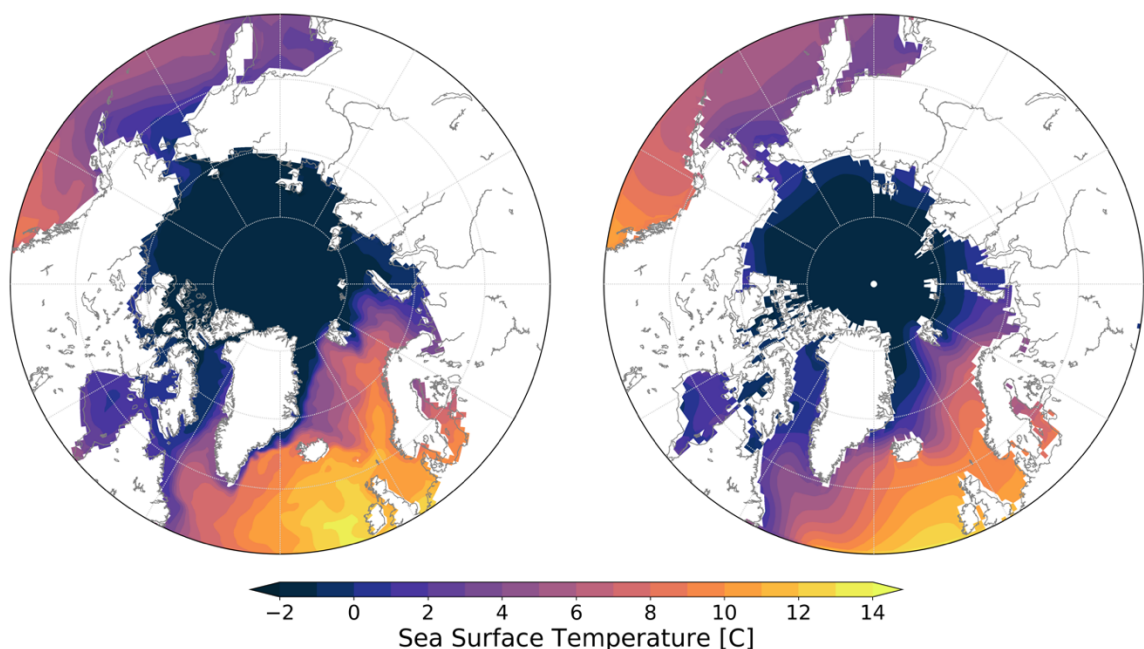

Figure 3.2. *Mean sea surface temperature. From (left) MPI-ESM simulations as ensemble mean of 10 fully coupled control runs for the period 1980–2010 and from (right) PHC3.0 climatology (Steele et al., 2001).*

The mean sea surface salinity from the model and from observations is presented on Figure 3.3. The ensemble mean of the model for 1980–2010 shows values of 30–32 in the

Arctic Ocean, and below 28 and down to 14 near river mouths in some shelf seas. The surface is somewhat saltier in the Amerasian Basin, and much fresher in the Siberian shelf seas and along the Canadian coast than observations. Surface salinity in the Arctic Ocean is highest in the Eurasian Basin where values reach up to 33.5, but most of the Eurasian Arctic has a fresh bias. The simulated values around the Canadian Arctic Archipelago are around 28–32. These are lower than observations, indicating a fresh bias, extending further south into the Baffin Bay. In the Subpolar North Atlantic, the model calculates surface salinity around 34.5 in most of the western basin, and above 35 and up to 35.5 in the eastern basin. These values north of 50°N are generally close to observations, with a slight salty bias in the Labrador Sea, and fresher waters along southern edge of the domain at 50°N. In the Nordic Seas the pathway of Atlantic Water is clearly seen in the higher values above 35, as well as in the saline extension into the Barents Sea. These are rather similar to observations. At the same time, the simulated values for the fresher waters of the East Greenland Current are up to 1.5 higher than observed.
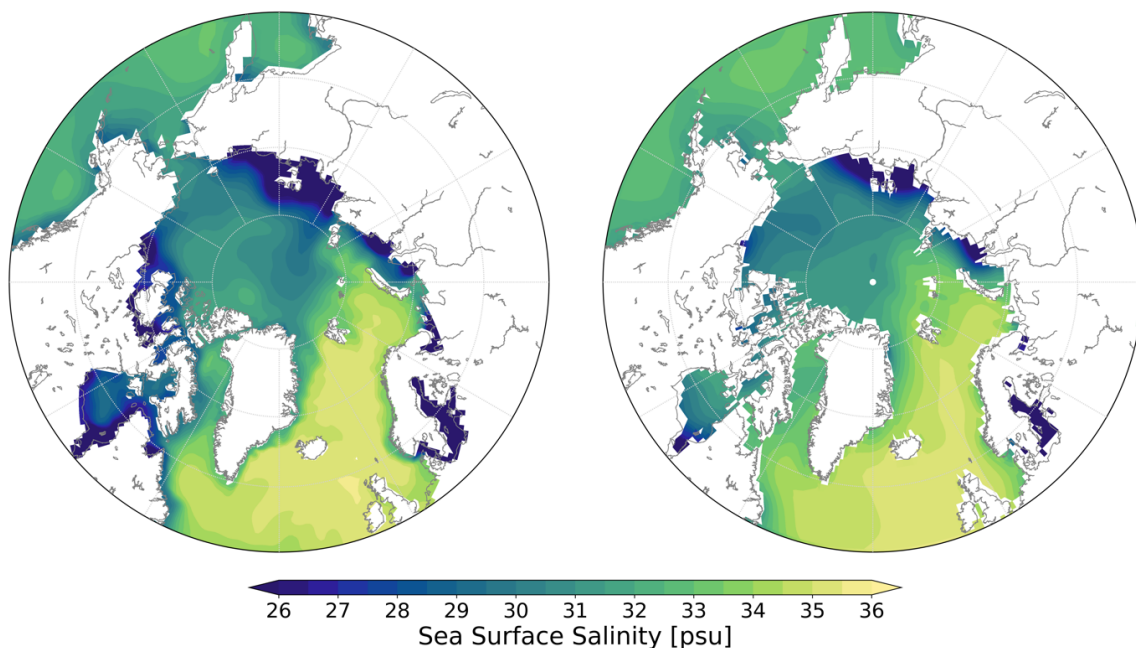

Figure 3.3. Mean sea surface salinity. From (left) MPI-ESM simulations as ensemble mean of 10 fully coupled control runs for the period 1980–2010 and from (right) PHC3.0 climatology (Steele et al., 2001).

The simulated vertical structure of salinity is illustrated by the depth of the 34.8 isohaline on Figure 3.4. This plot shows the depth of the 34.8 salinity level where it exists; where the entire column is more saline, values show 0 meters; where the entire column is fresher, values show the total depth of the water column. According to Figure 3.4, in most of the deep Arctic basin MPI-ESM calculates salinities lower than 34.8 in the upper several hundred meters. The simulated depth of the 34.8 isohaline reaches 700 meters in the Canada and Makarov Basins. This is about 300 meters deeper than in the PHC3.0

climatology, indicating a fresh bias, although it should be noted that the Arctic Ocean Atlas (Environmental Working Group (EWG) 1997, 1998), which is the source of most of the Arctic salinity data in the PHC3.0 hydrography, is based on observations mostly from the 1970s and the 1980s, and therefore does not include the significant freshening observed in the Arctic starting from the early 1990s (Rabe et al., 2014). The model simulations have a fresh bias in the Eurasian Basin too, especially in its eastern part, where the simulated 34.8 salinity level is more than 300 meters deeper than observed. Values in the shelf seas mostly agree well with observations, because there the entire water column is fresher than 34.8. Another notable difference in the Arctic is the Barents Sea where the 34.8 isohaline is much shallower in the model than observed, except for its southern part close to land. Near the shores the model simulations have a fresh bias elsewhere too, for example along the Norwegian coast, and along the East Greenland Current and the Labrador Current. But in most open seas outside the Arctic the simulated level of the 34.8 isohaline is higher than observed, for example in the Greenland Sea or in the Labrador Sea, indicating a saline bias not only on the surface, but in deeper layers too.
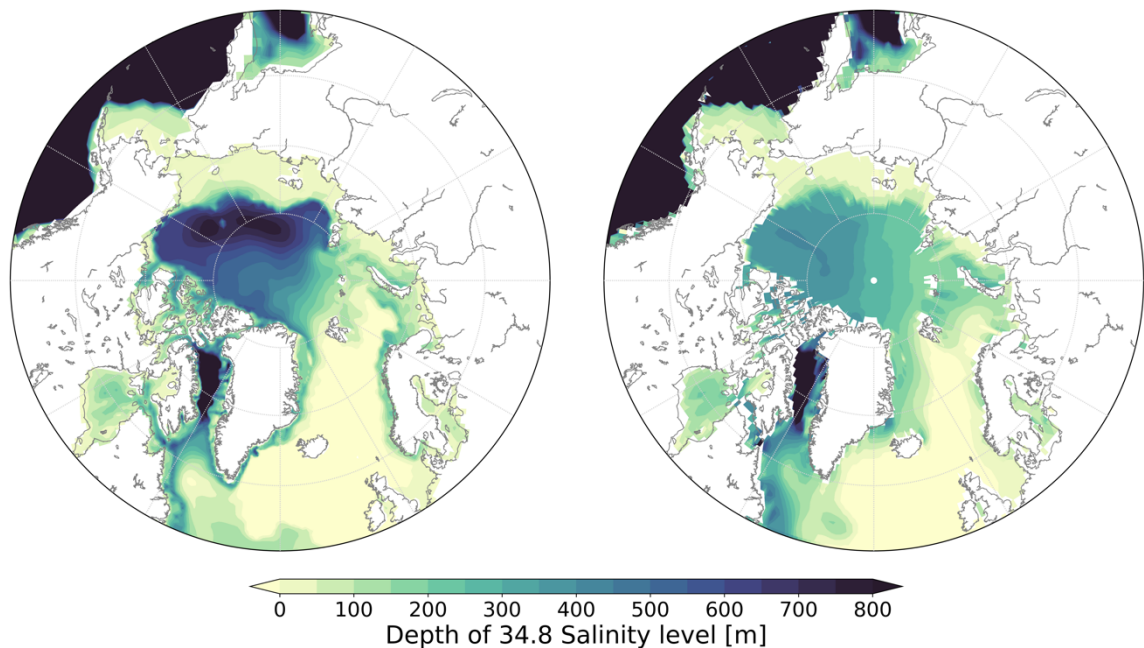

Figure 3.4. Mean depth of the 34.8 salinity level. From (left) MPI-ESM simulations as ensemble mean of 10 fully coupled control runs for the period 1980–2010 and from (right) PHC3.0 climatology (Steele et al., 2001). Where salinity is higher than 34.8 in the entire water column, values show 0. Where salinity is lower than 34.8 in the entire water column, values show the total depth.

Figure 3.5 shows the mixed layer depth according to model diagnostics. It is defined as the depth where the density is at least 0.125 kg/m³ higher than the surface value. The largest values in the MPI-ESM simulations are in the Labrador Sea and in the Nordic Seas. In the Labrador Sea, the mixed layer depth typically reaches 3000 meters. In other parts of the Subpolar North Atlantic, the average maximum is between 200 and 1000 meters.

Values exceed 1000 meters in a large part of the Nordic Seas, reaching 2000 meters in the Greenland Sea. The model calculates considerable mixing in the Barents Sea, where the average values reach 300 meters. The highest monthly mean values across the ensemble during the period of 1980–2010 can reach 3000 meters in the Norwegian Sea, 2000 meters in the northern Baffin Bay, and 1000 meters within the Arctic Ocean, in the Nansen Basin north of Svalbard (not shown).
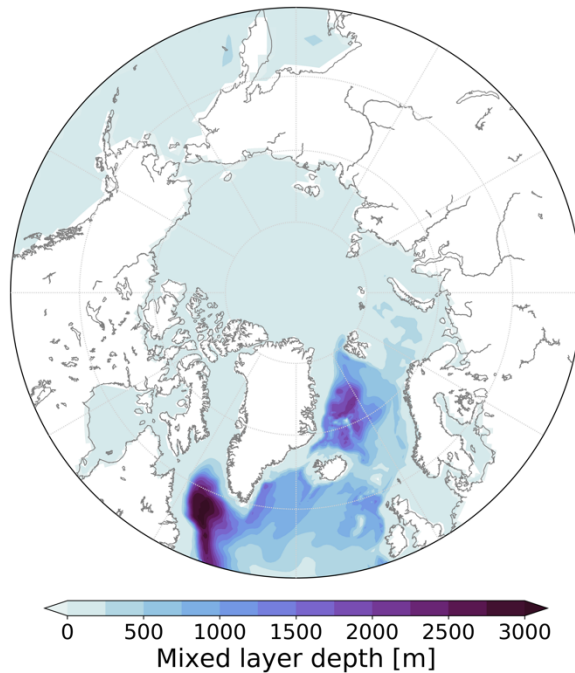

Figure 3.5. *Average maximum mixed layer depth from MPI-ESM simulations as ensemble mean of 10 fully coupled control runs for the period 1980–2010. Values have been calculated as the annual maximum of monthly mean mixed layer depth for each year, and then averaged over 30 years for the period 1980–2010.*

Finally, simulations of sea ice are presented on Figure 3.6 that shows the mean sea extent for March and September as light blue contour lines. For the period 1980–2010 the model simulates a mean annual maximum sea ice extent in March that covers the entire Arctic Ocean except for the central and southwestern Barents Sea. Sea ice covers much of the Bering Sea and the Sea of Okhotsk, the Hudson and Baffin Bays, and some part of the Labrador Sea and the Greenland Sea. The minimum extent in September covers most of the Arctic Ocean with the exception of the vicinity of the Canadian coast, some of the Laptev Sea, and the Kara and Barents Seas. Much of the Canadian Arctic Archipelago has sea ice in September too, as well as the north-western part of the Greenland Sea. The simulations of sea ice extent are rather similar to observations shown on Figure 1.3.

Figure 3.6 also presents the simulated sea ice thickness. The maximum values in March reach 2.5 meters in the East Siberian Sea, around the Canadian Arctic Archipelago and northern Greenland, and are generally between 2 and 2.5 meters over much of the

Arctic Ocean. The simulated maximum Arctic sea ice cover is thinner only in the Eurasian Basin, between 1 and 2 meters. The mean values for the minimum in September are above 0.5 meters over much of the Arctic, reaching 1.4 meters in the Central Arctic. Compared to observations on Figure 1.3, the model overestimates the thickness of the ice close to Siberia, and underestimates it in the Canadian Arctic.
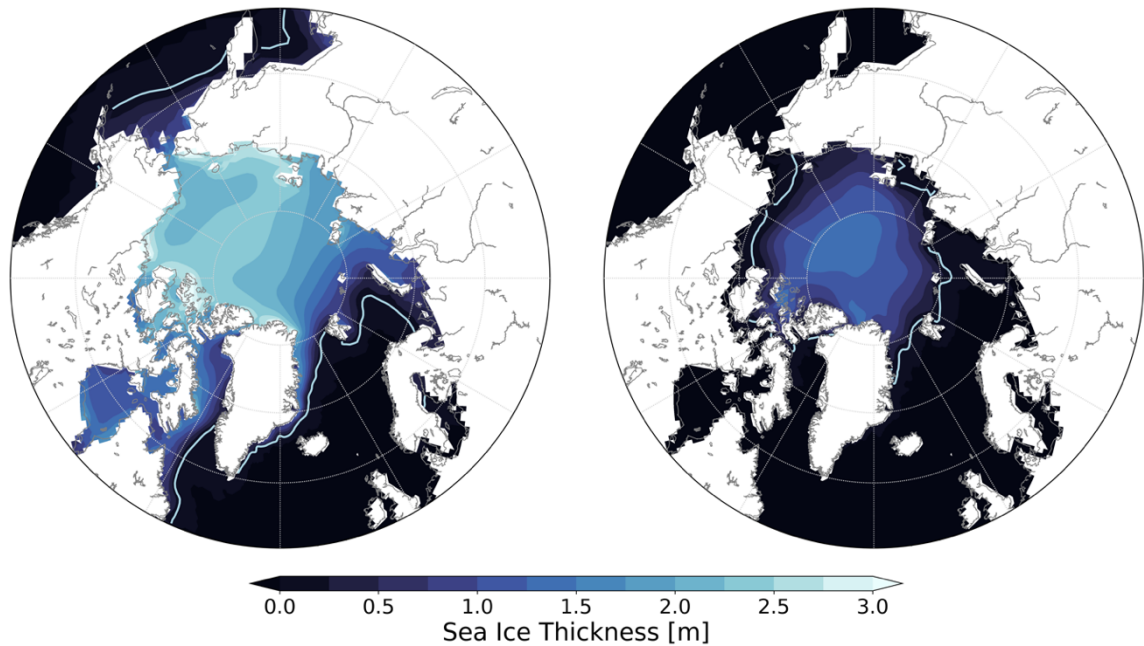

Figure 3.6. Mean sea ice thickness from MPI-ESM simulations as ensemble mean of 10 fully coupled control runs for the period 1980–2010 for (left) March and (right) September. The light blue line shows the 0.1 m edge.
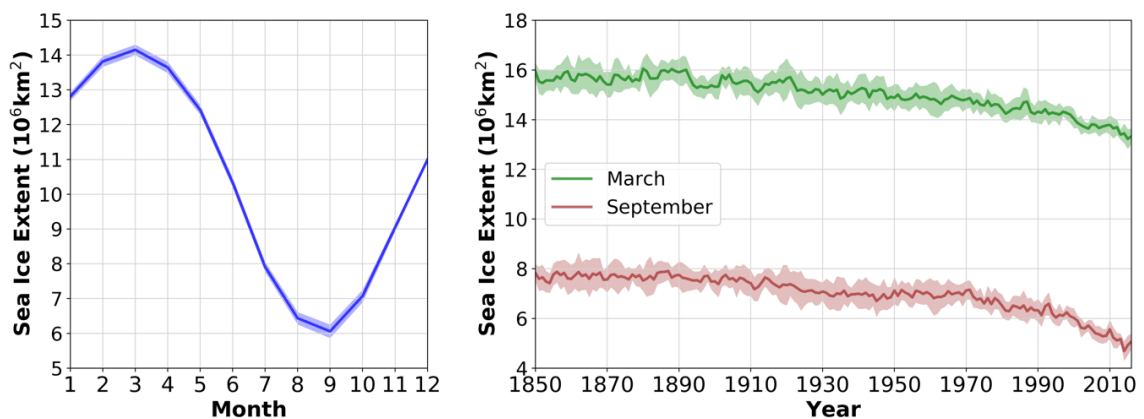
Figure 3.7. Sea Ice Extent in the Northern Hemisphere from fully coupled control runs. Left: seasonal cycle averaged over 1980–2010. Right: time series of March and September means. Solid line indicates the mean, shaded area indicates the standard deviation of 10 ensemble members.

Sea ice cover exhibits strong seasonality. The simulated seasonal cycle is presented on the left panel of Figure 3.7, showing the monthly mean values of sea ice extent in the Northern Hemisphere. Based on the ensemble mean of 10 members for 1980–2010, the highest extent is in March, 14.15×10^6 km². The lowest is in September, 6.05×10^6 km². The

plot shows the ensemble variability too as a shaded area around the solid line that represents the ensemble mean. This shows a good agreement between members with small differences. The right panel of Figure 3.7 presents time series of simulated Northern Hemispheric sea ice extent for March and September from 1850 to 2016, corresponding to the annual maximum and minimum values. March values are around 16×10^6 km^2 in the 19th century, then begin to decrease at an accelerating speed: the simulated extent slowly decreases to 15×10^6 km^2 by 1950, to 14×10^6 km^2 by 2000, and approach 13×10^6 km^2 by 2016. The September extent shows a more rapid decline. Values are close to 8×10^6 km^2 in the beginning of the model integration, stay around or above 7×10^6 km^2 until 1970, and then show a strong negative trend, and drop to 5×10^6 km^2 by 2016.

3.2.   Freshwater Content and Fluxes

As 1 meter of sea ice thickness in the model accounts to a roughly 0.76 meter deep layer of freshwater, mean sea ice thickness values on Figure 3.6 mean about 1.5–2 meters of freshwater in most parts of the Arctic Ocean. In addition to this, simulated snow on sea ice has also been taken into account while calculating solid freshwater content; however, these solid components together are still mostly an order of magnitude smaller in comparison with the liquid component stored in water except for some shelf areas with large ice thickness and shallow water depth.
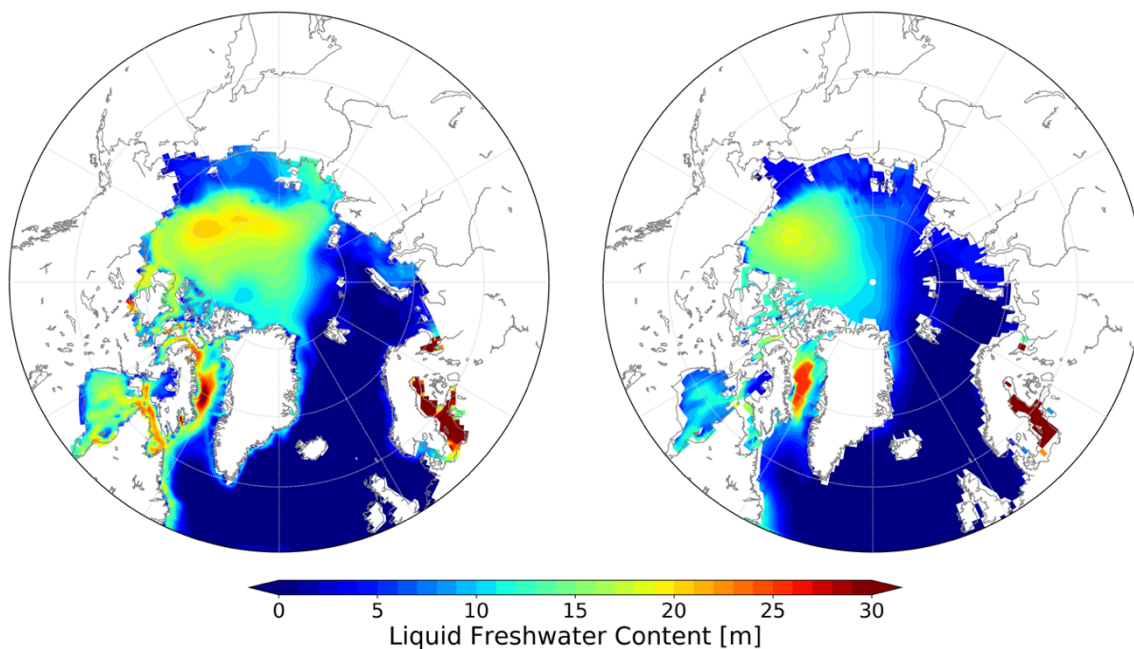

Figure 3.8. *Liquid freshwater content (S_{ref} = 34.8, integrated from surface down to the depth of S_{ref}) from (left) MPI-ESM simulations as ensemble mean of 10 fully coupled control runs for the period 1980–2010 and from (right) PHC3.0 climatology (Steele et al., 2001).*

The simulated mean liquid freshwater content for the period 1980–2010 is shown on Figure 3.8. To highlight the spatial distribution in the layers with highest variability, this map is based on an integration from surface down to the depth of S_{ref} = 34.8 surface. According to the figure, the ensemble mean liquid freshwater content from 10 fully coupled control runs totals up to a layer of between 10 and 20 meters in most of the deep Arctic Basin, similar to observations, except for parts of the Eurasian Basin where the model overestimates the content. Most of the shelf seas have lower values, about 7 meters in the East Siberian Sea and 5 meters in the Chukchi Sea; however, the content is rather high in the Laptev Sea (10–14 m), which is a significant overestimation. Freshwater content in the Canadian Archipelago (8–20 m) and in Baffin Bay (up to above 25 m) is generally close to observations. The model calculates more freshwater in Hudson Bay and in Hudson Strait (15–25 m) in comparison with observations, as well as where western boundary currents (Labrador Current, East Greenland Current) are located. Due to high salinities, freshwater content integrated down to the level of the S_{ref} = 34.8 surface in much of the Barents Sea, and in the open Nordic Seas and North Atlantic Ocean is zero (see surface salinities on Figure 3.3).
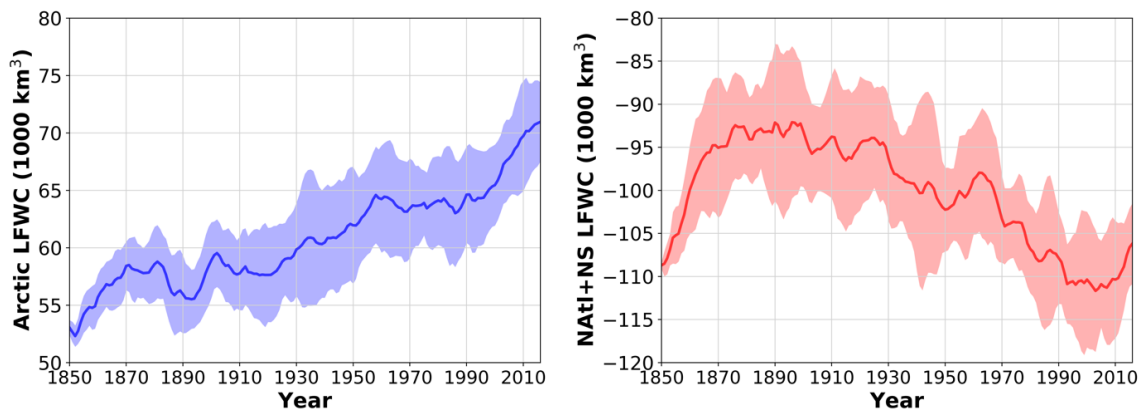

Figure 3.9. *Time series of annual liquid freshwater content (S_{ref} = 34.8, integrated in full vertical column) from fully coupled MPI-ESM simulations (left) in the Arctic Ocean, and (right) in the Subarctic North Atlantic (the Subpolar North Atlantic Ocean and the Nordic Seas). Solid line indicates the mean, shaded area indicates the standard deviation of 10 ensemble members.*

Figure 3.9 shows time series of liquid freshwater content in the Arctic Ocean, and in the Subarctic North Atlantic (comprising the Subpolar North Atlantic Ocean and the Nordic Seas) for 1850–2016. Here and in the following the liquid freshwater content refers to an integrated value in the full water column relative to S_{ref} = 34.8. The time mean for the Arctic Ocean is 60,800 km³ with a positive trend starting from below 54,000 km³ in 1850, increasing slowly to 65,000 km³ around 1990, and reaching above 70,000 km³ with a stronger trend in the last 20 years of the simulation. The ensemble spread is around 4,000 km³. The time mean for the Subarctic North Atlantic is -100,200 km³ The time series is characterised by a strong positive trend in the first 20 years of the simulation, and then

a negative trend after some stagnation from around -92,000 km^3 to below -110,000 km^3 by 1990. The last years of the simulation period show an increase again. The ensemble spread is usually around 5,000–8,000 km^3. Due to the clear sign of a spin-up in the anomalous trend during the first years, the further analysis of freshwater considers only the years 1870–2016.

The simulated freshwater content shows significant biases both for the Arctic Ocean and for the Subarctic North Atlantic, but the freshwater fluxes between their domains are much closer to observations. The time means of net annual values are shown in Table 3 both for the liquid and the solid fluxes. The liquid freshwater fluxes are generally well represented in MPI-ESM with deviations within 15% from observations listed by Haine et al. (2015), except for the Barents Sea Opening, where the southward flux is greatly overestimated by the model. The solid freshwater flux is much more difficult to simulate, as sea ice transport has high variability. A substantial net solid flux is observed only in Fram Strait; there is much less ice exported from the Arctic across other gateways (Haine et al., 2015). In MPI-ESM the Fram Strait flux is underestimated, and there is a significant export of sea ice through the Canadian Arctic Archipelago and Davis Strait too.

Section	Net liquid FW flux [km^{3}yr^{-1}]	Net solid FW flux [km^{3}yr^{-1}]
Bering Strait	2090 ± 100	4.5 ± 21.5
Canadian Archipelago	-2890 ± 160	-570 ± 30
Davis Strait	-3170 ± 160	-810 ± 30
Fram Strait	-2910 ± 150	-1700 ± 120
Barents Sea Opening	-660 ± 90	-72 ± 27

Table 3. *Net freshwater fluxes across sections bordering the Arctic and the Subpolar North Atlantic Oceans from fully coupled MPI-ESM simulations for the period 1980–2010. Values are based on the mean, the uncertainties on the standard deviation of 10 ensemble members. Negative values indicate southward transport.*

The simulated time series for the fluxes are presented on Figure 3.10. The liquid freshwater inflow through Bering Strait shows a positive trend, similar to observations. The amount of freshwater exported from the Arctic through the Canadian Arctic Archipelago is highly variable in the model, with no apparent trend in the time series of the liquid component. The solid freshwater flux shows a negative trend. The observed trends are negative for the liquid, and positive for the solid component. The simulated fluxes show the strongest trends in Fram Strait. The liquid freshwater flux is increasing, while the solid component has a negative trend. Both agree with the sign of trends in observations, although the simulated increase of the liquid component is much stronger in the last two decades of model simulations. Its annual values even reach -4000 km^3 after 2010. The trends are positive and negative for the liquid and solid fluxes across the Barents

Sea Opening, yielding an increase of total freshwater flux for the simulated period. However, there is almost no trend in the last two decades, similarly to observations.
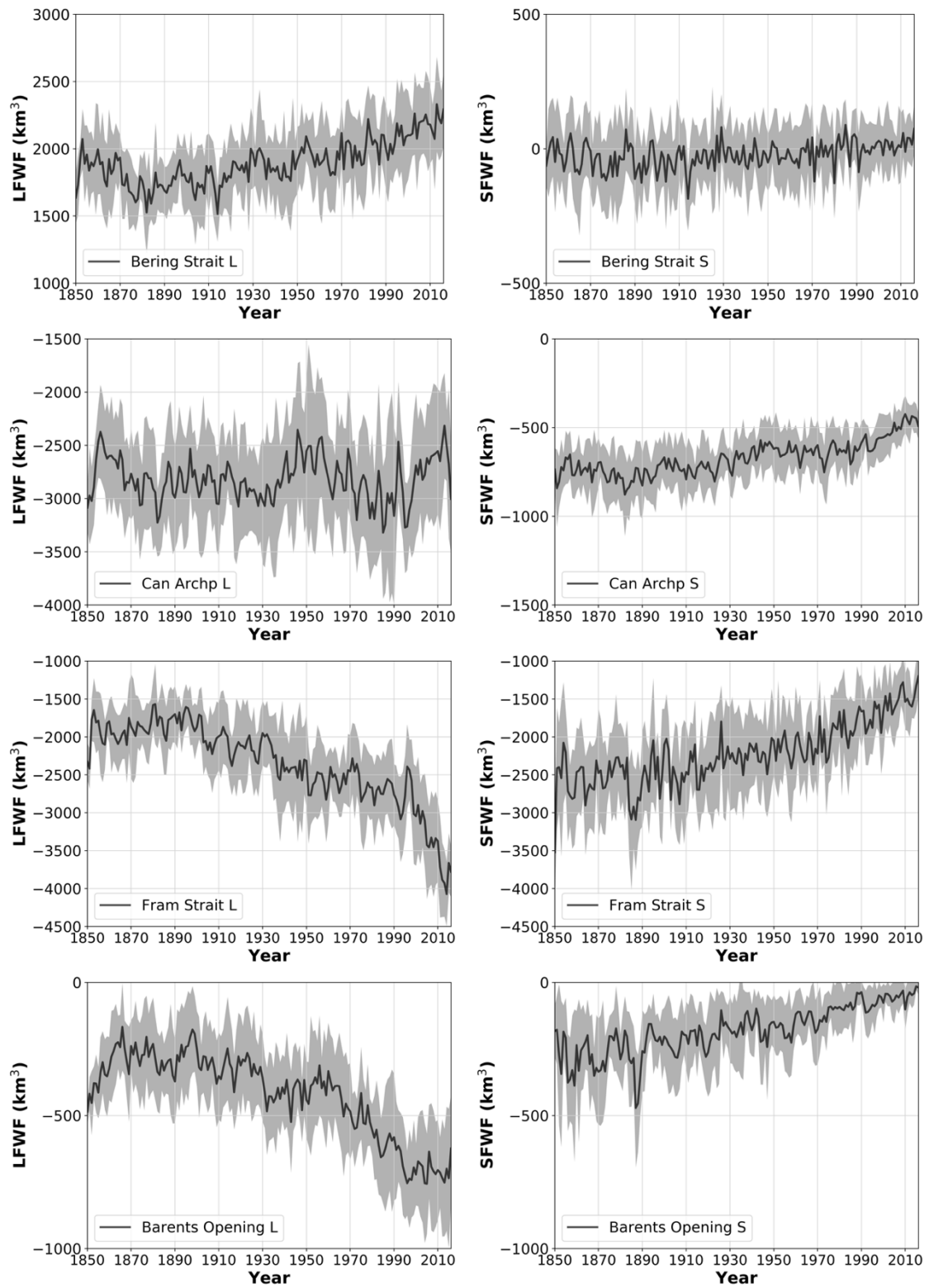

Figure 3.10. *Time series of annual net freshwater (left: liquid; right: solid) fluxes across sections from fully coupled MPI-ESM simulations. Solid line indicates the mean, shaded area indicates the standard deviation of 10 ensemble members. Negative values indicate southward transport.*

The variability of the lateral freshwater fluxes is particularly important. The comparison of their time series with the evolution of freshwater content shows a remarkable agreement. This is presented on Figure 3.11 where annual means of the total freshwater content are plotted together with the sum of the cumulative total oceanic freshwater fluxes across all bordering sections in both the Arctic Ocean (these are the Bering Strait, the Canadian Arctic Archipelago, Fram Strait, and the Barents Opening), and in the Subarctic North Atlantic (bordered by the Canadian Arctic Archipelago, Fram Strait, the Barents Sea Opening, and the 50°N section in the North Atlantic). In the Arctic Ocean the correlation between the detrended time series of total freshwater content and the cumulative lateral fluxes across sections bordering its domain is r=0.92. This relationship is rather stable in time, and the temporal anomalies and the ensemble spread are of similar size too. In the Subarctic North Atlantic the correlation coefficient is r=0.76. The anomalies and the ensemble spread of the content and the fluxes are similar, but they have somewhat different trends. This is why their time series still show differences after the removal of their linear trends.
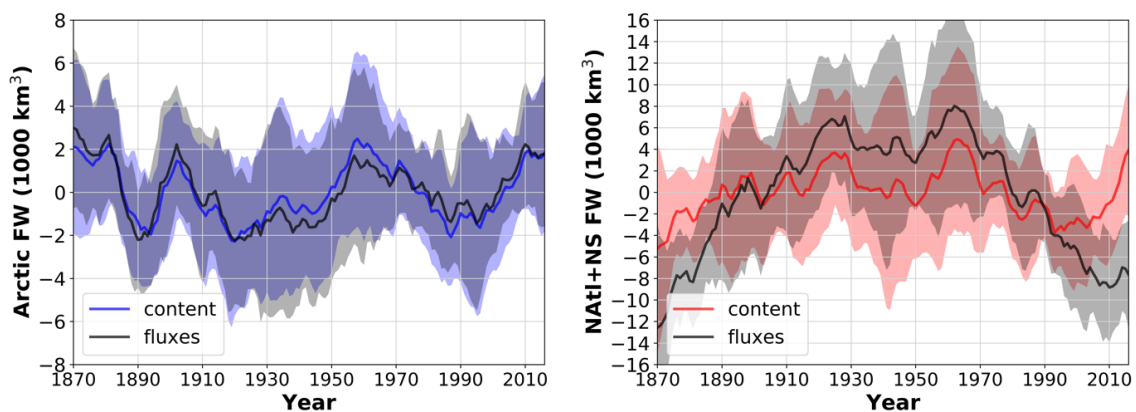

Figure 3.11. *Time series of detrended annual total freshwater content in the domain of, and cumulative total freshwater fluxes across sections around the Arctic Ocean (left), and the Subarctic North Atlantic (right) from fully coupled MPI-ESM simulations. Solid line indicates the mean, shaded area indicates the standard deviation of 10 ensemble members.*

Finally, the comparison of the total (liquid and solid) freshwater content of the Arctic Ocean and the Subarctic North Atlantic are plotted on Figure 3.12. The simulated time series show somewhat larger anomalies in the Subarctic North Atlantic, especially if the ensemble variability is also considered, but the variations in the two domains are still comparable. The correlation for the entire time period of 1870–2016 is r=-0.01, but focusing on multidecadal sub-periods reveals an unstable relationship. There are time periods where the freshwater content of the two domains anti-correlate (1880–1920: r=-0.52, 1920–1950: r=-0.60), but in other multidecadal periods a positive correlation can be seen (1950–2016: r=0.71). The picture is even less clear if the relationship is assessed in individual members of the ensemble instead of their means. This is done in the following chapter that

focuses on the internal variability of the model by presenting results of freshwater simulations from individual members of the ensemble, and discusses their differences.
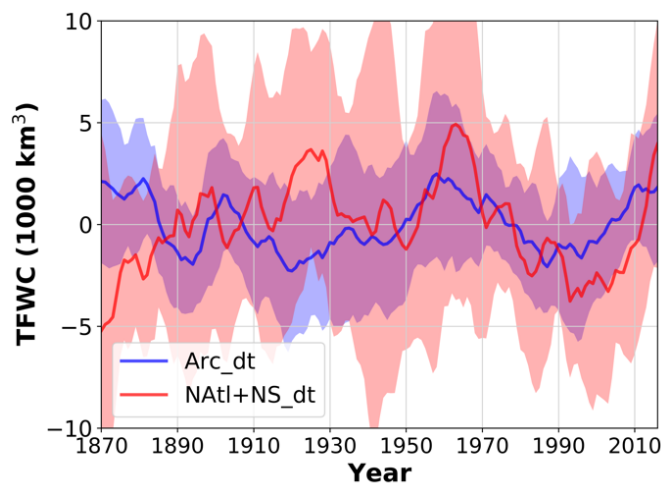

Figure 3.12. Time series of detrended annual total (liquid and solid) freshwater content from fully coupled MPI-ESM simulations in the Arctic Ocean, and in the Subarctic North Atlantic. Solid line indicates the mean, shaded area indicates the standard deviation of 10 ensemble members.

3.3.   Internal Variability

The results from previous chapters are based on an ensemble mean, that is, on the arithmetic mean of results from 10 model runs with identical setup, model physics, and forcing. The only difference between them was a perturbation of the initial conditions (see Experiment Design in Chapter 2.3). The advantage of running an ensemble is that it enables the assessment of the internal variability of the system within the boundaries of the model setup. Calculating and using the mean across the ensemble is useful because it can provide information about the mean states and the long-term evolution of parameters with more certainty; however, the signal of large amplitude events in individual members is suppressed by averaging across the members in an unconstrained system like the fully coupled MPI-ESM. Therefore, in order to evaluate freshwater anomalies that are such events, a deeper analysis of the ensemble is necessary.

First the long-term average of liquid freshwater content is analysed based on a comparison of individual members of the ensemble and the ensemble mean (Figure 3.13). These values are based on an integration in the full water column. Comparing the members of the ensemble, the biggest differences are in the Arctic, in particular in the Eurasian Basin, where the deviation from the ensemble mean can be larger than 2 meters in some members, while the ensemble mean is generally between 0 and -15 meters. The difference between members can be higher than 5 meters (compare members 02 and 03 for example). The simulated means of liquid freshwater are more stable in the rest of the

Arctic Ocean, although a few members show differences in the Canada Basin as well (in particular members 04, 07, 09). In the Nordic Seas four members show anomalies larger than 1 meters, where the ensemble mean is mostly between -20 and -30 meters. The ensemble mean in the open Subpolar North Atlantic Ocean is around -30 meters in the western basin, and around -35 meters in the eastern basin. Deviations from these in ensemble members range to 1 and 2 meters, respectively.
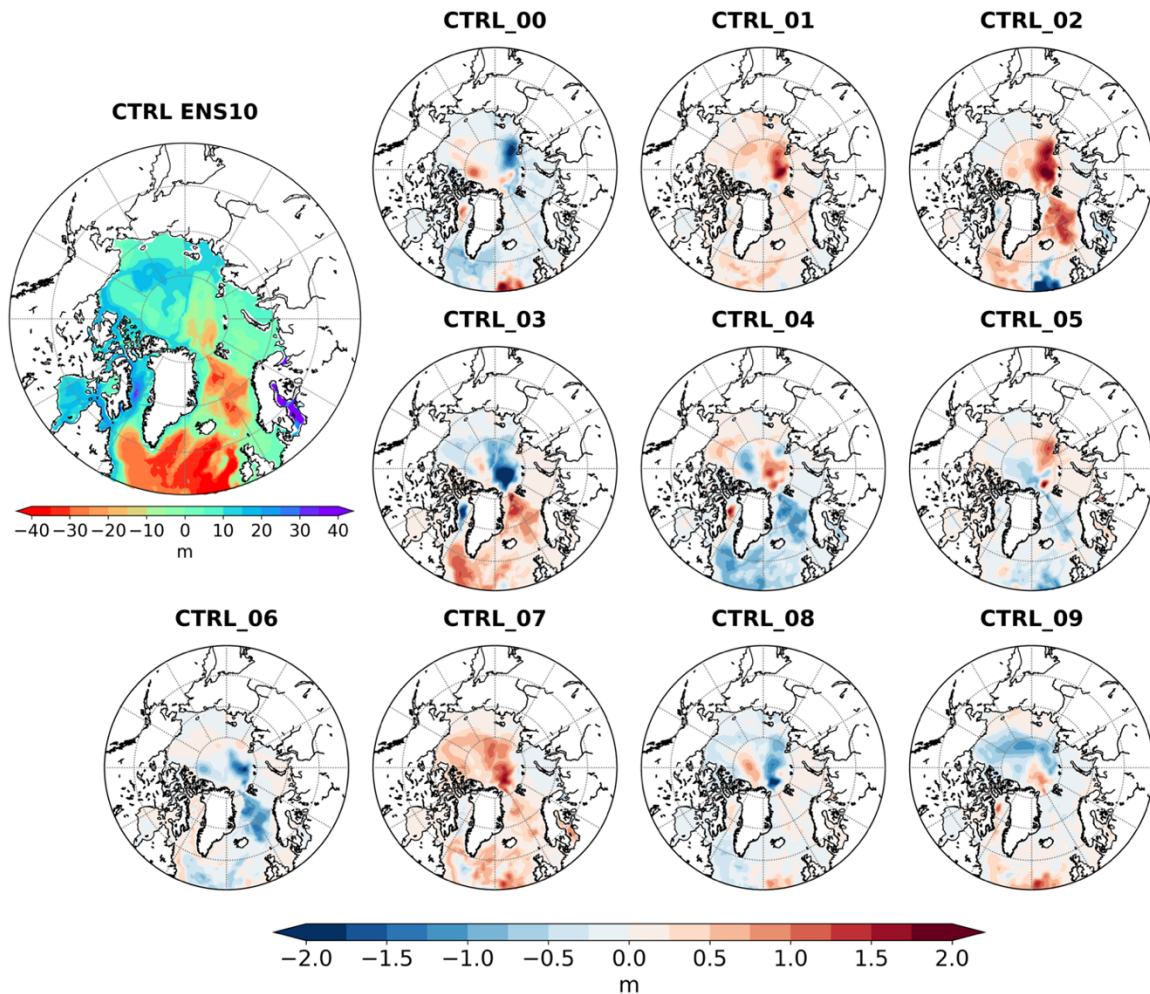

Figure 3.13. *Averages of annual liquid freshwater content (1870–2016) from fully coupled MPI-ESM simulations. Deviation of each ensemble member (CTRL_00–09) from the ensemble mean of averages (CTRL ENS10).*

In the next step, the temporal variability of liquid freshwater content in the ensemble is assessed. Figure 3.14 presents maps of the standard deviation of annual values based on the ensemble mean, and on individual members of the ensemble. In the Arctic, the ensemble mean shows the largest temporal variability in the Eurasian Basin, where the standard deviation of annual values reaches up to 3.5 meters. There is also a considerable variability present in the Canada Basin, up to 2.5 meters in the Beaufort Gyre and also south of the Alpha Ridge. The Arctic shelf seas show low variability below 1 meter. Liquid freshwater content simulations are rather stable in the Nordic Seas with values generally

around 1 meter, and up to 1.5 meters along the Norwegian Current and the East Greenland Current. The largest variability is seen in the Subpolar North Atlantic Ocean: there values mostly exceed 2.5 meters, up to 3.5 in the western, and to 4 meters in the eastern basin. Comparing these with results from individual ensemble members, the variability appears to be even larger.
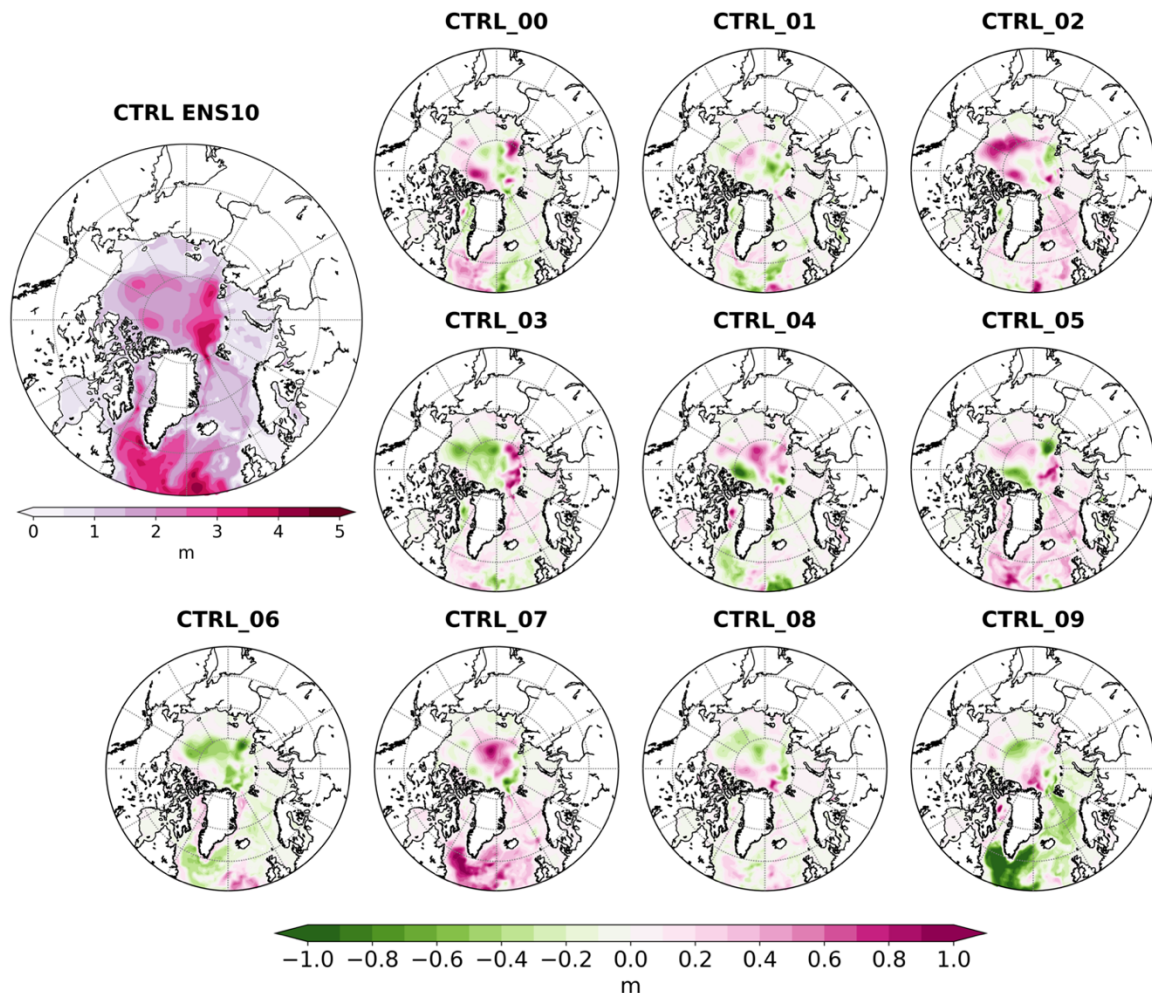

Figure 3.14. *Temporal standard deviations of annual liquid freshwater content (1870–2016) from fully coupled MPI-ESM simulations. Deviation of each ensemble member (CTRL_00–09) from the ensemble mean of standard deviations (CTRL ENS10).*

The standard deviations differ from those in the ensemble mean by up to 1 meter in more regions (smaller plots on Figure 3.14). In the Arctic Ocean for example the variability in the Eurasian Basin is almost comparable to that in the Beaufort Gyre in a few members (e.g. 02, 07), while in most of them it is much larger; in a few members values barely reach 2 meters in the Beaufort Gyre, but reach up to above 4 north of Svalbard (e.g. 03, 06, 08). Variability in the Nordic Seas is relatively similar across the ensemble, while in the North Atlantic there are large differences, especially in the western basin. There the standard deviation of annual values ranges from below 3 (09) to above 4.5 meters (07).

Differences across the ensemble in terms of solid freshwater content, i.e. sea ice are plotted on Figure 3.15. According to the figure, the standard deviation of 10 ensemble climatologies of sea ice thickness exceed 0.1 meters in some regions both in winter and summer. Values based on differences of the 1980–2010 averages for March vary up to 0.15 meters in the coastal areas of the Beaufort Sea and in the Chukchi and East Siberian Seas, and are above 0.1 meters north of Greenland, in Fram Strait, and along the export pathways of sea ice following the East Greenland Current. The ensemble mean sea ice thickness in these regions is above 2.5 meters (compare Figure 3.6) except for along the East Greenland Current, where it is between 1 and 1.75 meters. The ensemble variability is below 0.1 meters in the rest of the Arctic Ocean and 0.05 meters at lower latitudes with the exception of a small area east of Svalbard and along the varying winter ice edge in the Labrador Sea. Although the mean sea ice thickness is considerably smaller in September, the ensemble variability is larger: it is above 0.1 meters in most of the Arctic Ocean, and close to 0.15 meters in many coastal areas, where the ensemble average ranges down to below 0.5 meters (compare again Figure 3.6). Outside the Arctic Ocean there is no considerable variability due to lack of summer ice in all ensemble members.
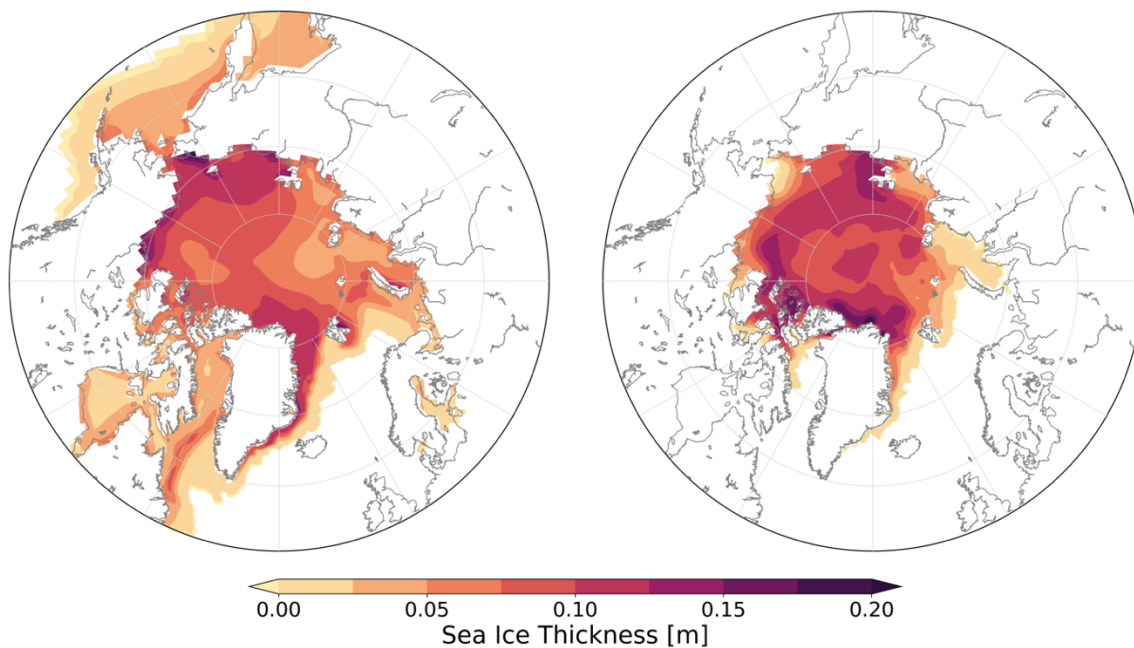

Figure 3.15. *Sea ice thickness variability from fully coupled MPI-ESM simulations. Temporal standard deviation of 1980–2010 averages of 10 ensemble members for (left) March and (right) September.*

As suggested by the similar ensemble spread for total freshwater content and fluxes on Figure 3.11, the relationship is robust across the ensemble. All individual members show a significant correlation in both domains (not shown), supporting the result from the ensemble mean that most of the temporal variability of the freshwater content can be explained by the variability in the lateral fluxes through sections bordering their domains.
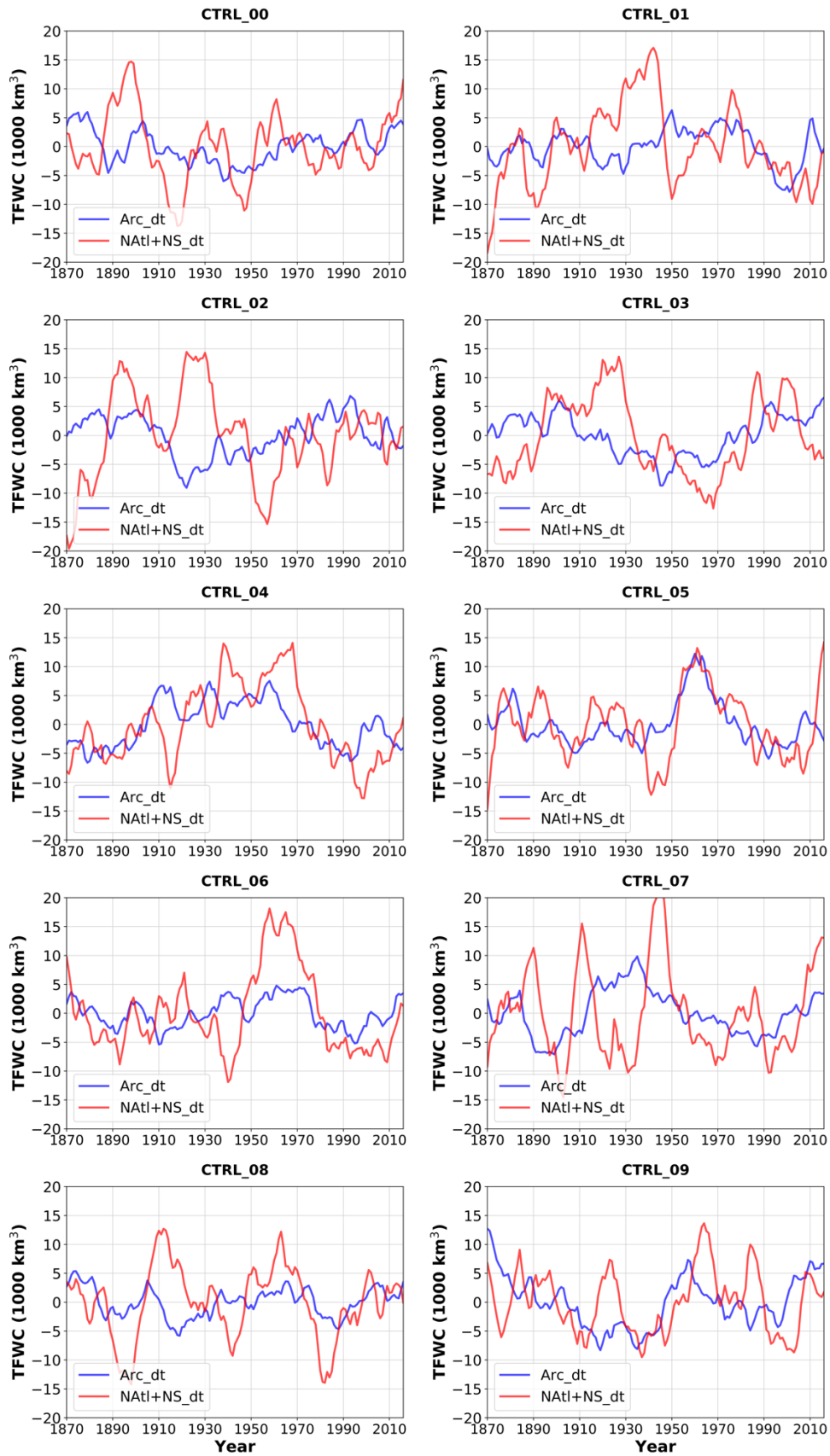
Figure 3.16. *Time series of detrended annual total (liquid and solid) freshwater content from 10 ensemble members of fully coupled MPI-ESM simulations in the Arctic Ocean and in the Subarctic North Atlantic.*

Finally, the connection between the total freshwater content in the Arctic Ocean and in the Subarctic North Atlantic is presented on Figure 3.16 by their time series similarly as on Figure 3.12, but here for each individual ensemble member. While anomalies based on the ensemble mean have a relatively similar size, Figure 3.16 suggests that this can be attributed to the masking of variability in the ensemble mean, since in individual members the anomalies in the Subarctic North Atlantic domain are twice the size of those in the Arctic. Still, there are multidecadal periods in most members where the anomalies are temporarily of similar size and opposite sign (notable examples are CTRL_00 in 1870–1910, CTRL_02 in 1965–2010, CTRL_04 in 1870–1910, CTRL_05 in 1980-2000, CTRL_09 in 1880–1915).

3.4.   Discussion

The results show that the model reproduces the main characteristics of large-scale ocean circulation in the Arctic and the North Atlantic Oceans. In coupled model simulations, the proper representation of the ocean surface, in particular the SST and sea ice are very important as they mediate the air-ocean fluxes. The rate of precipitation, evaporation, and river runoff are tightly linked to other components of the climate system, therefore the sea surface salinity and the freshwater content are good indicators of the coupling performance of the model (Jungclaus et al., 2013).

The performance of the ocean simulations of MPI-ESM has been analysed by Jungclaus et al. (2013). They noted that although the model results of temperature and salinity exhibit only small drifts after a sufficient spin-up length, there are still serious biases especially at intermediate levels. The surface conditions presented above are generally closer to observations, but still show some biases. These match the findings of Jungclaus et al. (2013), who have investigated the possible reasons. They found that in the North Atlantic Ocean, the simulated SST is too low because the North Atlantic Current is too zonally oriented. This is most likely because the Gulf Stream separation is improperly represented due to resolution limitations. The Atlantic Water thus loses too little heat, and it is too warm when it reaches the Nordic Seas and the Barents Sea, explaining the warm bias in these regions. Jungclaus et al. (2013) attributed the large fresh bias in the salinity of Siberian shelf seas to the overestimation of river runoff of Eurasian rivers, a known bias of the model (Hagemann et al., 2013).

The effect of salinity biases is apparent in the calculated liquid freshwater content as well: the model overestimates it in the Arctic Ocean, and underestimates it in the Subarctic North Atlantic. Nevertheless, the range of their interannual variability is similar to observations that show examples of decadal anomalies of up to about 7,000 km^3 in 10 years

in the Arctic (Rabe et al., 2014), and up to about 13,000 km^3 in the Subarctic North Atlantic (Boyer et al., 2007). Moreover, the simulated lateral oceanic freshwater fluxes are also similar to those listed by Haine et al. (2015), and their biases are within the range of those in regional ocean-sea ice models investigated by Aksenov et al. (2016). As the objective was to simulate the freshwater anomalies in these domains, model runs of the MPI-ESM can be considered a suitable tool, because this study is focusing on the analysis of the changes in freshwater content and fluxes, rather than on a precise representation of their mean states.

The model results show that for both domains, most of the variability of the total freshwater content can be represented by the variability of the lateral fluxes. This highlights the importance of the changes of water transport across their borders, especially for the Arctic Ocean whose domain is rather closed. As the Arctic Ocean and the Subarctic North Atlantic share most of their borders, it is reasonable to assume a link between their freshwater budgets. This has been suggested by many studies before, in particular while investigating the origin of Great Salinity Anomalies in the North Atlantic (e.g. Dickson et al., 1988; Aagaard and Carmack, 1989; Häkkinen, 1993; Belkin et al., 1998; Proshutinsky et al., 2002; Haak et al., 2003; Belkin, 2004; Karcher et al., 2005). Although the time series of reliable observations are still rather short, the comparison of observed freshwater content in the Arctic Ocean and in the Subarctic North Atlantic shows a remarkable connection in recent decades with a significant anticorrelation. The size and timing of their respective anomalies could even suggest an oscillation (Horn, 2018).

The fully coupled MPI-ESM is not constrained by observations, therefore it cannot reproduce the timing of the observed freshwater anomalies. But its simulations enable the analysis of anomalies associated with the internal variability of the climate system for a much longer time period than what is covered by observations. The model results for more than 150 years presented above show an unstable relationship between the time series of the Arctic and the Subarctic North Atlantic freshwater content. Their simulated freshwater budgets do show some opposing variability, but this is not persistent enough to result in an anticorrelation over the whole time series. Their correlation varies greatly depending on the selected sub-period of time and member of the ensemble.

The freshwater content and the total cumulative lateral fluxes agree well for both domains, and thus variations in the air-ocean fluxes and river runoff play only a minor role. But even if they are ignored, the system is still not closed—anomalies of freshwater transport through Bering Strait and the Atlantic 50°N section are not directly related to the amount of freshwater exchanged between the Arctic and the Subarctic North Atlantic. Variations in the simulated freshwater input through Bering Strait are relatively small compared to the total net Arctic freshwater export into the Subarctic North Atlantic, similarly to the model results of Häkkinen and Proshutinsky (2004). Therefore, most of the

changes in Arctic freshwater content are tightly linked to changes in this export, and thus to changes in the Subarctic freshwater content. However, the anticorrelation between the two contents is only occasional in the simulations. The reason why it is not persistent over a longer time period is because the Subarctic North Atlantic content is driven not only by the Arctic export, but also by the freshwater flux across the 50°N section, consistent with the findings of Horn (2018). In the MPI-ESM simulations the dominant drivers are these latter transports that cause large freshwater content anomalies that are not of Arctic origin. Without these, the Arctic-Subarctic North Atlantic link would be very robust. This is illustrated by Figure 3.17.
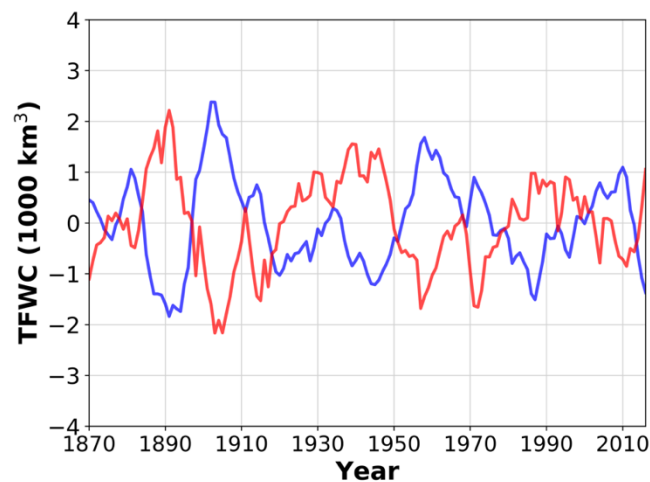

Figure 3.17. Time series of annual total (liquid and solid) freshwater content from fully coupled MPI-ESM simulations in the Arctic Ocean (in blue), and in the Subarctic North Atlantic minus the cumulative freshwater flux across the 50°N section (in red). Data shows the mean of 10 ensemble members, detrended with a 5th order polynomial function.

The time series plotted on Figure 3.17 are similar to those presented on Figure 3.12 with a few differences. The blue line shows the Arctic total freshwater content, but the red line shows the residual of Subarctic North Atlantic total freshwater content after the series of the cumulative freshwater flux across the 50°N section has been removed. Moreover, the data series have been detrended with a 5th order polynomial function in order to remove low-frequency variabilities on a time scale of a few decades and thus highlight the anomalies within a time scale similar to that of the available observations. Figure 3.17 shows a robust anticorrelation (r = -0.81, significant with above 99% confidence) that is persistent over the entire time series of the ensemble mean, and in each individual member of the ensemble as well (not shown). This suggests that on the time scale of a few decades, a seesaw of the two freshwater contents resembling an oscillation can develop as long as there are no large freshwater flux anomalies advected from the south into the Subarctic North Atlantic domain, or they are coincidently of appropriate size and sign. The modeled fluxes at the 50°N section frequently show large anomalies, obscuring the signal of the

Arctic link. This explains why the existing periods with anticorrelation are only temporary, and not dominant in the full simulation period.

The seesaw in freshwater content between the Arctic Ocean and the Subarctic North Atlantic is dominated by the liquid component. This is shown on Figure 3.18 that displays the same time series as Figure 3.17, and additionally the separate Arctic liquid (dashed blue) and solid (light blue) components, as well as the Subarctic liquid component (dashed red). The solid and dashed red lines match very closely, indicating the negligible contribution of the solid component to the total Subarctic North Atlantic freshwater budget. In the Arctic Ocean, variations of the liquid component dominate the changes of the total content, but occasionally the solid component can also be important (see for example the anomalies in the early 1970s on Figure 3.18). This suggests that over a longer time scale the seesaw is mostly driven by exchanges of liquid freshwater between the two basins, but there is a potential for events driven by anomalous sea ice export as well.
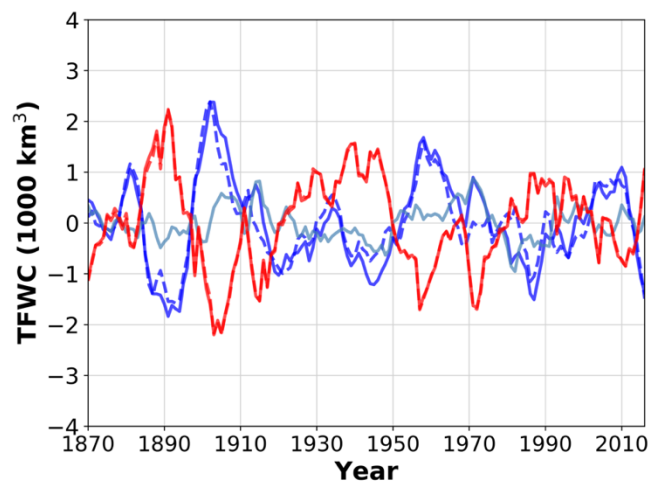

Figure 3.18. Time series of annual freshwater content from fully coupled MPI-ESM simulations in the Arctic Ocean (blue: total; dashed blue: liquid; light blue: solid), and in the Subarctic North Atlantic minus the cumulative freshwater flux across the 50°N section (red: total; dashed red: liquid). Data shows the mean of 10 ensemble members, detrended with a 5th order polynomial function.

Some of the repeatedly observed large Subarctic North Atlantic freshwater content anomalies in the recent decades have been found to indeed originate in the Arctic Ocean. The source of the 1970s event was most likely an anomalously large ice export through Fram Strait (Aagaard and Carmack, 1989; Häkkinen, 1993), and the 1990s event has been linked to a release of liquid freshwater from the Arctic (Karcher et al., 2005). The model simulations presented here confirm the potential for both liquid and solid freshwater export from the Arctic to dilute the Subarctic North Atlantic. The frequency and the time frame of these simulated events are also similar to what has been observed.

However, the results show no sign of large Subarctic North Atlantic freshwater anomalies that are independent from both the Arctic export and the flux at the 50°N

section, while for example the freshwater anomaly observed in the 1980s was likely a non-advective event. Instead, it has been linked to local processes in the Labrador Sea, with only a possible supplement of anomalous liquid freshwater export from the Arctic (Belkin et al., 1998), since local processes, for example deep convection can also trigger changes in the ocean circulation that can cause anomalous freshwater export from the Arctic (Wu and Wood, 2008). A possible reason for the absence of locally induced anomalies within the Subarctic North Atlantic in the model analysis presented here is that they were observed in the upper several hundred meters layer, while here the freshwater content was calculated by integrating in the full vertical column of the entire basin. A locally induced anomaly that is at least partly due to redistribution of freshwater within the region is thus not likely to be traceable in the metric used here.

3.5.   Conclusions

The aim of the work presented in this chapter was to simulate the ocean circulation and water exchanges in and around the Arctic Ocean and the Subpolar North Atlantic Ocean, with a particular focus on freshwater content anomalies. The results show that the applied model, the fully coupled MPI-ESM performs well in reproducing the large-scale features of ocean circulation. There are large biases in salinity and thus in freshwater content, which is overestimated in the Arctic, and underestimated in the North Atlantic. Nevertheless, the temporal variability in their freshwater content, as well as the simulated exchanges between their basins is similar to observations. This makes the model a suitable tool for the analysis of freshwater anomalies.

The results show that both in the Arctic Ocean and in the Subarctic North Atlantic, most of the variability in the total (liquid and solid) freshwater content can be explained by the lateral oceanic freshwater fluxes across the sections bordering their domains. This means that changes in precipitation, evaporation, or river runoff have an insignificant effect.

The comparison of the simulated freshwater content of the two domains shows a potential for their anticorrelation over a time period of a few decades, similar to what has been observed in the recent decades. However, this is not robust in time, as there are time periods with a positive correlation too, while during most of the time series there seems to be no connection at all. This is true for the ensemble mean of 10 members, and for the individual members as well that also exhibit large differences in the Arctic-Subarctic freshwater covariability.

The modeled time series of Arctic and Subarctic North Atlantic freshwater content presented here suggest that their observed anticorrelation in the recent decades is not

likely to persist in the future, as it occurs only temporarily in the simulations. The link between their domains appears to be rather stable, dominated by the exchange of liquid freshwater between their basins. This implies that the potential for their anticorrelation could remain similar regardless of the loss of sea ice that is observed in the Arctic (Kwok et al., 2013), a trend that is expected to continue in the 21st century, along with a decrease in ice export (Haine et al., 2015). However, the signal of the link is mostly masked by much larger anomalies in the Subarctic North Atlantic that are advected from the south, and are not directly related to the freshwater exchange with the Arctic Ocean. Still, the Arctic and the North Atlantic freshwater contents exhibit a seesaw-like balance driven by anomalous fluxes of freshwater between their basins during periods when this southern flux shows no significant anomalies, or when its anomalies coincide with the changes in the Arctic Ocean.

But what drives these freshwater fluxes? What sets their variability, especially the variability of the exchanges between the Arctic and the Subarctic North Atlantic? How different are the driving forces of the changes in the liquid, and in the solid component? The hypothesis of this study was that the changes in freshwater content are driven by wind stress forcing associated with large-scale patterns of atmospheric variability. The analysis of a possible connection between freshwater content and atmospheric variability is presented in the next chapter.

4.   The Role of Atmospheric Forcing

The previous chapter describes general characteristics of the MPI-ESM simulations, with focus on liquid freshwater content and the solid component, sea ice. According to fully coupled model runs, the Arctic and Subarctic North Atlantic freshwater budgets show some opposing freshwater variability but this is not persistent enough to result in a stable anticorrelation over a longer time scale. A detailed investigation of freshwater content and fluxes showed that the seesaw between the two freshwater contents is actually very robust, but most of the time its sign is obscured in the Subarctic North Atlantic by large anomalies that are not of Arctic origin.

Based on these results, the second objective of this study was to identify key patterns of atmospheric variability that govern the changes in Arctic and Subarctic North Atlantic freshwater content through wind forcing. This chapter presents the main characteristics of sea-level pressure and wind simulations in MPI-ESM. After deriving the NAO and AO patterns from the fully coupled model simulations, an attempt is made to identify a connection between their time series, and the simulated freshwater contents and fluxes. After no robust link can be established, a more sophisticated method is applied that is capable to identify redundant modes of sea-level pressure and freshwater variability. This enables the investigation of different drivers of freshwater anomalies in the different basins, also respective to the liquid and solid components. Finally, in order to examine the role of wind stress, part of the model experiments is repeated with prescribed wind forcing based on observations. The comparison of the fully coupled control runs and these partially coupled simulations confirms the influence of wind forcing in shaping the Arctic and Subarctic North Atlantic freshwater system.

4.1.   Simulated Atmospheric Variability in MPI-ESM

For this study, the most relevant atmospheric parameters are the sea-level pressure, and the wind speed and direction. First, these are analyzed in the model simulations of MPI-ESM.

The simulated 30-year mean sea-level pressure in the fully coupled control simulations is compared to observations (NCEPcfsr reanalysis, (Saha et al., 2010)) for the Northern Hemisphere north of 50°N on Figure 4.1. Comparing the two panels of the figure, it can be seen that the model is able to reproduce the key large scale atmospheric

features in the region, although with various inaccuracies. In the Arctic the Beaufort High is of similar magnitude (above 1017 hPa) as observed, but its position is much less confined to the Canadian side, as it extends far into the central Arctic. As a result, mean sea-level pressure is higher than 1015 hPa over almost the entire Arctic Ocean, which is a notable overestimation especially over the Eurasian Basin, where the bias is up to +4 hPa. This anomaly extends into the Barents Sea and the Nordic Seas as well, where sea-level pressure is also too high in the model. The position and extent of the Icelandic Low is very close to observations, and only about 1 hPa stronger (1003 hPa). In the Northern Pacific, however, the low-pressure regime over the Bering Sea is much smaller and weaker compared to the reanalysis. Pressure fields over land, in particular the Siberian, the Canadian, or the Greenland High have small biases both in strength and position. The mean climatology of large scale wind fields is mostly associated with pressure patterns according to geostrophy, especially over water. This can be seen comparing the pressure patterns to the following figure.
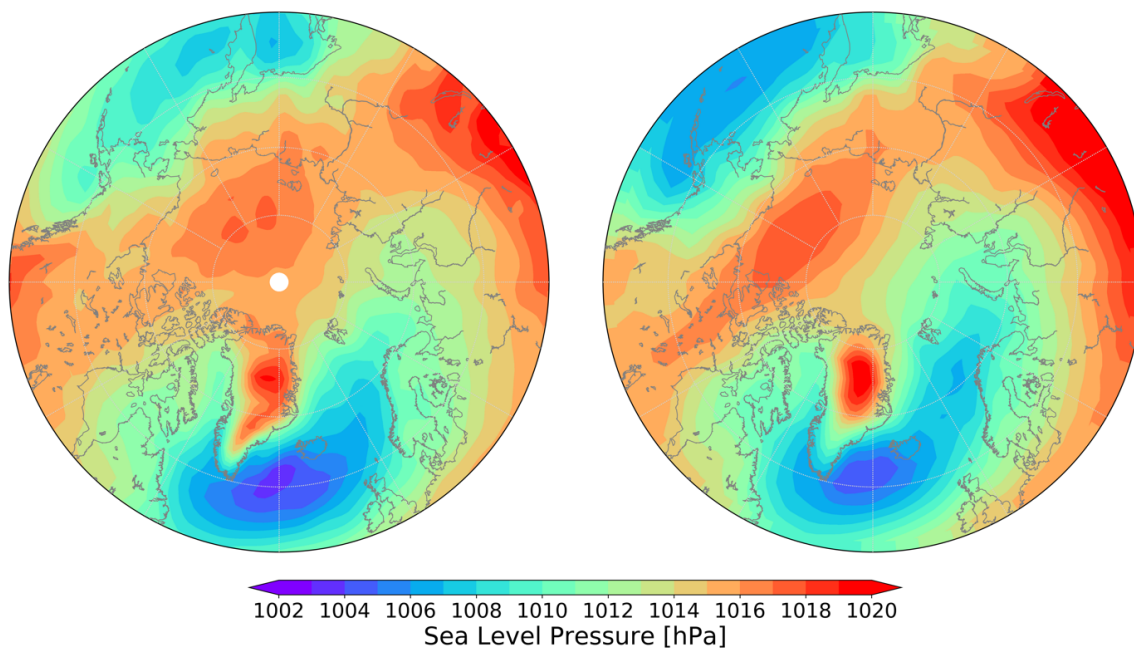

Figure 4.1: *Mean atmospheric sea-level pressure. From (left) MPI-ESM simulations as ensemble mean of 10 fully coupled control runs for the period 1980–2010 and from (right) NCEPcfsr reanalysis (Saha et al., 2010).*

Figure 4.2 shows the mean atmospheric circulation near the surface, that is, the wind velocities and directions at 10-meter level over ground or water from model simulations and from reanalysis. The model simulates the large-scale wind systems relatively well. In the Arctic, the anticyclonic circulation associated with the Beaufort High is clearly visible, although its center is displaced and its extent is larger than observed. Therefore, the winds crossing the Arctic that drive the Transpolar Drift are also less pronounced in the model.

At lower latitudes, wind directions are very similar to observations, with strong northerly winds (although somewhat too strong, with some easterly bias) along the eastern shore of Greenland, and with the dominant westerlies in the North Atlantic.
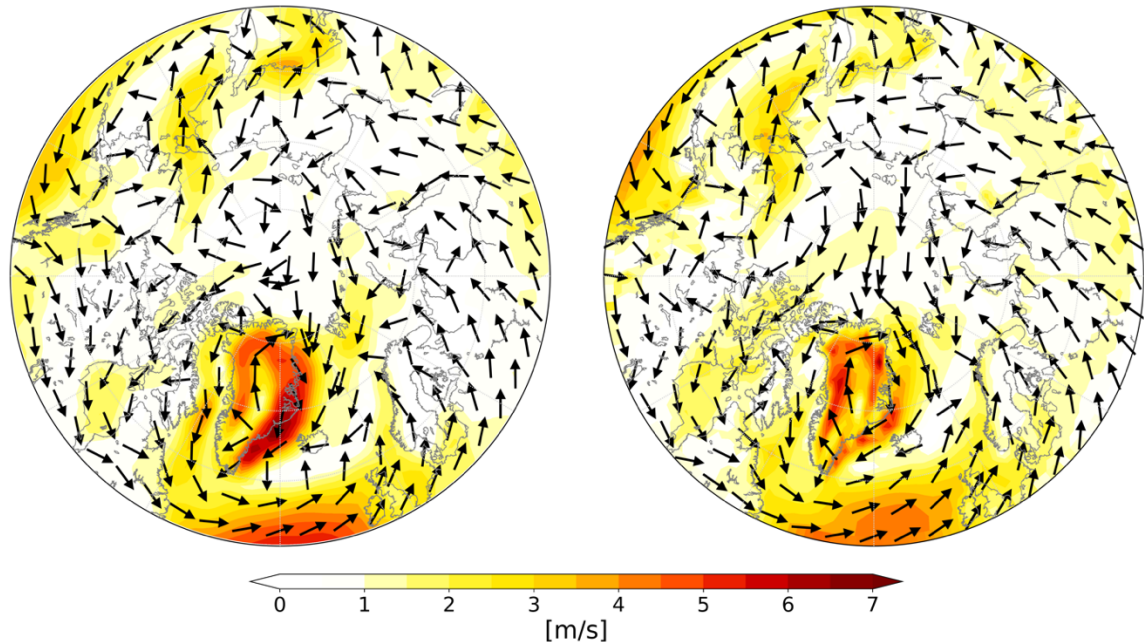

Figure 4.2. *Mean wind at 10 meters. Color shading indicates velocity, arrows show direction. From (left) MPI-ESM simulations as ensemble mean of 10 fully coupled control runs for the period 1980– 2010 and from (right) NCEPcfsr reanalysis (Saha et al., 2010)*

The mean climatology and the temporal variability of sea-level pressure is similar in different members of the model ensemble. Unlike the liquid freshwater content (Figure 3.13 and Figure 3.14), MPI-ESM simulates sea-level pressure with relatively small internal model variability. Figure 4.3 presents a comparison of long-term (1870–2016) means of sea-level pressure as differences between individual ensemble members and the ensemble mean. The largest differences across the ensemble are on the order of a few tenths of hPa. The spatial distributions of the differences are rather stochastic, and their extent is insignificant in comparison with the climatology based on the ensemble mean of all 10 members.

Differences of the temporal variability are plotted on Figure 4.4. This figure shows the temporal standard deviations of annual sea-level pressure as differences between members of the ensemble and the ensemble mean. In the ensemble mean, the standard deviations are largest over the Bering Sea (up to above 2.5 hPa), and around Iceland and Southern Greenland and over much of the Siberian shelf seas and the Central Arctic (above 2 hPa). In the western North Atlantic and over land, values are mostly below 1.5 hPa. Individual ensemble members show a rather similar variability with relatively small differences. A few members show some differences (within the range of 0.5 hPa) over the Nordic Seas or over the Canada Basin, and many of them over the Bering Sea, although

these are the regions where the variability is highest in all of them. It is also notable that differences over land are mostly smaller than over water, within the range of 0.2 hPa.
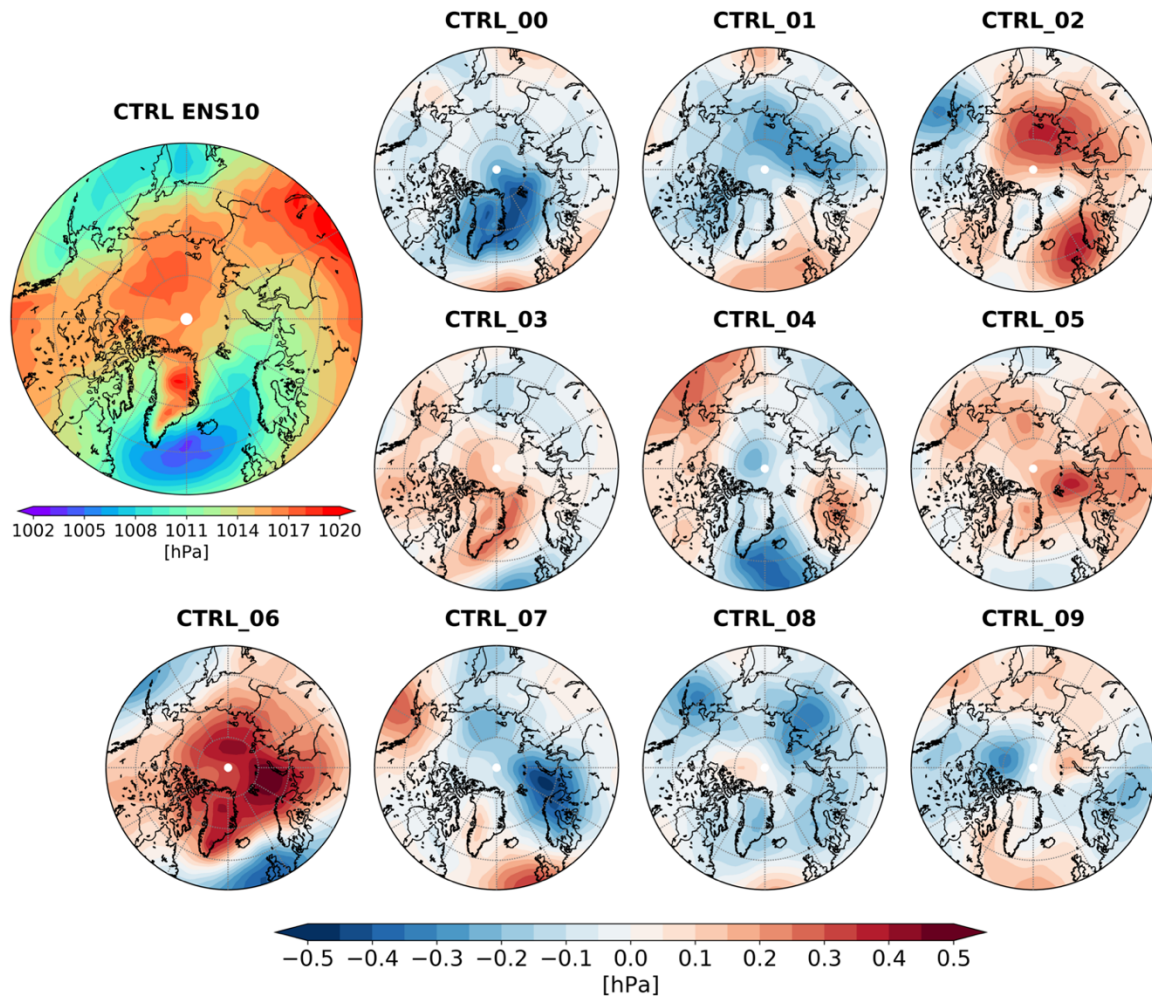

Figure 4.3. *Averages of annual atmospheric sea-level pressure (1870–2016) from fully coupled MPI-ESM simulations. Difference of each ensemble member (CTRL_00–09) in comparison with the ensemble mean of averages (CTRL ENS10).*

Overall, the mean climatology and the temporal variations of sea-level pressure (and thus the large-scale wind systems) are well simulated in MPI-ESM compared to observations. They are also rather stable within the model: there is no significant difference between the ensemble mean, and the individual members of the ensemble. This stability provides a good basis for the analysis of the connection of large scale atmospheric variability and freshwater content. The following section presents results of this analysis based on metrics that describe key modes of sea-level pressure variability, and attempts to identify those that are the most relevant in terms of their influence on freshwater variability.
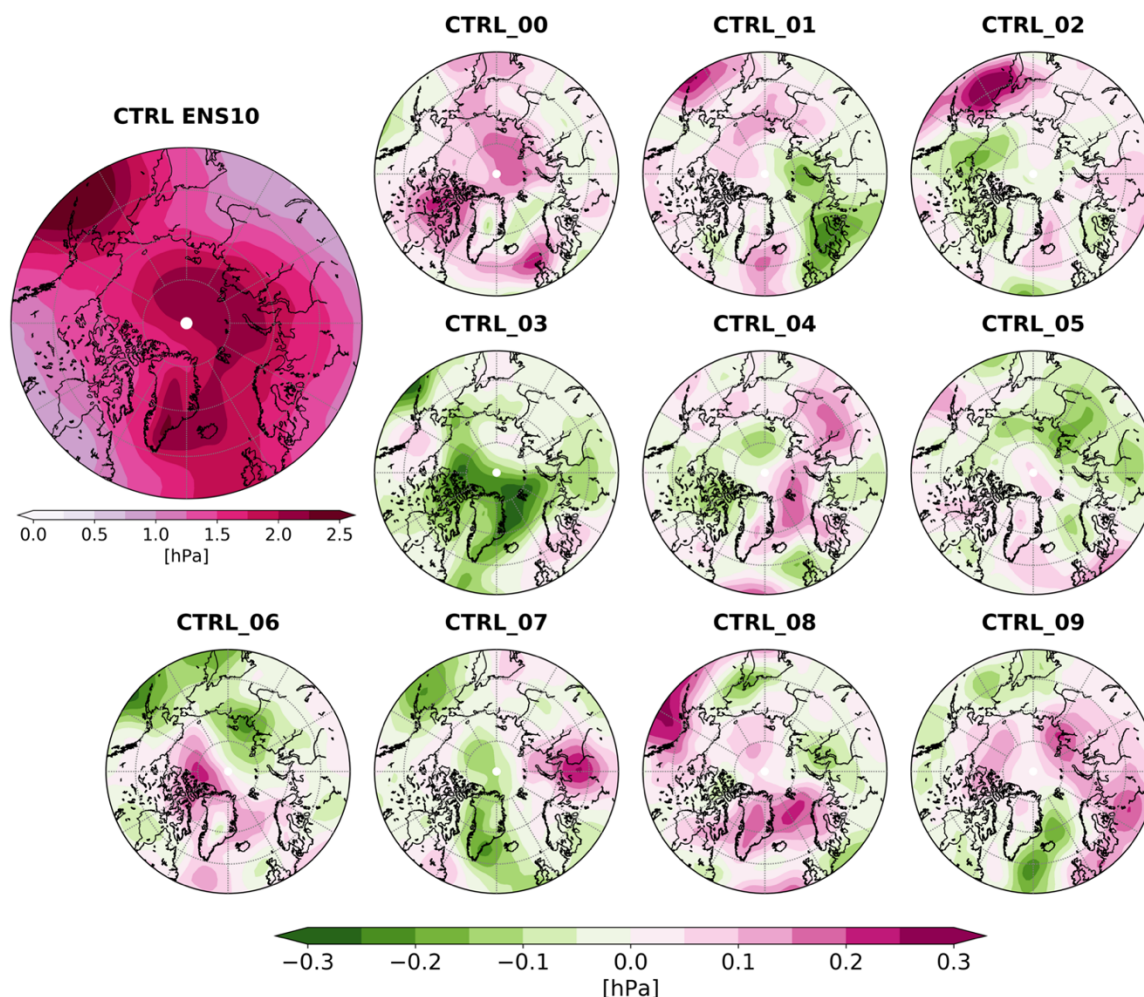
Figure 4.4. *Temporal standard deviations of annual atmospheric sea-level pressure (1870–2016) from fully coupled MPI-ESM simulations. Difference of each ensemble member (CTRL_00–09) in comparison with the ensemble mean of standard deviations (CTRL ENS10).*

4.2.   Atmospheric Drivers of Freshwater Anomalies

This section presents a detailed investigation of atmospheric sea-level pressure variability, and its impact on freshwater content in the fully coupled MPI-ESM experiments. First, the analysis of certain oscillation indices and their connection to freshwater content anomalies is performed, then results based on a comprehensive statistical analysis are presented.

4.2.1. The Link Between Oscillation Indices and Freshwater Anomalies

There are different metrics that provide information on certain aspects of atmospheric variability. In key regions of this study in the Northern Hemisphere, the Arctic Oscillation (AO) and the North Atlantic Oscillation (NAO) are widely used indices that describe major modes of low-frequency variability of sea-level pressure. These were calculated here

by performing an Empirical Orthogonal Function (EOF) analysis. This method, also known as Principal Component Analysis, is a multivariate technique used to derive main patterns of variability form a statistical field. The EOF analysis is commonly used in climate sciences to identify patterns of simultaneous variation, for example atmospheric teleconnections represented by oscillation indices. A description of the AO and the NAO can be found in Chapter 1.2.3.2—Large-scale Atmospheric Variability, and a brief introduction of the EOF analysis is given in the Appendix at the end of this thesis. This chapter presents the main characteristics of the AO and the NAO in the fully coupled MPI-ESM simulations. Then an attempt is made to find a connection between their time series and freshwater content anomalies.

Figure 4.5 presents the pattern and time series of AO in the model as the eigen vector and the principal component time series of the first EOF of sea-level pressure north of 20°N. In MPI-ESM this leading mode describes 40.9% of the sea-level pressure variability, and is characterised by a center over the Arctic, and two further lower latitude centers of opposite sign associated with the Aleutian Low and the Azores High. Overall, this pattern is similar to that calculated from reanalysis data (see Chapter 1.2.3.2—Large-scale Atmospheric Variability), although there it represents more than 50% of the total variability. The model results presented here have a smaller amplitude, which is explained by the reduced variability in the ensemble mean, that has been created by averaging 10 members. The center close to the Aleutian Low is situated somewhat too south in the model results. The pattern, and the percent of the total variability it describes is very similar in each individual member of the ensemble (not shown).
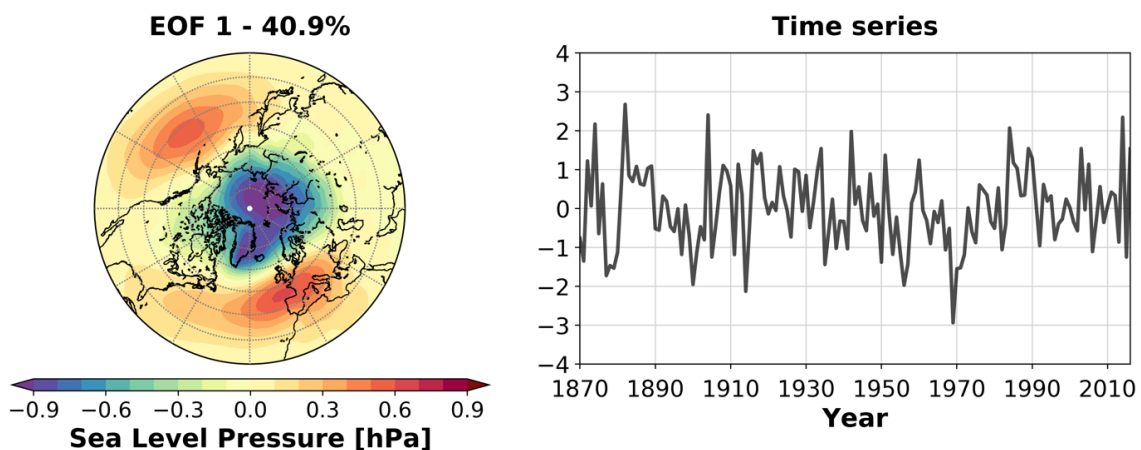

Figure 4.5. *Arctic Oscillation (AO) for winter (November–April) in MPI-ESM simulations as the (left) eigen vector and (right) principal component time series of the first empirical orthogonal function (EOF) of Northern Hemispheric (north of 20°N) sea-level pressure from the ensemble mean of 10 fully coupled control runs for the period 1870–2016.*

A powerful diagnostic for identifying links between changes in the AO strength and freshwater content anomalies is provided by associated patterns on Figure 4.6. Solid lines

in each panel depict linear fits to the data points, and their slope represents the temporal correlation between the detrended freshwater content and AO time series. All data are based on the ensemble mean of 10 fully coupled control simulations for the time period 1870–2016.

According to the top left panel of Figure 4.6, the annual means of Arctic total freshwater content are very weakly linked to time series of the AO index. Their temporal correlation is low (r=-0.20), and the data points are scattered. Splitting the total freshwater content into a liquid (top middle panel) and solid (top right panel) component does not improve the results. The temporal correlation between the AO index and the liquid (top middle panel, r=-0.11) and the solid (top right panel, r=-0.18) content is similarly low, implying no link between their time series in the ensemble mean.
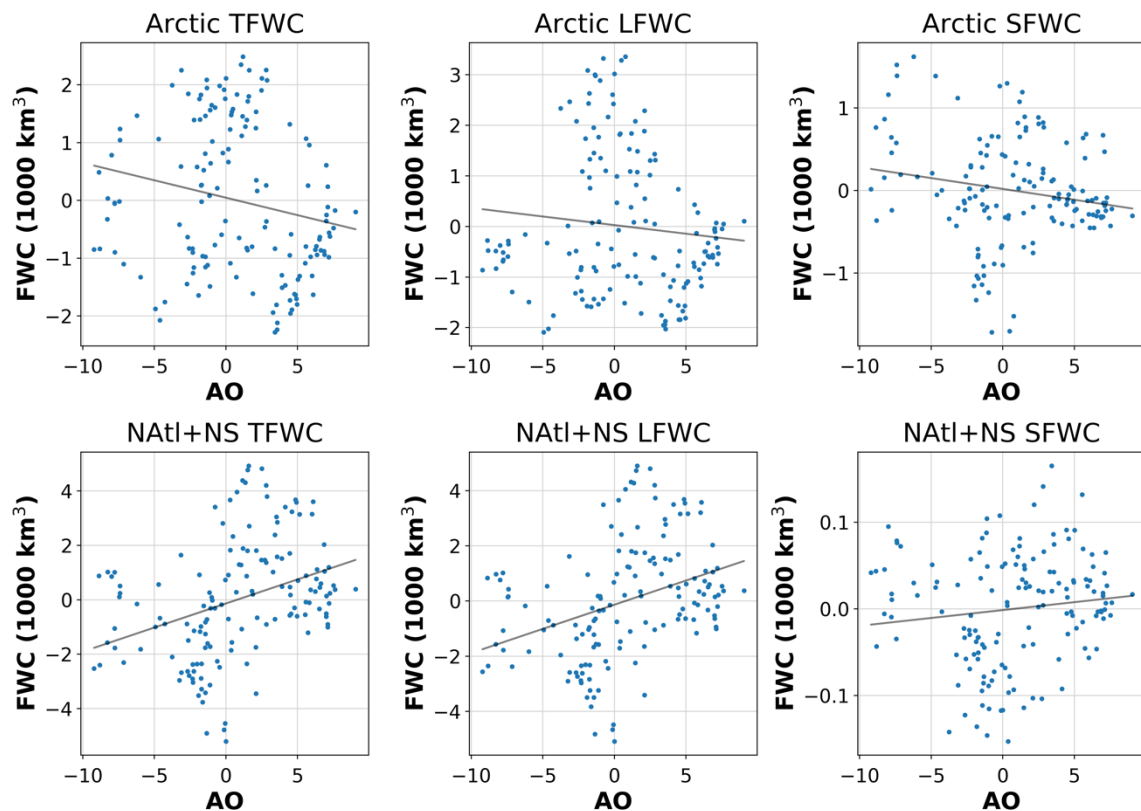

Figure 4.6. *Scatter plots of AO vs. freshwater content time series in MPI-ESM simulations from the ensemble mean of 10 fully coupled control runs for the period 1870–2016. left - total content, middle - liquid content; right - solid content in (top) the Arctic Ocean and in (bottom) the Subarctic North Atlantic. The solid lines depict linear fits to the data points.*

The bottom panels of Figure 4.6 show the connection between the simulated AO and the Subarctic North Atlantic freshwater content. In case of the total content (bottom left panel), their moderate correlation (r=0.35) suggests a potential link between their time series, but it is not particularly robust over the full simulation period. Since in the Subarctic North Atlantic the contribution of the liquid freshwater to the total content is two orders

of magnitude larger than the contribution of the solid component, the results are almost the same for the liquid part (bottom middle panel, r=0.35), and show no connection for the solid part (bottom right panel, r=0.12).

The same analysis was repeated for the NAO as well. The simulated pattern and time series of the NAO are plotted on Figure 4.7 as the leading EOF of sea-level pressure in the North Atlantic region (20°N–70°N, 90°W–40°E) and its principal coefficients. The NAO pattern on the left panel describes 41.6% of the total sea-level pressure variability in the region, and is characterized by two centers of action of opposite sign. One in the northern edge of the region east of Greenland, and one in the south, off the Iberian coast. These correspond to the Icelandic Low and the Azores High, also similarly present in the NCEPcfsr reanalysis data (see Chapter 1.2.3.2–Large-scale Atmospheric Variability), with the Icelandic Low shifted somewhat to the west in MPI-ESM. In the reanalysis this pattern represents a larger part of the total North Atlantic sea-level pressure variability (almost 50%), but overall the simulated NAO is very similar to the observed one. Moreover, both the pattern and the percent of the total variability it describes is very similar in each individual member of the ensemble (not shown).
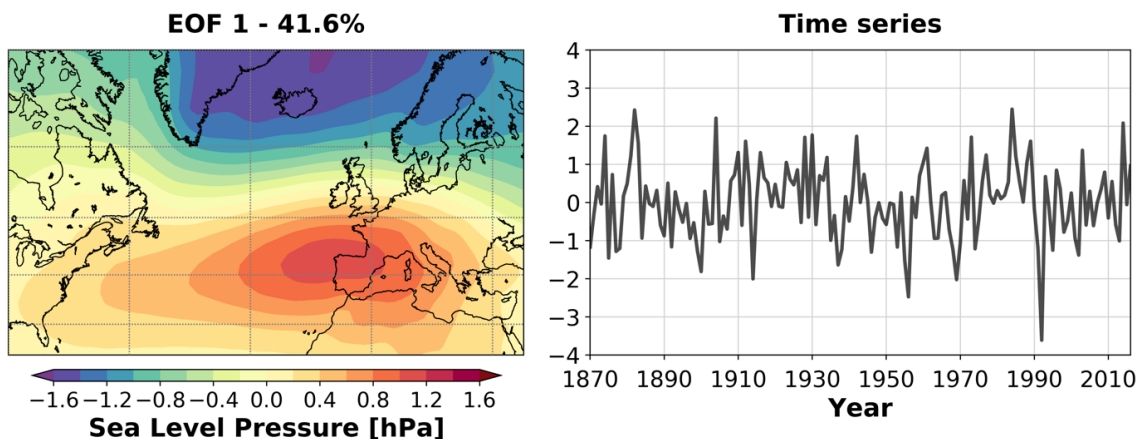

Figure 4.7. *North Atlantic Oscillation (NAO) for winter (December–February) in MPI-ESM simulations as the (left) eigen vector and (right) principal component time series of the first empirical orthogonal function (EOF) of North Atlantic sea-level pressure from the ensemble mean of 10 fully coupled control runs for the period 1870–2016.*

The links between the NAO and the different freshwater contents is presented by correlation plots on Figure 4.8 in the same way as for the AO above. According to the top left panel of Figure 4.8, there is some negative temporal correlation (r=-0.38) between the simulated time series of the NAO index and the total freshwater content in the Arctic Ocean. The correlation is also negative, but weaker for both the liquid (top middle panel, r=-0.25) and the solid component (top right panel, r=-0.23). The results show almost no connection between the NAO and the Subarctic North Atlantic freshwater content (bottom

panels of Figure 4.8). The temporal correlations are very low for the total content, and for the different components as well (r<0.1 for all cases).
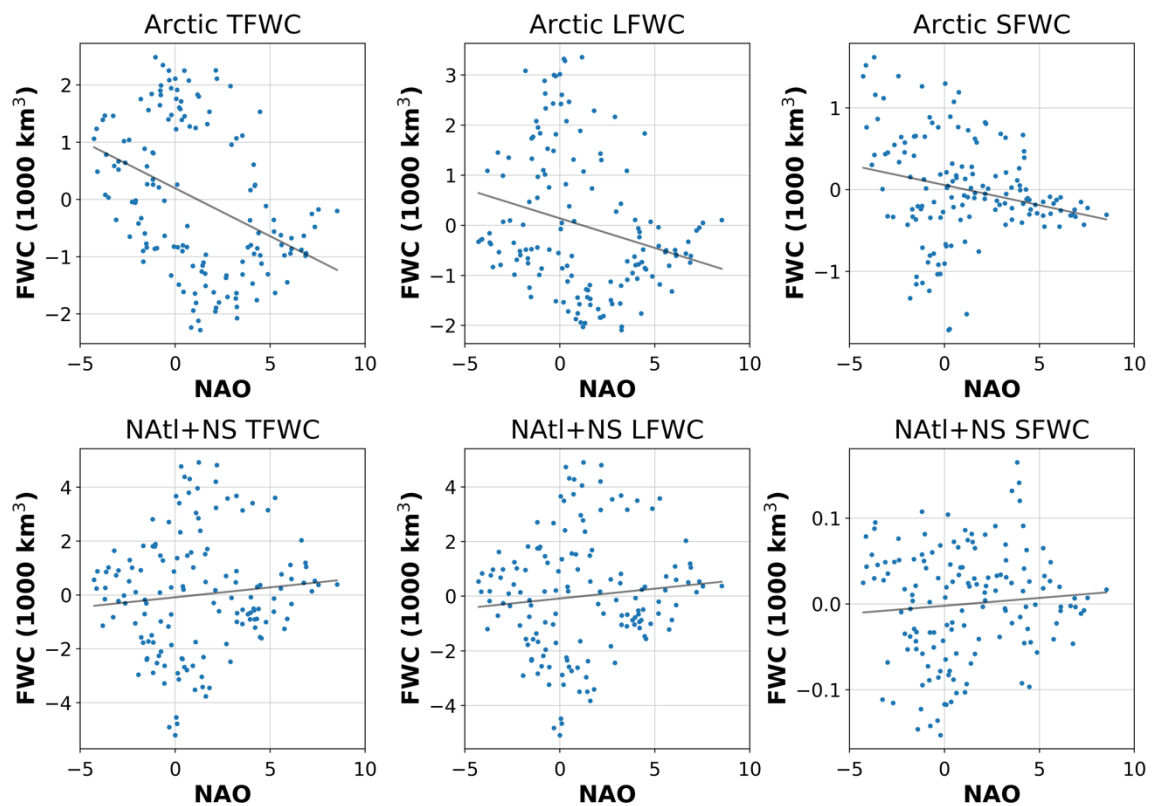

Figure 4.8. Scatter plots of NAO vs. freshwater content time series in MPI-ESM simulations from the ensemble mean of 10 fully coupled control runs for the period 1870–2016. left - total content; middle - liquid content; right - solid content in (top) the Arctic Ocean and in (bottom) the Subarctic North Atlantic. The solid lines depict linear fits to the data points.

These results based on the ensemble mean for 1870–2016 suggest that anomalies in Arctic freshwater content are more related to changes of the NAO rather than of the AO. In the Subarctic North Atlantic, it is the opposite: the freshwater content there shows no link with the NAO, but there is some correlation with the AO. However, it should be noted that although none of the panels on Figure 4.6 or Figure 4.8 show a robust link in the full time period in the ensemble mean, the same correlation plots show fundamentally different results for arbitrarily selected subperiods of individual members of the ensemble. Both in case of the AO and the NAO, their time series can show a significant correlation or anticorrelation, or no correlation for different multidecadal periods of the members (not shown).

There is observational evidence pointing towards the important role of other modes of atmospheric variability that are not or only partly represented by the AO or the NAO. For example the alternating cyclonic and anticyclonic circulation regimes of the Arctic atmosphere (Proshutinsky and Johnson, 1997), represented by the Arctic Ocean Oscillation index (Proshutinsky et al., 1999), have a stronger influence on Arctic liquid

freshwater anomalies than the hemispheric changes described by the AO (Rabe et al., 2014). Variations in Arctic sea ice motion and export have been linked to a local atmospheric dipole anomaly, that corresponds to the second-leading EOF of winter sea-level pressure north of 70°N. Although this mode describes only 13% of the total regional variance in sea-level pressure, its influence on sea ice motion and export is greater than that of the AO (Wu et al., 2006). A model study of Ionita et al. (2016) showed that Arctic sea ice accumulation and export is also modulated by an atmospheric blocking activity over Greenland. This activity is strongly linked to the NAO (Davini et al., 2012), but better represents a key driver of changes in the solid component of freshwater.

A recent model study of Johnson et al. (2018) investigated the response of Arctic liquid freshwater content to a step change in the strength of the first three EOF modes of sea-level pressure north of 70°N. They found the strongest response to the third mode, even though it described much less of the total sea-level pressure variance than the first two modes. They also reconstructed the modeled freshwater content variability from the principal component time series of the EOF modes of sea-level pressure, and got the best results when all three modes were included.

When attempting to estimate the role of sea-level pressure variability in driving freshwater anomalies, different atmospheric drivers should be considered, not just those described by for example the NAO (Ionita et al., 2016). Taking into account multiple modes of atmospheric variability yields better results (Johnson et al., 2018), but this approach still has limitations. For example, while it allows a reconstruction of freshwater content time series, it cannot identify specific modes of freshwater variability that correspond to the different modes of atmospheric variability. Moreover, the EOFs are selected by maximizing the variance they describe—the variance in the sea-level pressure field, not in freshwater content. As Johnson et al. (2018) noted, while the EOFs are independent by construction, their impact on freshwater content may not be. These limitations were addressed in this study by performing a comprehensive analysis of sea-level pressure and freshwater content.

4.2.2. A Comprehensive Analysis of Atmospheric Variability and Freshwater Anomalies

The EOF analysis is a powerful tool to identify dominant patterns in sea-level pressure; however, these patterns represent the major statistical modes of its variability, and they do not necessarily correspond to those modes of sea-level pressure variability that are best connected to changes in freshwater content. In order to identify such modes, the freshwater variability should also be taken into account. This was achieved by performing a Redundancy Analysis, a method that is able to identify pairs of patterns in sea-level

pressure (the predictor) and in freshwater content (the predictand) that are strongly linked through a regression model, while maximizing the freshwater variance. The results of the analysis are presented here separately for the liquid and solid freshwater component, due to their likely different atmospheric drivers. A basic introduction to the Redundancy Analysis (RDA) is provided in the Appendix at the end of this thesis.

The RDA modes are illustrated as maps in two rows, where the top row shows the predictor mode, and the bottom row shows the predictand mode (Figure 4.9 and Figure 4.10). Redundant pairs are thus presented in one column; correlation coefficients between their time series are given in the text and are shown in more detail in Table 4. The analysis was based on a concatenated time series of all 10 members of the ensemble, linking their detrended 1870–2016 time series together to create a long time series. This way it could be ensured that the results would be robust across the ensemble, regardless of the differences in the freshwater variability in different members.
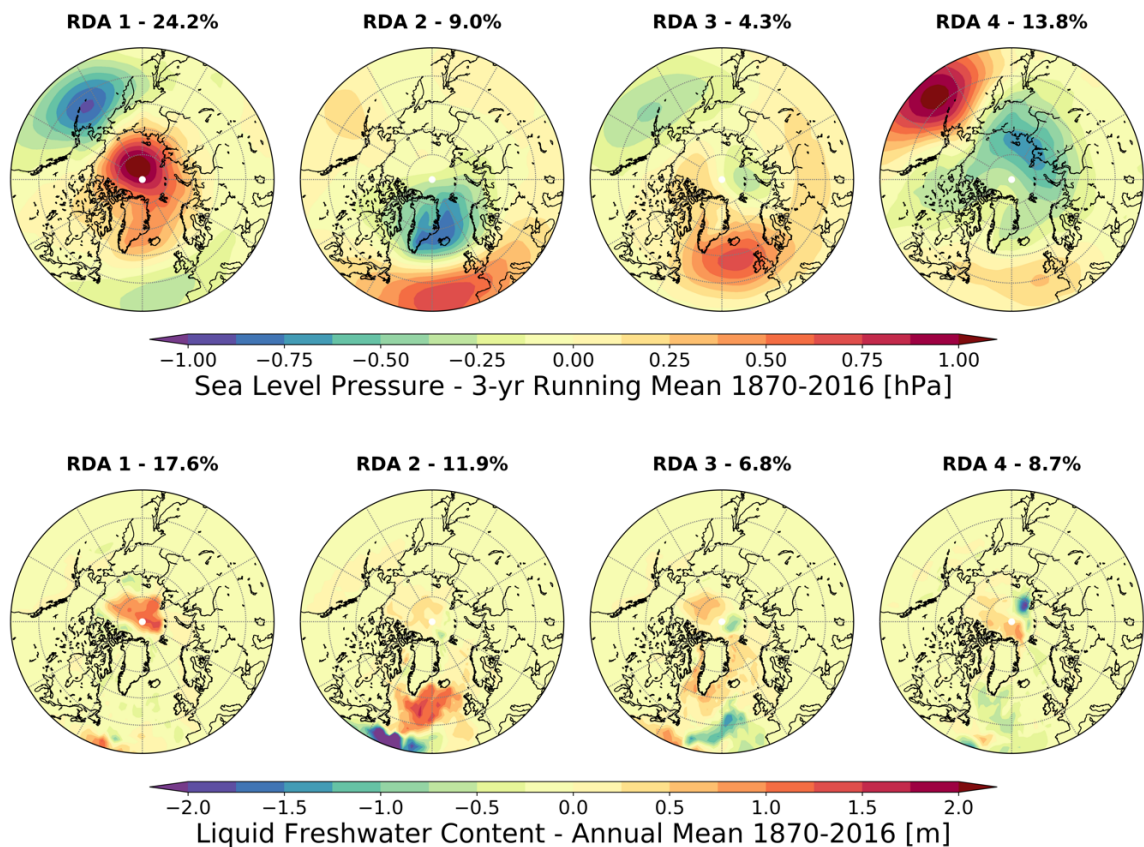

Figure 4.9. The first four redundant modes of sea-level pressure (north of 20°N) and liquid freshwater content (Arctic and Subarctic North Atlantic north of 35°N) variability based on concatenated time series of 10 fully coupled control runs for the period 1870–2016. The top row shows predictor (three-year running mean of sea-level pressure) modes, the bottom row shows predictand (annual means of liquid freshwater content) modes north of 40°N. The numbers above the maps stand for the percent of total variance described by the mode.

Figure 4.9 shows the first four RDA modes of sea-level pressure and liquid freshwater content. In this analysis the predictor was the three-year running mean of sea-level pressure, and the predictand was the annual means of liquid freshwater content. A three-year running mean was chosen for the sea-level pressure because of its higher frequency variability compared to that of the freshwater content.

The first RDA mode (Figure 4.9, first column) shows an anomaly of freshwater content (the predictand) in the central Arctic Basin, largely corresponding to the Beaufort Gyre in the model. There is a weak anomaly of opposite sign along the continental shelves in the Arctic. At lower latitudes, in the Nordic Seas and the Subpolar North Atlantic, no anomaly is present. This mode describes 17.6% of the predictand variance. The predictor mode shows a tripole pattern that is similar to the AO at the first look, with a sea-level pressure anomaly in the Arctic, and two other centers of opposite sign located near the Aleutian Low and the Azores High. However, the Arctic pressure anomaly is situated over the central Arctic, unlike for the AO, and this mode describes only 24.2% of the total predictor variance. The correlation coefficient between the predictor and predictand time series is 0.72.

The second RDA mode (Figure 4.9, second column) is characterized by a strong freshwater anomaly in the Subpolar North Atlantic Ocean, with a strong anomaly of opposite sign further south around 40°N. This mode represents 11.9% of the predictand variance. The corresponding predictor pattern exhibits a pressure dipole between two centers that are located near the Icelandic Low and the Azores High, reminiscent of the NAO, but describing only 9% of the predictor variance. The correlation coefficient of the predictor and predictand time series is 0.62.

Further modes are less distinct. The third RDA mode (Figure 4.9, third column) is characterized by a predictand pattern describing 6.8% of its variance, with a weak freshwater dipole in the Arctic, and a slightly higher freshwater content in the Nordic Seas and around Greenland, and lower values in the North Atlantic around 50°N. The corresponding predictor pattern (with a correlation coefficient of 0.52) is dominated by a positive pressure field south of Iceland, and a weak pressure dipole in the Arctic between the Beaufort High and a low pressure center north of Novaya Zemlya. This pattern represents 4.3% of the predictor variance. The fourth mode (Figure 4.9, fourth column) exhibits a weak sign in the predictand, except for a small region in the northern Laptev Sea, and represents 8.7% of the total freshwater variance. Its correlation with the predictor series is 0.39, and the corresponding sea-level pressure pattern is similar to the first mode, although somewhat weaker, and the three centers of anomalies are also somewhat displaced. The next three modes (not shown) describe an additional 16% of the predictand, and 9.4% of the predictor variance.

The solid component of freshwater content (stored in sea ice) shows different patterns of variability, and is driven by different modes of atmospheric variability. Figure 4.10 presents the first four RDA modes of annual sea-level pressure and solid freshwater content.

The predictand pattern of the first RDA mode (Figure 4.10, first column) is characterized by a seesaw between the Siberian Arctic and the Canadian Arctic extended east to Svalbard. This pattern describes 19.5% of the predictand variance. The corresponding atmospheric mode is dominated by a sea-level pressure anomaly centered over the northern Kara and Laptev seas, describing 15.6% of the total predictor variance. The correlation coefficient between the two time series is 0.77.
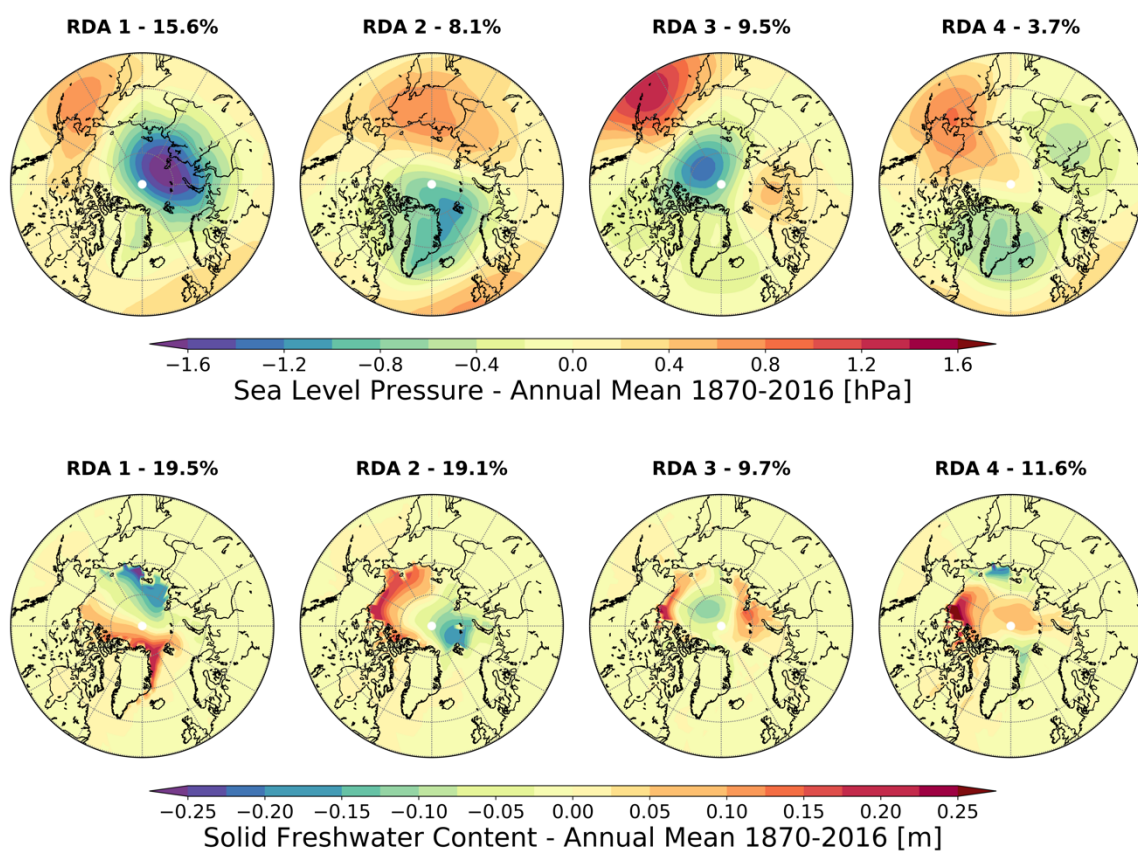

RDA 1 - 15.6%   **RDA 2 - 8.1%**   **RDA 3 - 9.5%**   **RDA 4 - 3.7%**

Sea Level Pressure - Annual Mean 1870-2016 [hPa]

RDA 1 - 19.5%   **RDA 2 - 19.1%**   **RDA 3 - 9.7%**   **RDA 4 - 11.6%**

Solid Freshwater Content - Annual Mean 1870-2016 [m]

Figure 4.10. *The first four redundant modes of sea-level pressure (north of 20°N) and solid freshwater content (stored in sea ice, north of 20°N) variability based on concatenated time series of 10 fully coupled control runs for the period 1870–2016. The top row shows predictor (annual mean of sea-level pressure) modes, the bottom row shows predictand (annual means of solid freshwater content) modes north of 50°N. The numbers above the maps stand for the percent of total variance described by the mode.*

The second RDA mode (Figure 4.10, second column) is similar to the first, with a 90 degree rotation. It depicts a seesaw pattern between two sides of the Lomonosov Ridge, describing a similar portion of the total predictand variance, 19.1%. In the atmosphere, this mode is characterized by a sea-level pressure anomaly centered over the northern

Greenland Sea around Fram Strait, with two further centers of opposite sign, one over eastern Siberia, the other west of the British Isles at about 50°N. This mode describes 8.1% of the predictor variance. The correlation coefficient between the two time series is 0.67.

The third mode (Figure 4.10, third column) shows a predictand anomaly around the Central Arctic, with anomalies of opposing sign along the Canadian and the Siberian shelf seas. This mode describes 9.7% of the total variance of solid freshwater content. It is tightly linked (with a time correlation of 0.72) to a corresponding atmospheric mode of a pressure anomaly centered over the same location in the Amerasian Basin. In the predictor mode there is also a strong opposing anomaly around the Aleutian Low, creating a pattern that resembles the AO, although it describes only 9.5% of the total sea-level pressure variance.

The fourth mode (Figure 4.10, fourth column) shows a strong freshwater anomaly along the Canadian shelf, and anomalies of opposing sign in the East Siberian Sea and east of Greenland, describing 11.6% of the total predictand variance. The corresponding mode in the atmosphere is characterized by three centers of (rather weak) sea-level pressure anomalies, one over Bering Strait, and two of opposing sign over Greenland and Siberia. This mode describes 3.7% of the predictor variance, and its time series are correlated with the predictand series with a coefficient of 0.58. The next three modes (not shown) describe an additional 22% of the predictand, and 13% of the predictor variance.

	CTRL	CTRL_00	CTRL_01	CTRL_02	CTRL_03	CTRL_04	CTRL_05	CTRL_06	CTRL_07	CTRL_08	CTRL_09
RDA 1	**0.72**	0.77	0.80	0.60	0.73	0.76	0.70	0.61	0.67	0.74	0.78
RDA 2	**0.62**	0.65	0.63	0.55	0.67	0.67	0.51	0.71	0.68	0.62	0.45
RDA 3	**0.52**	0.67	0.43	0.53	0.55	0.47	0.56	0.44	0.56	0.52	0.48
RDA 4	**0.39**	0.50	0.48	0.39	0.35	0.27	0.28	0.32	0.50	0.38	0.46

	CTRL	CTRL_00	CTRL_01	CTRL_02	CTRL_03	CTRL_04	CTRL_05	CTRL_06	CTRL_07	CTRL_08	CTRL_09
RDA 1	**0.77**	0.79	0.73	0.78	0.76	0.78	0.75	0.81	0.78	0.77	0.75
RDA 2	**0.67**	0.63	0.65	0.66	0.64	0.66	0.63	0.72	0.71	0.74	0.68
RDA 3	**0.72**	0.73	0.75	0.71	0.68	0.75	0.72	0.75	0.75	0.69	0.68
RDA 4	**0.58**	0.65	0.54	0.67	0.62	0.56	0.49	0.56	0.54	0.62	0.55

Table 4. Correlation coefficients of predictor and predictand time series of the first four redundancy modes in the full concatenated run ('CTRL', in bold) and in each individual member of the ensemble ('CTRL_00–09'). Top: predictor is three-year running mean of sea-level pressure, predictand is annual means of liquid freshwater content (see modes on Figure 4.9); Bottom: predictor is annual means of sea-level pressure, predictand is annual means of solid freshwater content (see modes on Figure 4.10).

The above patterns were identified in the concatenated time series. Therefore, although the first four modes presented here describe only 45% of the total liquid and 60% of the solid freshwater variance, they represent part of the variability, which is robust in

all members of the ensemble. The same can be stated about the connection of these patterns to the respective atmospheric patterns of the redundancy modes. According to Table 4, the correlation coefficients of the time series of the predictor and predictand modes are also rather similar in the concatenated series (labeled CTRL), and in individual members of the ensemble (CTRL_01–09).

As the correlation coefficients of the redundancy modes are similar for all members of the ensemble, their time series are shown here through an example from an arbitrarily chosen member. This reduces their length to 147 time steps opposed to the 1470 time steps of the full concatenated series, and thus they are easier to visualize. Here the predictor and predictand time series are shown corresponding to the first four redundancy modes presented above, for the member 'CTRL_03'.
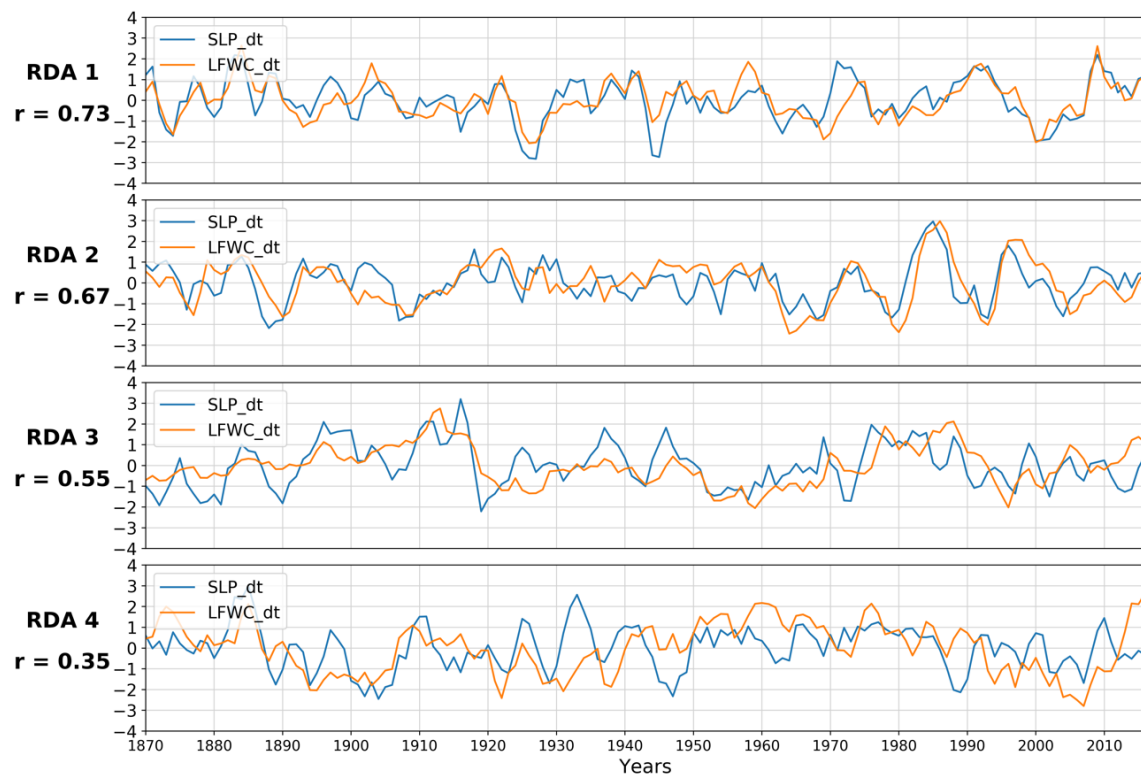

Figure 4.11. Time series of the first four redundant modes of sea-level pressure (blue lines) and liquid freshwater content (orange lines) variability in the fully coupled member 'CTRL_03' based on concatenated time series of 10 fully coupled control runs for the period 1870–2016. The modes and the percent of total variance they describe are shown on Figure 4.9.

Figure 4.11 depicts the time series of the first four redundancy modes of sea-level pressure and liquid freshwater content shown on Figure 4.9. The high temporal correlation of the leading two modes is clearly visible, with the time series of sea-level pressure and liquid freshwater content showing mostly synchronized large, multi-year anomalies. The correlation is considerably lower for the third and fourth mode. The lower frequency variability of freshwater content in comparison with sea-level pressure is also

apparent, the time series of the latter having been based on a three-year running mean instead of annual values.

The time series corresponding to the redundancy modes of sea-level pressure and solid freshwater content (see Figure 4.10) are shown on Figure 4.12. The predictand series closely follow the predictor series in all modes, in particular the first mode. Autocorrelation is much less prominent compared to the redundancy series for the liquid freshwater content, suggesting a higher frequency variability of the solid component (sea ice), as well as part of the atmospheric variability driving it as predictor.
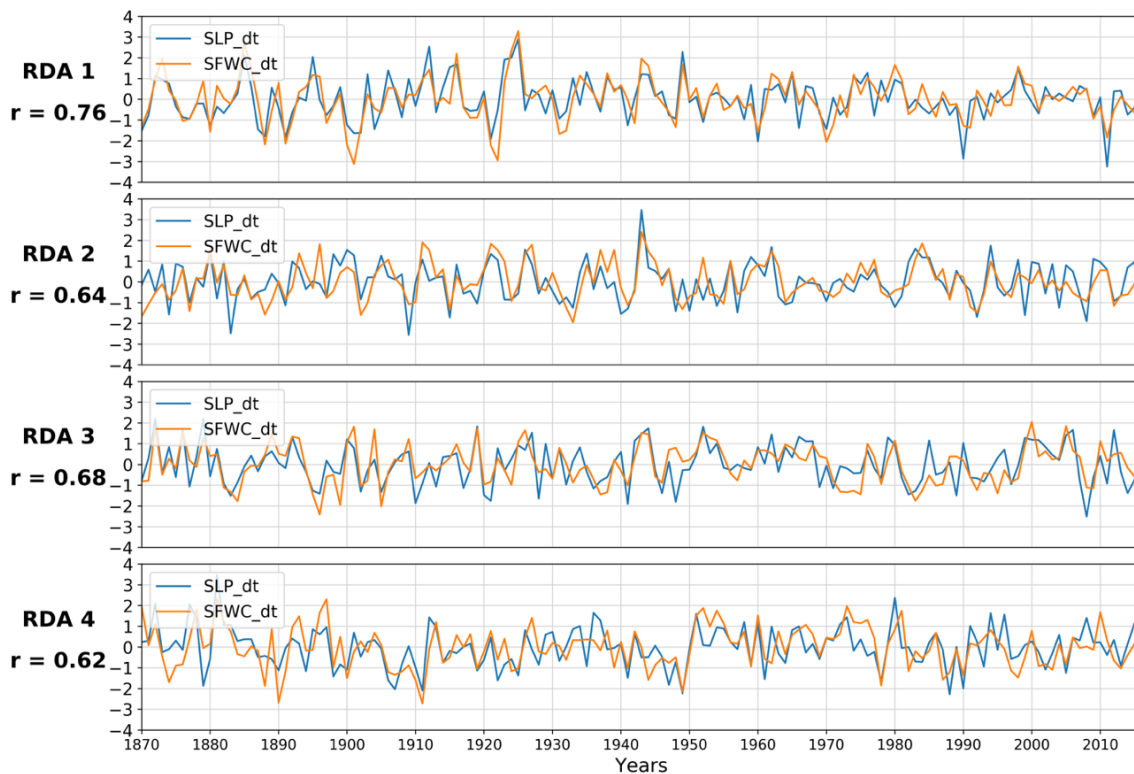

Figure 4.12. *Time series of the first four redundant modes of sea-level pressure (blue lines) and solid freshwater content (orange lines) variability in the fully coupled member 'CTRL_03' based on concatenated time series of 10 fully coupled control runs for the period 1870–2016. The modes and the percent of total variance they describe are shown on Figure 4.10.*

4.3.   Model Runs with Constrained Wind Forcing Based on Observations

The results of the statistical analysis presented above suggest a close connection between certain modes of atmospheric variability and freshwater content. It is likely that the driving force of the freshwater anomalies is associated with these sea-level pressure patterns. However, the hypothesis of this study was that this driving force is the wind

stress. Therefore, as an attempt to isolate the effect of the wind forcing, parts of the model experiments were rerun with prescribed wind forcing, while otherwise keeping the restart conditions and the model setup (including the rest of the coupling) identical to the fully coupled control runs. For details of the model structure and the experiment setup see Chapters 2.2 and 2.3.

Here results are shown from these partially coupled runs that used prescribed wind stress forcing according to observations (based on wind data from NCEPcfsr). It is shown that the freshwater simulations in these experiments are closer to observations both in terms of mean values and of the size and timing of anomalies.

4.3.1. Freshwater Content and Fluxes

The Modini-MPI-ESM simulated mean liquid freshwater content for the period of 1980–2010, integrated from the surface down to $S_{ref} = 34.8$ is shown on Figure 4.13, together with the observed values. The simulated liquid freshwater content totals up to a layer of 10 to 17 meters in most of the deep Arctic, similarly to observations. There is significantly less freshwater in the Eurasian Basin, and essentially no freshwater in the Subpolar North Atlantic and in the Nordic Seas, apart from the vicinity of the eastern boundary currents, also similar to the observed patterns. However, the partially coupled runs with NCEPcfsr wind anomaly forcing show too high freshwater content along the Siberian shelf, especially in the Laptev Sea, where the bias reaches 10 meters.
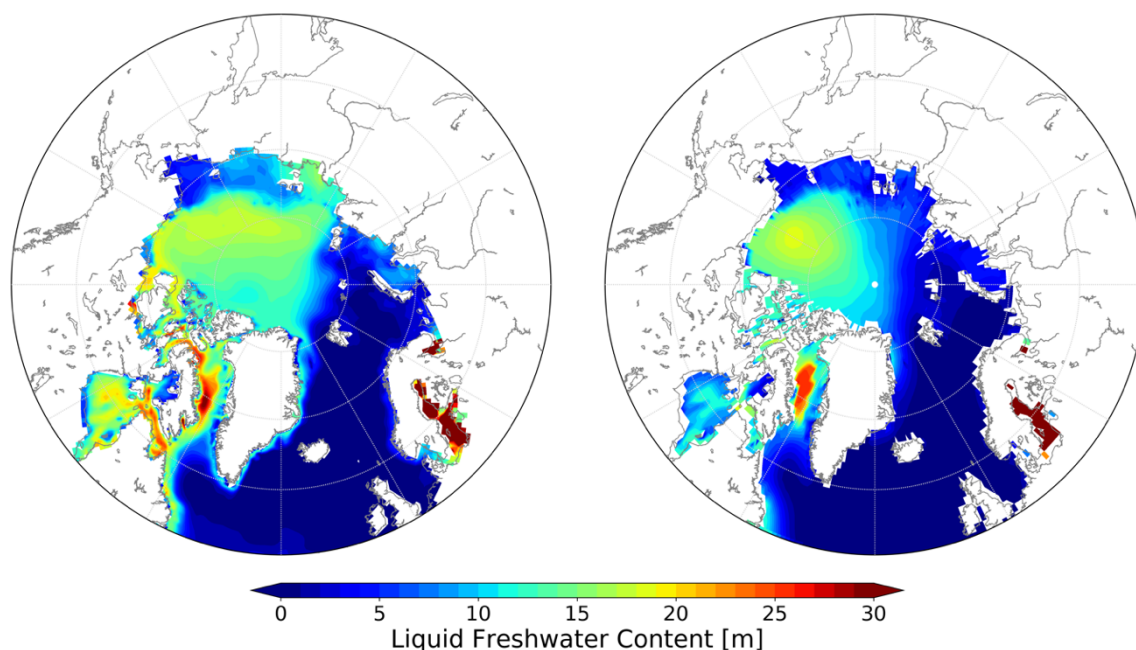

Figure 4.13. Liquid freshwater content (S$_{ref}$ = 34.8, integrated from surface down to the depth of S$_{ref}$). From (left) partially coupled Modini-MPI-ESM simulations with wind anomaly forcing from NCEPcfsr as ensemble mean of 10 fully coupled control runs for the period 1980–2010 and from (right) PHC3.0 climatology (Steele et al., 2001).

The freshwater reservoir of the Beaufort Gyre in the Canada Basin is less pronounced than in observations. The high freshwater content also reaches too far in the Eurasian Basin, with a clear overestimation as far as the Nansen Basin. Compared to observations, the model also simulates too high content along the eastern boundary currents at lower latitudes. These biases are generally very similar to those seen in the fully coupled, unconstrained model configuration (see Figure 3.8). A notable difference is the absence of the overestimation in the Canada Basin, especially in the Beaufort Gyre, where it is up to 3 meters less than in the fully coupled runs. The freshwater content in the shelf regions and along the eastern boundary currents are slightly higher (by 1-2 meters) than in the fully coupled runs.

The time series of liquid freshwater content, integrated in the total volume of the Arctic Ocean and in the Subarctic North Atlantic are shown on Figure 4.14 as annual values for the period of 1979–2016. Values in the Arctic Ocean are between 63–70,000 km³, with no significant trend. There is a large, multi-year negative anomaly of 5,000 km³, reaching the minimum in 1995-1996. The standard deviation between the 10 members of the ensemble is about 3–5,000 km³. In the Subarctic North Atlantic, annual values range from -109,000 km³ to -90,000 km³, with a minimum in 1982, and a maximum in 1995-1996. The peak of this multi-year positive anomaly corresponds that of the negative anomaly in the Arctic Ocean, but it is roughly double in size. The time series show a positive trend, and an ensemble standard deviation of 5–7,000 km³. Compared to the time series from fully coupled model runs (see Figure 3.9), a notable difference is the amplitude of anomalies. In both domains, the anomalies are much larger here than in the fully coupled time series, while the ensemble standard deviations are similar.
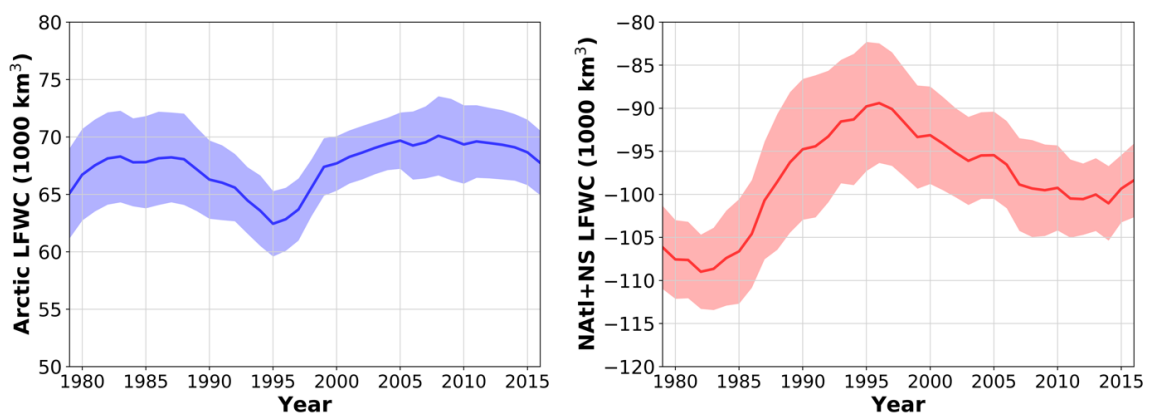

Figure 4.14. *Time series of annual liquid freshwater content (Sref = 34.8, integrated in full vertical column) from partially coupled MPI-ESM simulations with wind anomaly forcing from NCEPcfsr (left) in the Arctic Ocean, and (right) in the Subarctic North Atlantic. Solid line indicates the mean, shaded area indicates the standard deviation of 10 ensemble members.*

The time means of net freshwater fluxes across sections bordering the Arctic Ocean (liquid and solid component separately) in the partially coupled Modini-MPI-ESM simulations are presented in Table 5. For comparison, values from fully coupled model results are summarized in Table 3. Observed values referred here are taken from Haine et al. (2015). Positive values denote fluxes into the Arctic Ocean, negative values show an export of freshwater to lower latitudes. Compared to the fully coupled results, the model simulations with NCEPcfsr wind anomaly forcing show an increased liquid freshwater flux through Bering Strait of 2460 km^3 for the period of 1980–2010, very close to observations (2430 km^3). The solid flux increases somewhat (from 4.5 to 29 km^3), but is still much smaller than in observations (140 km^3). Freshwater fluxes through the Canadian Arctic Archipelago and across Davis Strait are smaller than in the fully coupled runs, and slightly underestimate the observed liquid component (-3100 km^3), and overestimate the solid component (-210 km^3) across Davis Strait. The mean liquid freshwater flux across Fram Strait is considerably higher than in the fully coupled runs (-3430 km^3 instead of -2910 km^3), overestimating the observed values (-2600 km^3). The solid component is also higher (-1960 km^3 instead of -1700 km^3), but it is still smaller than observed (-2170 km^3). Finally, the liquid flux through the Barents Sea Opening is somewhat smaller than in the fully coupled runs (-470 km^3 instead of -660 km^3), while the solid flux is larger (-138 km^3 instead of -72 km^3). Together, they are significantly larger than observed (-90 km^3).

Section	Net liquid FW flux [km^3]	Net solid FW flux [km^3]
Bering Strait	2460 $\pm$ 90	29 $\pm$ 8
Canadian Archipelago	-2720 $\pm$ 160	-380 $\pm$ 22
Davis Strait	-2920 $\pm$ 160	-680 $\pm$ 27
Fram Strait	-3430 $\pm$ 170	-1960 $\pm$ 47
Barents Sea Opening	-470 $\pm$ 60	-138 $\pm$ 34

Table 5. *Net freshwater fluxes across sections bordering the Artic and the Subpolar North Atlantic Oceans from partially coupled Modini-MPI-ESM simulations with wind anomaly forcing from NCEPcfsr for the period 1980–2010. Values are based on the mean, the uncertainties on the standard deviation of 10 ensemble members. Negative values indicate southward transport.*

The time series of annual net freshwater fluxes across the above sections are shown on Figure 4.15. Due to the relatively short time period and the large interannual variability, no clear trend is visible, except for the growing liquid freshwater export through Fram Strait and the Barents Sea Opening. The ensemble variability is significantly smaller for the solid component in all sections, even where their mean values are large, for example in Fram Strait. This is due to the differences in the complexity of the driving forces of different components. The members of the Modini-MPI-ESM ensemble have different oceanic states within the range of their internal variability, but the anomalies in their wind stress forcing are the same. Solid freshwater flux (sea ice transport) is largely driven by

the wind, which explains its small differences across the ensemble. However, liquid freshwater is transported in the entire water column, and is thus influenced by other processes as well in addition to wind stress forcing.
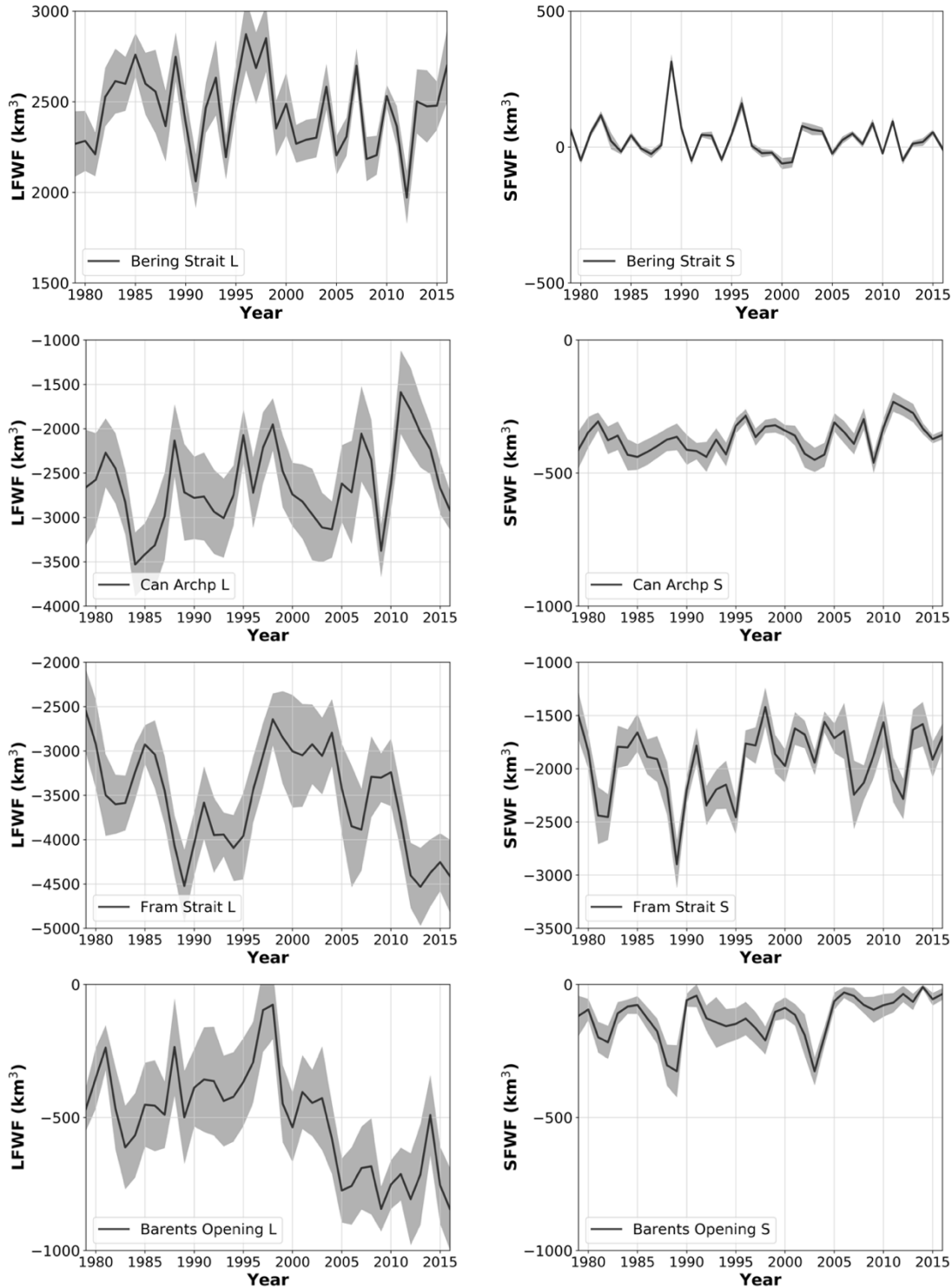

Figure 4.15. *Time series of annual net freshwater (left: liquid; right: solid) fluxes across sections from partially coupled Modini-MPI-ESM simulations with wind anomaly forcing from NCEPcfsr. Solid line indicates the mean, shaded area indicates the standard deviation of 10 ensemble members. Negative values indicate southward transport.*

Comparing these results with those from the fully coupled configuration (see Figure 3.10), the effect of the prescribed wind data is evident. The ensemble variability is reduced, especially for the solid fluxes, confirming their higher sensitivity to atmospheric momentum forcing, whose prescribed anomalies are the same in all members. For the same reason, the interannual variability is also much larger in all sections for both components. Individual members actually show similar amplitudes in the unconstrained fully coupled runs, but they are greatly reduced by the ensemble mean creation, that masks the size of temporal anomalies.

Changes in the above lateral freshwater fluxes are the main drivers of freshwater content variability both in the Arctic Ocean and in the Subarctic North Atlantic, similarly to the findings based on fully coupled simulations. According to Figure 4.16, there is a very close connection between their detrended total freshwater contents and the sum of the cumulative lateral fluxes across sections bordering their domains. Time series of the content (colored line) and the fluxes (black line) follow closely for both regions, and their ensemble variabilities are also very similar in size. The correlation coefficient is 0.93 for the Arctic Ocean, and 0.99 for the Subarctic North Atlantic. Both are highly significant (with above 99% confidence), and higher than for the fully coupled model runs (0.92 and 0.76 respectively, see Figure 3.11).
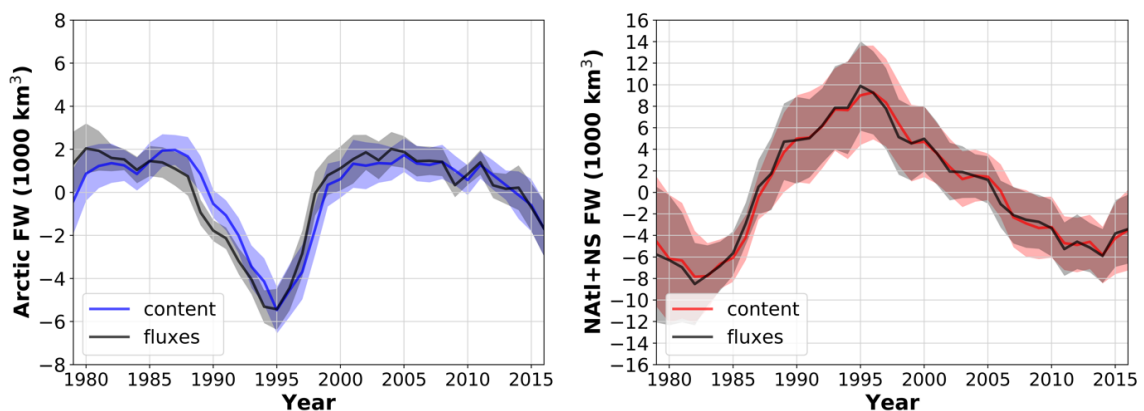

Figure 4.16. *Time series of detrended annual total freshwater content in the domain of, and cumulative total freshwater fluxes across sections around the Arctic Ocean (left), and the Subarctic North Atlantic (right) from partially coupled Modini-MPI-ESM simulations with wind anomaly forcing from NCEPcfsr. Solid line indicates the mean, shaded area indicates the standard deviation of 10 ensemble members.*

Finally, the Arctic and Subarctic North Atlantic freshwater covariability is assessed. Figure 4.17 depicts the times series of their detrended total freshwater contents from partially coupled Modini-MPI-ESM simulations, and also from fully coupled runs for the same time period (1979–2016) for comparison. The unconstrained fully coupled runs on the left panel of Figure 4.17 show no clear connection, with a weak positive correlation ($r = 0.46$). The ensemble mean shows smaller anomalies than the range of ensemble

standard deviations for both domains, therefore no robust conclusion can be drawn from it. Individual members of the fully coupled ensemble show changes with larger amplitudes that are sometimes synchronized in the two domains (see their longer time series on Figure 3.16), but their connection still cannot be objectively evaluated due to large differences between the members (correlation coefficients in the 10 members for 1979–2016 range from -0.36 to +0.65).

The partially coupled runs on the right panel of Figure 4.17 show different results. Although the ocean state varies within its internal variability in different members of the ensemble, the Modini-MPI-ESM runs with prescribed wind anomaly forcing show similar changes in freshwater content. Because of this, their ensemble mean plotted here shows much larger anomalies than for the unconstrained fully coupled ensemble. The ensemble variability is reduced, especially for the Arctic Ocean. The simulations show no significant change in Arctic freshwater content until the late 1980s, when a decrease begins that reaches -7,000 km^3 by 1995. Afterwards the freshwater content recovers in five years, and stays high again until the early 2010s when a slow reduction begins again. In the Subarctic North Atlantic, the simulations show a strong increase of about 10,000 km^3 between 1985 and 1990, when the Arctic content does not change. However, the changes in the two domains are of similar size and timing during the period 1990–2005. After 2005, the decrease of freshwater content continues in the Subarctic North Atlantic until 2014.
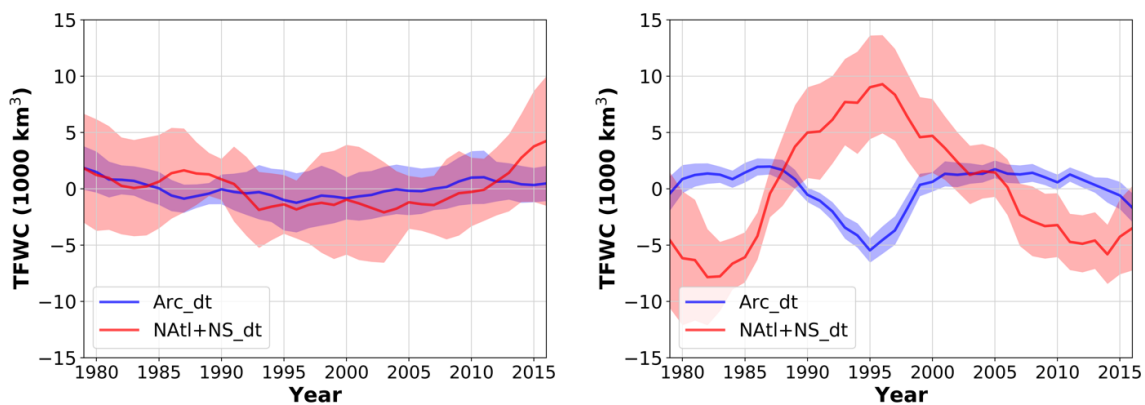

Figure 4.17. *Time series of detrended annual total (liquid and solid) freshwater content from fully coupled MPI-ESM (left), and from partially coupled Modini-MPI-ESM simulations with wind anomaly forcing from NCEPcfsr (right) in the Arctic Ocean and in the Subarctic North Atlantic. Solid line indicates the mean, shaded area indicates the standard deviation of 10 ensemble members.*

Here it should be stressed that the Modini-MPI-ESM runs on the right panel of Figure 4.17 are identical to their parent fully coupled control runs on the left panel at the start of 1979, and differ from them only in the wind stress forcing from then on. The difference in the results from the different model configurations can be attributed to the effect of the wind stress forcing, confirming its primary role in shaping the freshwater variability in both domains, and also the potential covariability between them.

4.4.   Discussion

The atmospheric model component of MPI-ESM is known to overestimate sea-level pressure in much of the Arctic, and over Greenland (Stevens et al., 2013); however, the simulations successfully reproduce the main features of sea-level pressure and the large-scale wind systems in the Arctic and in the Subpolar North Atlantic. Their differences across the ensemble are remarkably small: the simulations of their mean climatology and variability are robust across the ensemble, unlike those of the freshwater content presented in the previous chapter. Even though many earth system models misinterpret the physical processes connected to the NAO, MPI-ESM is able to properly capture its main properties (Davini and Cagnazzo, 2014). This is confirmed by this work, as the analyzed modes of large-scale atmospheric variability, namely the AO and NAO patterns are well reproduced by the model, and their patterns are also stable over time and similar in all members of the ensemble.

A connection between Arctic freshwater content and atmospheric circulation has been suggested by many studies before, both for its liquid component (e.g. Proshutinsky and Johnson, 1997; Proshutinsky et al., 2009; Giles et al., 2012; Stewart and Haine, 2013; Rabe et al., 2014) and for sea ice (e.g. Dickson et al., 2000; Wu et al., 2006; Ionita et al., 2016). Great Salinity Anomalies in the Subarctic North Atlantic have also been linked to atmospheric variability (Haak et al., 2003; Karcher et al., 2005; Mauritzen et al., 2012). However, the results presented here show no robust link between the main modes of large-scale atmospheric variability and the changes in freshwater content. There is only a weak positive correlation between the simulated AO and the Subarctic North Atlantic liquid freshwater content, and a weak negative correlation between the NAO and the Arctic total freshwater content in the ensemble mean.

Repeating the analysis for arbitrarily selected multidecadal subperiods in individual members of the ensemble reveals a large internal variability of the system. Different selections of the member and the time period yield fundamentally different results, ranging from significant positive to negative correlations for the same parameters. These differences are likely to originate in the different oceanic states of the simulations that exhibit a large internal variability in the model (see the ensemble variability of freshwater content in the previous chapter). It appears that changes in large-scale atmospheric circulation regimes can potentially correspond with freshwater anomalies both in the Arctic Ocean and in the Subarctic North Atlantic, but the link between them is not stable over time. This is consistent with previous studies that found a similarly unstable link. For example, Hilmer and Jung (2000) found a significant positive correlation between the NAO and Arctic sea ice export for the years 1978–1997, but found no correlation for the preceding two decades, whereas Vinje (2001) reported a negative correlation during 1962–

1978. Dickson et al. (2000) also noted that an anomalous freshwater export from the Arctic to the Subarctic North Atlantic, significantly influencing their freshwater contents, can occur during both extrema of the NAO. The regional variations of sea-level pressure in the Arctic that control the liquid freshwater variability have also been found to be partly related to the AO, but to act intermittently as well (Carmack et al., 2016).

The 10 members of the MPI-ESM ensemble analyzed here cover a total of 1470 years, and it is likely safe to assume that they capture all main features of the variability in the atmosphere-freshwater link over such a long period. The results show a stable simulation of the AO and NAO indices, but there is a striking lack of a robust link between their time series and the freshwater anomalies. This suggests that while these indices do describe the main modes of atmospheric variability, their patterns might not represent the most relevant modes for driving the freshwater anomalies. The most relevant modes might also be different for the liquid and the solid components.

The value of the redundancy analysis performed here is that it not only links variations of certain patterns in freshwater content to patterns of atmospheric variability, but also gives a measure of how much of the total freshwater variance is described by these patterns, and provides information on how persistent their link is over time. As the analysis was based on the concatenated time series of the ensemble members totalling up to 1470 years, it provides reliable results that can be considered robust across the ensemble.

The results of the redundancy analysis show that the liquid and solid components of freshwater content are linked to different patterns of atmospheric circulation. Moreover, the variability of both components can be further separated into different modes, based on their different atmospheric driving patterns.

Variations in the atmospheric circulation-driven liquid freshwater content are separated into different modes. The leading two of these are distinct patterns connecting the freshwater content of the different basins. The correlation coefficient of the time series of the leading mode and the Arctic liquid content is r=0.41, and the strength of the second mode correlates with the total Subarctic North Atlantic freshwater content with a coefficient of r=0.54. The main drivers of these two modes resemble (but are not identical to) the AO and the NAO, respectively. The results suggest that during times when these corresponding atmospheric patterns anticorrelate, there is a higher potential for an anticorrelation between the Arctic and the Subarctic North Atlantic freshwater contents. However, these two leading modes together describe only a third of the liquid freshwater variance in the Arctic-Subarctic joint system. This means that during most of the time, the combinations of further modes can effectively mask the effect of the leading two, even when they happen to anticorrelate.

The results might help explain the great extent of internal variability of the Arctic-Subarctic North Atlantic freshwater system, and the controversies in our current understanding of its atmospheric drivers. The findings presented here confirm that anomalous flushes of liquid freshwater from the Arctic into the Subarctic North Atlantic can occur under different atmospheric circulation patterns, although it is most likely to happen during a persistent positive state of AO or NAO, as suggested by previous studies (e.g. Köberle and Gerdes, 2003; Zhang et al., 2003; Häkkinen and Proshutinsky, 2004; Karcher et al., 2005; Houssais et al., 2007; Condron et al., 2009). But even during such an anomalous Arctic export, an anticorrelation between the two domains still might not be realized due to the combined effect of further modes of freshwater variability. These are difficult to interpret, as they describe smaller and smaller parts of the total variability, and are more likely to be only statistical results without real physical significance, together with their corresponding atmospheric patterns. In addition to the variability of the liquid component, the solid freshwater also shows distinct patterns of variability.

For the solid freshwater content, the first RDA mode of sea-level pressure defines the strength of the winds along the Transpolar Drift, and the corresponding solid freshwater content mode shows that the stronger these winds are, the more sea ice is moved from the Siberian shelf seas towards and across Fram Strait. This confirms that Arctic sea ice redistribution, and especially variations in its export through Fram Strait are partly driven by local atmospheric changes unrelated to the AO, consistent with previous findings (Häkkinen and Geiger, 2000; Vinje, 2001; Koenigk et al., 2006; Wu et al., 2006). However, the second RDA mode describes a similarly large part of the total variance in sea ice, but its corresponding atmospheric pattern is similar to the NAO, confirming the results of other studies as well that related Arctic sea ice changes to the NAO (Köberle and Gerdes, 2003; Kwok et al., 2004).

In order to confirm the influence of wind stress forcing on freshwater anomalies, parts of the model runs were repeated using prescribed wind data based on observations. These partially coupled runs, although they are identical to the fully coupled control runs in every other aspect, show fundamentally different freshwater results. The ensemble variability is greatly reduced, and the freshwater anomalies are similar in size and timing for different members, even though they are still unconstrained except for the wind forcing.

The partially coupled runs show a strong increase of freshwater content (about 10,000 km^3) in Subarctic North Atlantic freshwater content in the late 1980s. This is a result of an anomalous transport across the southern boundary of the domain, which cannot be seen in observations. However, during 1990–1995 there is an additional freshening of about 5,000 km3 in the North Atlantic, corresponding to the Great Salinity Anomaly of the 1990s reported by Belkin (2004). This anomaly corresponds to a reduction of a similar size

in the Arctic freshwater content. This change already begins in the last years of the 1980s, consistent with Karcher et al. (2005) who identified an Arctic change as the reason of 1990s GSA. The anomalies in the two domains correspond between 1990 and 2005, with a decrease in the Subarctic content and an increase in the Arctic content back to the level before the 1990s event. After 2005 the Arctic content stabilizes at a high level, which is also consistent with observations (Zhang et al., 2016), while the Subarctic North Atlantic content keeps decreasing gradually, due to anomalous fluxes from the south. The successful reproduction of the 1990s GSA in the partially coupled runs implies that this event was mainly wind-driven, and that its signs could already be seen in the Arctic before the freshening in the North Atlantic began.

4.5. Conclusions

The objective of the work presented in this chapter was to identify key patterns of atmospheric variability that govern the changes in Arctic and Subarctic North Atlantic freshwater content through wind forcing. This was attempted by deriving the AO and NAO patterns from the results of fully coupled MPI-ESM simulations, and analyzing the covariability of their time series with changes of freshwater content.

The results showed that there are short multidecadal periods in individual members of the ensemble when a link between the AO or the NAO and the Arctic or the Subarctic North Atlantic freshwater content is present. The strongest identified links were a positive correlation between the AO and the Subarctic freshwater content, and a negative correlation between the NAO and the Arctic freshwater content. However, none of these links were stable over a longer time period or robust across the ensemble. This implied that these links can potentially exist, but the oscillation indices do not describe the patterns of atmospheric variability most relevant for driving freshwater anomalies, and there must be further modes of freshwater variability driven by different atmospheric regimes. These were investigated by performing a redundancy analysis of the simulated atmospheric sea-level pressure and freshwater content.

The redundancy analysis identified the most important patterns of atmosphere-driven freshwater variability, and quantified the strength of their links to their respective atmospheric forcing patterns. The results showed that about a third of the total liquid freshwater content variability of the joint Arctic-Subarctic North Atlantic system could be explained by patterns of opposing anomalies in their domains. The strength of these anomalies are linked to patterns of atmospheric variability reminiscent of (but not identical to) the AO and the NAO. The major modes of solid freshwater content variability showed a redistribution between opposing sides of the Arctic Ocean, primarily driven by

atmospheric patterns local to the Arctic that otherwise explain only a small part of the total hemispheric variance in sea-level pressure.

The results of the redundancy analysis highlight that not only the liquid and the solid components of freshwater content have different atmospheric drivers, but different modes of their variability are also driven by different atmospheric circulation patterns. The total freshwater anomalies are the result of the combination of these different modes. An attempt to connect these anomalies to oscillation indices can explain only a minor part of their variability. Better results can be achieved if further modes of atmospheric variability are included as well, and identifying these modes by taking into account the freshwater variability yields the best results.

Still, a main hypothesis of this study, namely that the freshwater anomalies are driven by wind stress forcing associated with large-scale patterns of atmospheric variability, is still not confirmed. The drivers of the anomalies might be other parameters associated with the atmospheric patterns, as these patterns were based on the variability of sea-level pressure, not wind. The partially coupled model simulations with prescribed wind forcing were able to reproduce the observed freshwater anomalies of the 1990s in the Arctic and in the North Atlantic, confirming the connection of their anomalies, and that in their formations a key driver was the wind stress forcing. However, they did not provide a confirmation of actual physical processes behind the forcing patterns identified by the redundancy analysis, whose results might be purely statistical artifacts.

In order to explain the physical processes that lead to the freshwater anomalies driven by wind stress forcing associated with the identified patterns of atmospheric variability, further model experiments were needed. The flexibility of the Modini approach enabled the construction of wind forcing scenarios through which the direct effect of wind stress forcing could be investigated. These scenarios were created by perturbing the forcing wind field in accordance with certain patterns of atmospheric variability identified by the redundancy analysis, and their results are presented in the following chapter.

5. Idealized Wind Forcing Scenarios

The previous chapter presented a statistical analysis whose results identified certain patterns in atmospheric sea-level pressure variability that are linked to major modes of freshwater variability. The first two of the liquid modes represent large freshwater anomalies in the Arctic Ocean, and in the Subpolar North Atlantic Ocean, respectively. The time series associated with these modes and their corresponding atmospheric patterns imply that a freshwater covariability can be observed when the identified first two atmospheric patterns of variability are in opposing phase, and cannot be observed, when they are not, or when large anomalies of further patterns are dominating.

In addition, repeated model runs with prescribed wind anomalies confirm the key role of atmospheric momentum forcing. The results suggest that the main driving force of the freshwater anomalies is the wind stress, associated with large-scale patterns of atmospheric pressure. The Modini-MPI-ESM simulations with wind anomaly forcing based on the NCEPcfsr dataset show an Arctic-North Atlantic freshwater covariability similar to observed trends in recent decades, with a reduced ensemble variability.

This chapter presents findings from model experiments with idealized wind forcing scenarios. These were constructed according to key features of atmospheric variability that can also be seen in the results discussed in the previous chapter, and serve the purpose of confirming the existence of physical processes behind the results of the statistical analysis. Moreover, these experiments also provide an opportunity to test the initial hypothesis that the main driver of Arctic-North Atlantic freshwater anomalies is the wind stress forcing. In order to achieve these goals, a careful design of the experiments was essential.

5.1. Experiment Design

Model simulations in this chapter were based on a fully coupled MPI-ESM run that used the same setup and greenhouse gas forcing as the historical CMIP5 scenario until 2005, and the RCP4.5 emission scenario afterwards. The control run of the targeted experiments was a partially coupled Modini-MPI-ESM run, restarted from that fully coupled run in 1979. The source of external wind data for computing the surface stress in this run was the NCEPcfsr (Saha et al., 2010). Note that this control run is identical to the first member of the prescribed wind-driven Modini-MPI-ESM ensemble (Modini_00) presented in

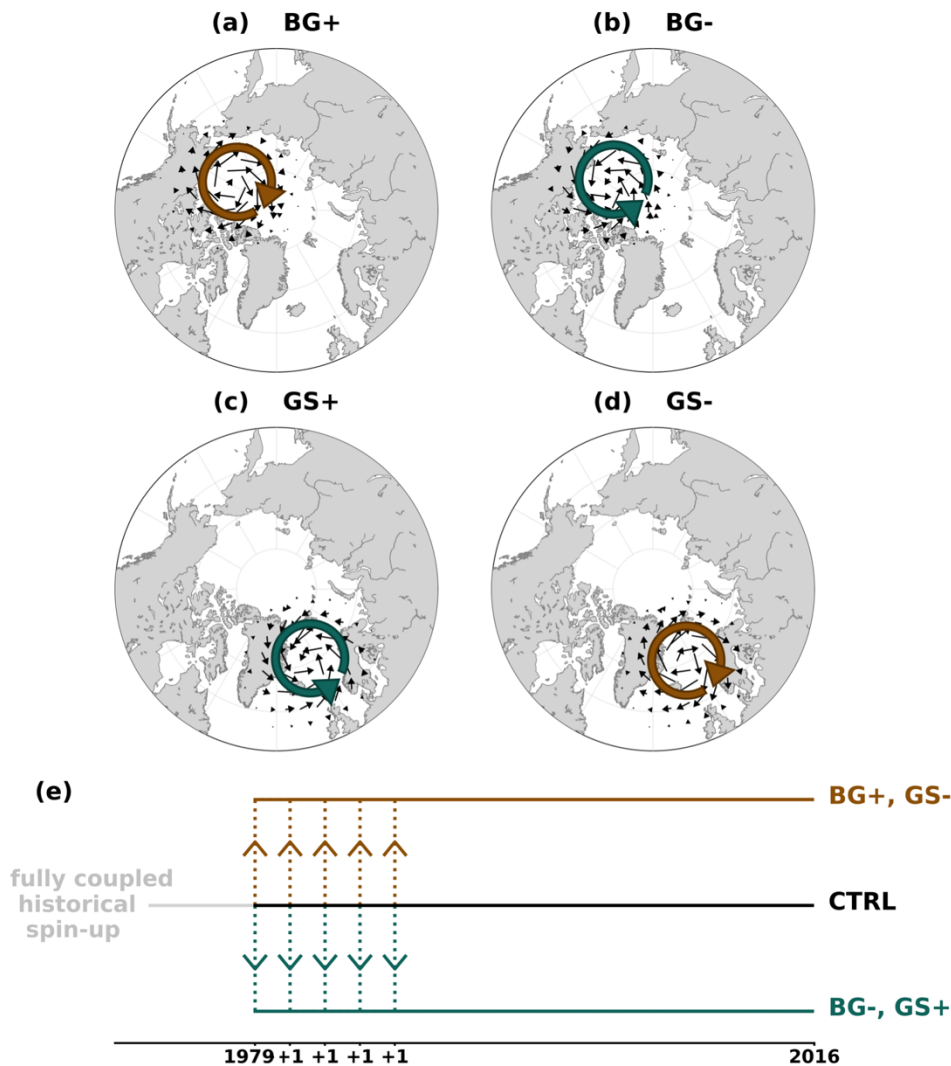Chapter 4.3, and is different from the fully coupled runs of the previous chapters, named CTRL_00–09.

Figure 5.1. *Experiment design. Location (a-d) and timing (e) of wind forcing perturbations: (a) Anticyclonic wind anomaly over the Beaufort Gyre, BG+, (b) Cyclonic wind anomaly over the Beaufort Gyre, BG-, (c) Cyclonic wind anomaly over the Greenland Sea, GS+, (d) Anticyclonic wind anomaly over the Greenland Seas, GS-.*

Then additional model experiments were run with locally perturbed wind forcing scenarios. These were constructed following Marshall et al. (2017), who suggested several perturbations to different forcing fields as a step change of idealized anomalies, including changes in wind forcing, freshwater forcing (river runoff, evaporation and precipitation), and Pacific and North Atlantic Water inflow into the Arctic Ocean. From those scenarios, four were selected here that closely correspond to the results of the statistical analysis of the atmospheric drivers of freshwater anomalies presented in Chapter 4.2.2: the perturbation of the wind field in the Canadian Arctic, centered over the Beaufort Gyre at 77° N and 147° W, and at lower latitudes, centered over the Greenland Sea at 71° N and

6° W. These perturbations, shown on Figure 5.1, are essentially modifications of the local cyclonicity in the prescribed wind forcing. Two scenarios with a step change in atmospheric circulation were created for both locations, resulting in a total of four perturbations:

- an anticyclonic circulation anomaly over the Beaufort Gyre (labeled BG+),
- a cyclonic circulation anomaly over the Beaufort Gyre (labeled BG-),
- a cyclonic circulation anomaly over the Greenland Sea (labeled GS+),
- an anticyclonic circulation anomaly over the Greenland Sea (labeled GS-).

The labels correspond to changes in the strength of the corresponding local atmospheric feature, rather than the cyclonicity. BG+ is associated with an enhanced Beaufort High, and thus represents an anticyclonic anomaly, while GS+ is associated with an enhanced Icelandic Low, and is thus a cyclonic anomaly. This can be seen on Figure 5.1a-d, where the colors, however, represent the cyclonicity.

The perturbations are step changes in the near-surface geostrophic winds associated with a sea-level pressure anomaly of 4 hPa, with a radius of influence of about 1000 km, following Marshall et al. (2017). The experiments cover the same time period as the control run (1979-2016). In order to assess the robustness of the response, an ensemble of five members was created for each of the four scenarios by lagged introduction of the forcing anomalies. The step change was introduced in 1979 for the first member, and it was delayed an additional year for each subsequent member (see Figure 5.1e).

5.2.   Beaufort High Perturbations

The prescribed wind anomalies modify the underlying oceanic currents and sea ice motion through transfer of kinetic energy. In this part, results are presented from model simulations with wind perturbation associated with the strength of the Beaufort High. The control run (CTRL) uses prescribed wind anomaly forcing based on the NCEPcfsr data product, and the perturbations use the same forcing, except for an anticyclonic (BG+), and a cyclonic (BG-) wind anomaly located over the Beaufort Gyre (see Figure 5.1).

First, characteristics of the horizontal circulation are assessed on the left panel of Figure 5.2 which presents the mean barotropic streamfunction in the control simulation. In this experiment, the Arctic Ocean is characterized by an anticyclonic circulation situated in the Amerasian Basin, corresponding to the Beaufort Gyre. The strength of this cell is above 2 Sv, with a maximum of 3 Sv located in the Canada Basin. The anticyclonic circulation extends across the Chukchi Plateau as far as the Lomonosov Ridge. The

Eurasian Basin is characterized by a cyclonic circulation reaching -4 Sv in the Nansen Basin. The horizontal circulation in the Arctic Ocean is relatively weak, compared to for example the Nordic Seas, where the strength of the cyclonic circulation reaches -10 Sv.
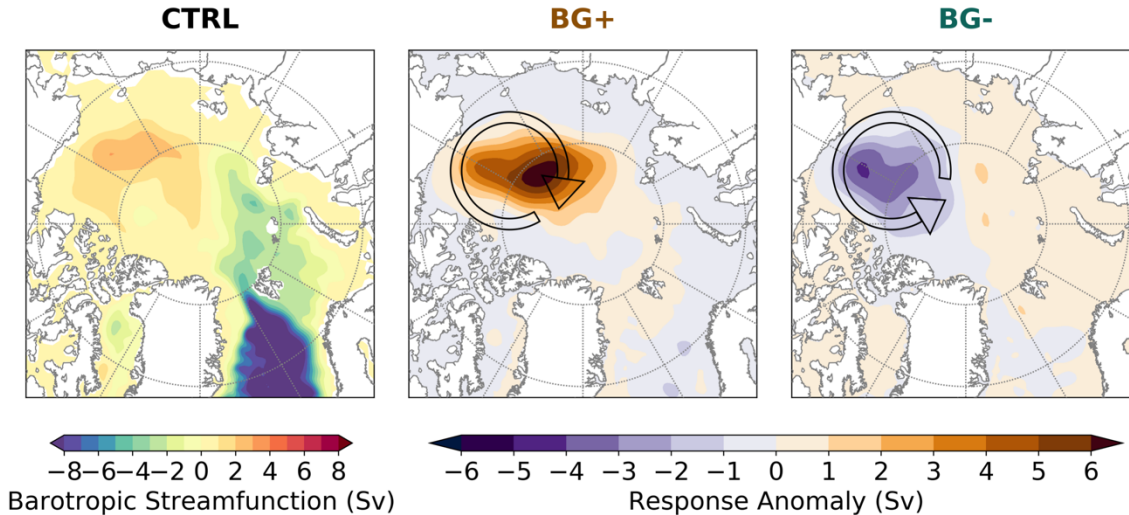

Figure 5.2. *Oceanic circulation response to the BG wind perturbations (black contours in middle and right panels) as anomalies to the mean barotropic streamfunction of the control run for the period 1998-2013 (left). Ensemble mean anomalies for the last 15 years of model simulation, 20 years after the step change in forcing in the BG+ (middle) and the BG- (right) scenarios.*

The response of the barotropic horizontal circulation to the BG+ and BG- wind scenarios is shown on the middle and right panels of Figure 5.2. The changes are confined to the Amerasian Basin, and are larger than the mean values of the control run in both scenarios. The anticyclonic circulation is significantly enhanced in the BG+ scenario, more than doubling in strength. The response anomaly exceeds +3 Sv in a large area stretching from the Canada Basin to the Lomonosov Ridge, with a maximum of more than +6 Sv situated north of the Chukchi Plateau around 80°N. There is no significant change outside of the simulated range of the Beaufort Gyre. The response to the cyclonic wind anomaly of the BG- scenario is a cyclonic circulation anomaly that is large enough to turn around the direction of the gyre. The pattern of the response anomaly is centered in the Canada Basin, and does not cross the Mendeleev Ridge. It is mostly between -1 and -3 Sv, with the largest anomaly of -4 Sv located in the central Canada Basin. Apart from a weak anticyclonic response along the Lomonosov Ridge reaching +1 Sv, no further anomalies can be observed in the Arctic Ocean, or outside of it.

Figure 5.3 focuses on further characteristics of the Beaufort Gyre. According to the top left panel, the simulated sea surface height within the Arctic Ocean mostly corresponds to the patterns in the horizontal circulation, except for the shallower shelf seas, especially where major rivers discharge large amounts of water. Apart from these locations, sea surface height in the Arctic Ocean is generally below 0 m in the control run.

The highest value is around the middle of the Beaufort Gyre, reaching -0.05 m. Outside of the gyre, the values are lower, down to -0.2 m in the Amerasian Basin. Sea surface height is much lower in the southern Eurasian Basin and in the Nordic Seas, where values are below -0.4 m.
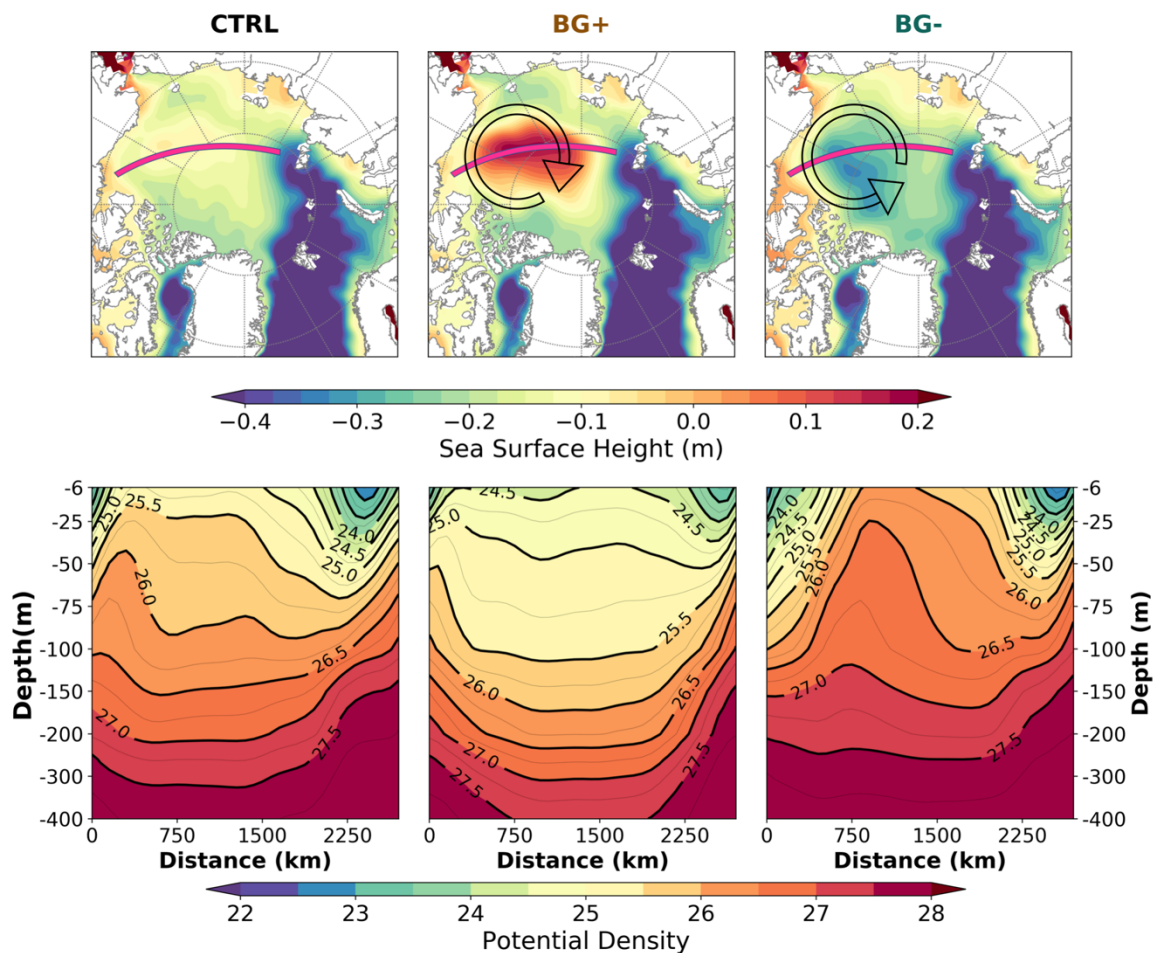

Figure 5.3. *Response of the Beaufort Gyre to the BG wind perturbations (black contours in top middle and right panels), illustrated by maps of the sea surface height (top row) and cross sections of potential density along the pink line (bottom row). The plots show the control run (left) and the ensemble mean of the BG+ (middle) and the BG- (right) scenarios for the last 15 years of model simulation, 20 years after the step change in forcing.*

The effect of the wind perturbations is most evident in the Amerasian Basin, centered in the Beaufort Gyre. The top middle panel of Figure 5.3 shows the sea surface height averaged for the last 15 years of the BG+ run, 20 years after the step change in forcing. The response is dominated by an increase in sea surface height in the Beaufort Gyre, where values reach +0.2 m. The extent of the increase is rather large, covering the entire area of the simulated gyre. Outside of the gyre, there is a slight decrease in some of the Arctic shelf seas, contributing to a much larger contrast of sea surface height between the center of the gyre, and outside of it. The response in the BG- scenario (top right panel of Figure 5.3) is the opposite, with some notable differences. The cyclonic wind perturbation in this

scenario results in a decrease of sea surface height in the Amerasian Basin. The changes are more confined to the Canada Basin, where values reach as low as -0.3 m. Sea surface height slightly increases in most of the Arctic shelf seas, in particular in the Canadian Arctic Archipelago. In this scenario the region of the Beaufort Gyre is characterized by a depression in sea surface height, suggesting a fundamental change of its behaviour.

The applied wind perturbations modify the characteristics of the Beaufort Gyre not only on the ocean surface, but also in the upper few hundred meters of the water column beneath the surface. This is shown in the bottom panels of Figure 5.3 that present vertical cross sections of potential density down to -400 meters depth along a line crossing the Beaufort Gyre, marked with a pink line in the top panels of Figure 5.3. Note that the depth shown in the vertical axis is not linear, in order to magnify the shallow layers where the differences are the largest. The bottom left panel shows the mean state in the control simulation. Close to the surface, the isopycnals are higher in the center of the gyre (up to about 25.7 kg/m³), and lower near the Canadian coast and towards the Eurasian Basin seen on the right side of the plot (around 23.5 and 23.0 kg/m³). This is mainly due to the lower surface salinity simulated by the model in these regions in comparison with the center of the gyre. However, this lower salinity and its effect on potential density is present only in shallow waters close to the surface. At -75 meters depth there is already no sign of it, and the potential density is the lowest in the gyre (about 26 kg/m³), compared to the regions outside of it. In deeper waters the distribution illustrates the location and the extent of the gyre even better, as it is characterized by waters of lower density. This is clearly visible even at -400 meters depth, where the potential density is still lower in the gyre (about 27.8 kg/m³) than outside of it.

The bottom middle plot of Figure 5.3 depicts the response of the Beaufort Gyre in the anticyclonic BG+ scenario. Compared to the control run, there are significant changes. Although the changes near the surface are relatively small, and the potential density is still higher in the gyre than outside of it, the vertical structure is different. The isopycnals sink much lower, illustrating the inflation of the gyre in the vertical. The anomalies reach -0.8 kg/m³ at -75 meters, -0.7 kg/m³ at -200 meters, and -0.3 kg/m³ at -400 meters, while changes outside of the gyre (at the left and right side of the plot) are much smaller. The response in the cyclonic BG- scenario is roughly the opposite. As seen on the bottom right plot of Figure 5.3, the isopycnals do not change significantly outside of the gyre, but they rise considerably within the gyre. A notable difference is the large anomaly at the surface, where in this scenario an anomaly of up to about +1.0 kg/m³ is visible in the center of the gyre. The anomalies reach +0.7 kg/m³ at -75 meters, +0.3 kg/m³ at -200 meters, and about +0.1 kg/m³ at -400 meters. Overall, the pattern of the changes illustrate the deflation of the gyre in the vertical. In fact, its typical structure completely disappears in the BG- scenario,

where the potential density is actually larger within the former area of the gyre than outside of it everywhere in the vertical water column.

The changes in potential density are mainly due to changes in salinity. This can be illustrated through the analysis of liquid freshwater content, which is based on the vertical integral of salinity. The time series of annual means of liquid freshwater content stored within the Beaufort Gyre is shown on Figure 5.4. The area of the gyre here does not strictly follow the simulated area of the gyre (although there is a considerable overlap), but rather corresponds to the area (130-170°W, 70.5-80.5°N) used by Marshall et al. (2017) for the sake of comparability.

On the left panel of Figure 5.4, annual means of the Beaufort Gyre liquid freshwater content are shown as a function of time for the control experiment, and for each five-five members of the BG+ and the BG- ensemble. According to the plot, the model is rather stable; no significant trend can be observed during the 38 years of simulation. Annual values in the control experiment are between 20,000 and 23,000 km³. Considering that the area of the region on the model grid is 1.36×10^6 km², this equals to an approximately 15-16 meter thick layer of freshwater evenly distributed in the region. The lower values are in the 1990s and early 2000s, and there is an increase of about 2,000 km³ after 2007. These changes roughly correspond to those seen in observations, especially the increase in the late 2000s (Rabe et al., 2014), and also the prevailing high values following the increase that are likely connected to the observed stabilization of the gyre, controlled by atmospheric changes in the Canada Basin (Zhang et al., 2016). The important role of the local wind forcing is evident in the perturbed time series shown on the left panel of Figure 5.4: the changes in both scenarios are larger than the range of variability in the control run, with a rather small difference between members of the ensemble.
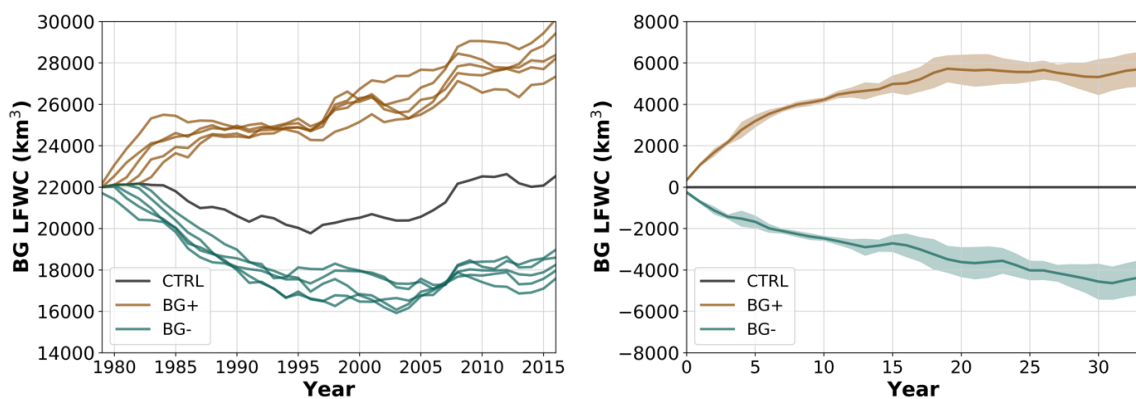

***Figure 5.4.** Beaufort Gyre liquid freshwater content response to the BG wind perturbations as absolute values in the control run and members of the BG+ and BG- ensemble (left), and as anomalies in comparison with the control run (right), where the solid line indicates the mean, the shaded area indicates the standard deviation of five-five ensemble members.*

The time evolution of the response of the Beaufort Gyre liquid freshwater content as anomaly to the control run is presented on the right panel of Figure 5.4. The response is well pronounced in both scenarios, and it is slightly asymmetric in terms of the forcing. In the anticyclonic BG+ scenario, freshwater content quickly increases in the beginning. The anomaly reaches 2,000 km^3 in three years after the step change in forcing, and after 10 years it is above 4,000 km^3. After 10 years the increase is much slower, and the anomaly finally stabilizes around 5,500 km^3 after between 15 and 20 years following the time of perturbation. In the cyclonic BG- scenario the response is somewhat smaller, and more linear. After three years the response anomaly is about -1,500 km^3, and then grows gradually. It reaches -2,500 km^3 after 10 years, and -4,000 km^3 after 25 years following the step change in forcing, and shows no such clear equilibrium as the BG+ scenario.

The spatial pattern of liquid freshwater response to the BG+ and BG- scenarios is shown on Figure 5.5. The plots present the response in the Arctic Ocean as annual mean anomalies to the control run after 3, 10, and 30 years following the step change in forcing.

The top row of Figure 5.5 shows the results of the anticyclonic wind perturbation of the BG+ scenario. The spatial development of the response can be clearly seen. After 3 years the anomaly is mostly confined to the Canada Basin, where it reaches 3 meters. By year 10, the anomaly extends both in space and in amplitude, covering most of the deep Amerasian Basin, and crossing even the Lomonosov Ridge all the way until Severnaya Zemlya. The anomaly exceeds 2 meters in a large area, and has a maximum of about 7 meters that is located a little north of the Chukchi Plateau. A small change of opposite sign outside of the gyre region can also be observed in shallower shelf seas, especially in the Canadian Arctic Archipelago. After 30 years, the anomaly covers roughly the same area, but it is even stronger. The increase exceeds 4 meters in a large area, and has a maximum of about 10 meters. It is notable how the location of the maximum shifts from the Canada Basin towards the central Arctic.

Maps of freshwater response to the cyclonic BG- scenario are presented in the bottom panels of Figure 5.5. Compared to the BG+ scenario, the anomalies are weaker and more confined to the Amerasian Basin. After 3 years there is not much change outside of the Canada Basin, where anomalies reach -2 meters. After 10 years following the step change in forcing, the anomalies are much larger, reaching -6 meters, and are more spread especially to the east towards Greenland. A weak response of opposite sign is present around the Canadian Arctic Archipelago in this scenario as well, but not in the Siberian shelf seas. After 30 years, the response extends into the Eurasian Basin towards Fram Strait, while the location of the maximum, now reaching -9 meters, does not change.
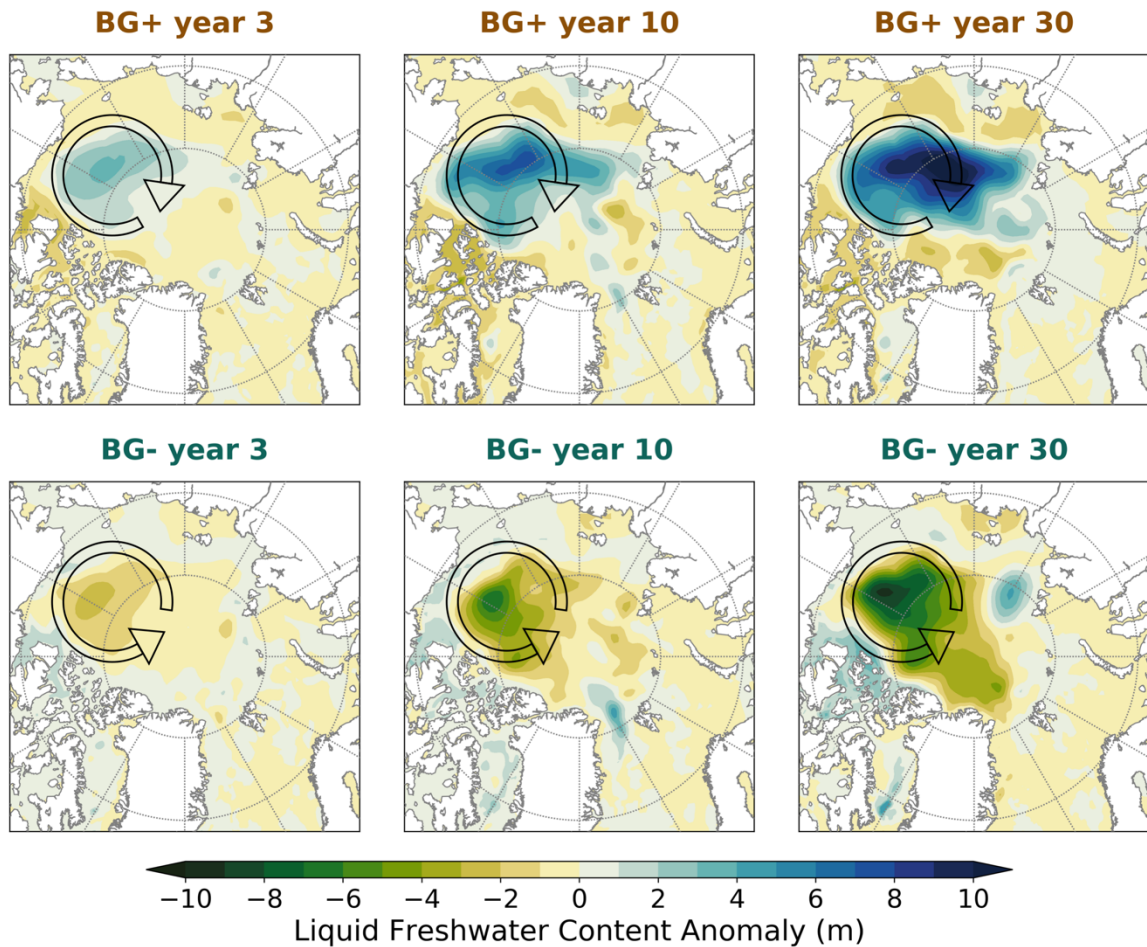
Figure 5.5. *Arctic liquid freshwater content response to the BG wind perturbations (black contours). The panels show the ensemble mean anomalies of the BG+ (top row) and the BG- (bottom row) scenarios in comparison with the control run as annual means of the 3rd (left), the 10th (middle), and the 30th (right) year following the step change in forcing.*

Wind forcing has a significant impact on sea ice motion, therefore it is interesting to assess its response to the wind perturbations as well. Time series of Arctic sea ice extent and volume are presented on Figure 5.6. The top left panel shows absolute values of annual mean sea ice extent in the control run, and in all five-five members of the BG+ and BG- ensemble. The control run of the model simulates rather stable annual ice extent until about the year 2000, and when a decreasing trend begins. Considering the anomalies, no clear response is visible. Plotting the time series as anomalies to the control run on the top right panel of Figure 5.6, the same can be observed. The two scenarios do not differ significantly from the control run, and the range of their ensemble variability is larger than the anomalies that their ensemble means show. The lack of response can be attributed to the fact that the changes are not robust enough to prevent the ice from forming in the winter, and do not melt enough ice in the summer either. Another explanation may be that the local changes are masked when the total Arctic ice extent is calculated. It is also true that ice extent has a maximum value, over which it cannot increase anymore.

Therefore in addition to its extent, the total Arctic ice volume might show additional information.
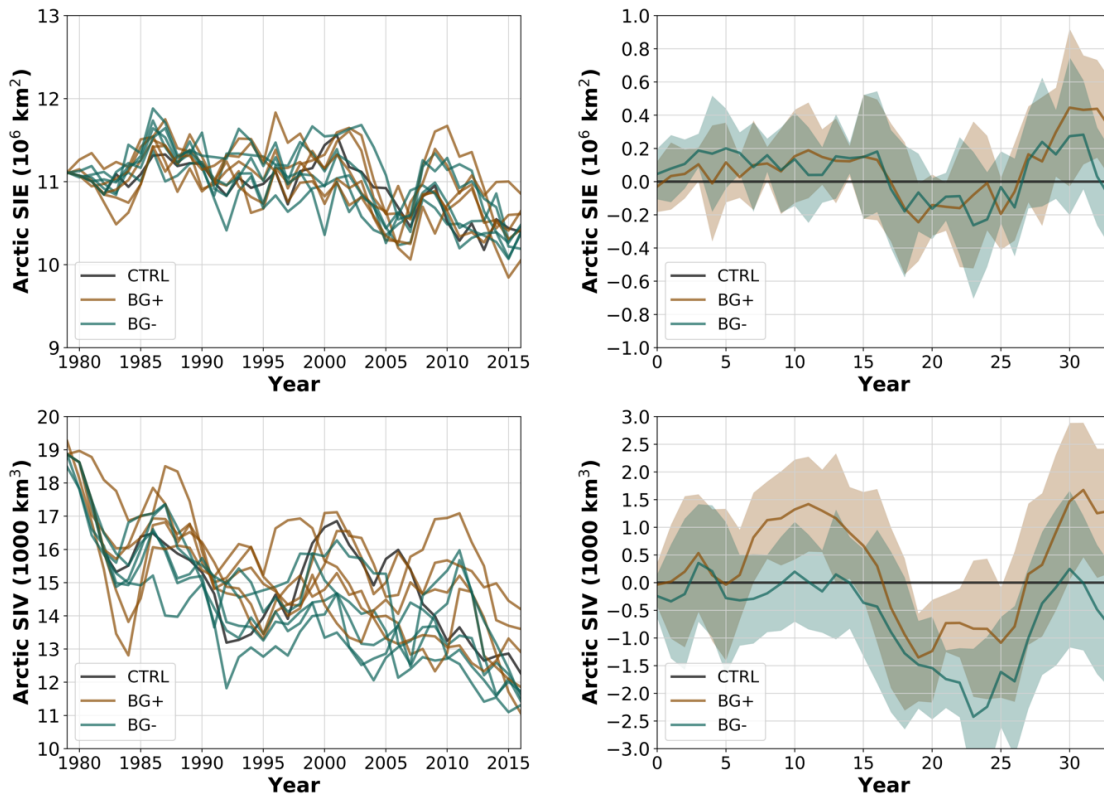

Figure 5.6. *Arctic sea ice extent (top) and volume (bottom) response to the BG wind perturbations as absolute values in the control run and members of the BG+ and BG- ensemble (left), and as anomalies in comparison with the control run (right), where the solid line indicates the mean, the shaded area indicates the standard deviation of five-five ensemble members.*

The time series of Arctic sea ice volume are presented on the bottom panels of Figure 5.6. In this metric there is a clear decreasing trend throughout the simulation period both in the control run, and in the BG+ and BG- scenarios as well. Plotting the results from the perturbed runs as anomalies to the control run, their differences are more apparent. In the anticyclonic BG+ scenario the total Arctic sea ice volume is higher than in the cyclonic BG-scenario, but the changes are not significant if they are compared to the control run. The ensemble variability is also larger than the response shown by the ensemble means. It is also interesting that in some cases both scenarios show similar anomalies, for example around years 20-25, where both of their values are lower than that of the control run.

Overall, no clear response can be seen in the time series of total Arctic sea ice. In order to estimate the possible local effects of the applied wind forcing anomalies, the spatial distribution of the sea ice thickness anomalies is shown on Figure 5.7 that presents the response in the Arctic Ocean. The panels of the figure show annual mean anomalies of sea ice thickness after 3, 10, and 30 years following the step change in forcing.
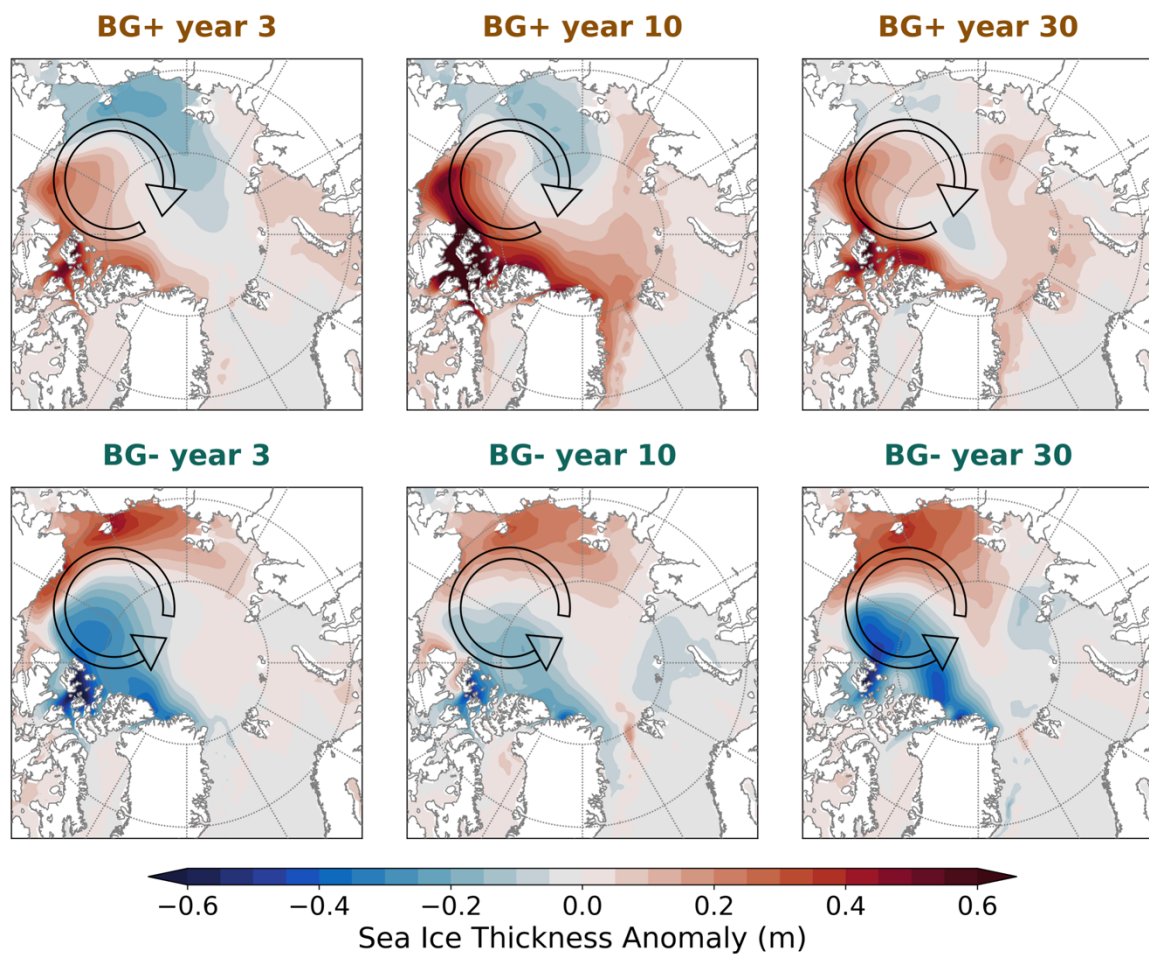
Figure 5.7. *Sea ice thickness response to the BG wind perturbations (black contours). The panels show the ensemble mean anomalies of the BG+ (top row) and the BG- (bottom row) scenarios in comparison with the control run as annual means of the 3rd (left), the 10th (middle), and the 30th (right) year following the step change in forcing.*

The response shows a seesaw-like pattern between the Canadian and the Siberian Arctic. According to the top panels of Figure 5.7, the wind perturbation of the anticyclonic BG+ scenario has a well pronounced effect on Arctic sea ice distribution. An anticyclonic wind anomaly over the Beaufort Gyre causes an increase of ice thickness in the Canadian Arctic, and a decrease in the East Siberian Sea and the Chukchi Sea, as well as along the Transpolar Drift. The increase reaches 0.5 meter in the Canadian Arctic Archipelago 3 years after stepping up the wind, while the negative anomalies reach -0.2 meter in the East Siberian Sea. Under continuous forcing anomaly conditions, the ice cover is further thickening in the Canadian Arctic, and after 10 years the extent of the positive anomaly stretches as far as the Eurasian Basin, as well as into the Nordic Seas across Fram Strait. Meanwhile, the negative anomaly remains rather weak. Towards the end of the simulation the pattern is similar, with an increased ice thickness in the Canadian Arctic, and a no change or slight decrease in the East Siberian Sea.

In the cyclonic BG- scenario, the seesaw consists of a decrease in ice thickness in the Canada Basin and north of Greenland, and an increase in the Siberian shelf seas. Small differences can be observed along the northern coast of Alaska, where an increase is present in both scenarios. Also, the amplitudes of the two anomalies are more balanced in the BG- scenario, and the response appears to be more stable over time. However, it should be noted that the years shown on Figure 5.7 are arbitrarily selected snapshots to illustrate the response. Arctic sea ice cover shows large interannual variability in the model simulations, and the amplitude of the anomalies can be substantially different in other years. For example, around 20 years into the BG+ scenario, the negative anomaly has a larger extent, and is stronger than the positive anomaly for a few years (not shown). Nevertheless, Canadian-Siberian seesaw pattern persists throughout both scenarios, and can therefore be considered a robust result.

5.3.   Greenland Low Perturbations

In this chapter, model results using wind perturbations associated with the strength of the Greenland Low are presented. Similarly to experiments in the previous chapter, the control run (CTRL) is a partially coupled Modini-MPI-ESM run that uses prescribed wind anomaly forcing based on the NCEPcfsr data product. The perturbed simulations cover the same time period from 1979 to 2016 and use the same wind forcing, except for a cyclonic (GS+) and an anticyclonic (GS-) wind anomaly located over the Greenland Sea (see Figure 5.1).
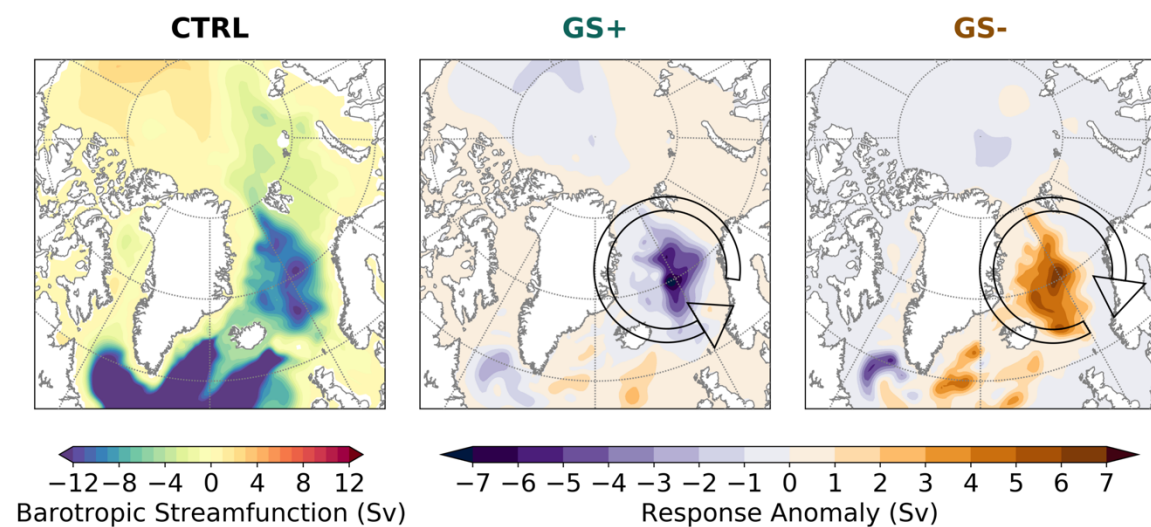

Figure 5.8. *Oceanic circulation response to the GS wind perturbations (black contours in middle and right panels) as anomalies to the mean barotropic streamfunction of the control run for the period 1998-2013 (left). Ensemble mean anomalies for the last 15 years of model simulation, 20 years after the step change in forcing in the GS+ (middle) and the GS- (right) scenarios.*

The applied wind forcing scenarios communicate an anomalous momentum transfer to the ocean. This can be clearly seen in the changes of the horizonal circulation, which is assessed on Figure 5.8. On the left panel of the figure, the mean climatology of the barotropic streamfunction of the control run is presented. The barotropic flow in the Arctic is presented in the beginning of the previous chapter; here focus is on the Nordic Seas. This region is characterized by a cyclonic circulation, reaching a strength of -13 Sv, which is similar to estimates based on profiling float observations (Voet et al., 2010). Values in the North Atlantic are much lower, reaching -20 Sv in the strong cyclonic cell of the Subpolar Gyre. The effect of enhanced cyclonic winds over the Greenland Sea is shown on the middle panel of Figure 5.8. The response anomaly after 20 years in this scenario reaches -7 Sv, increasing the strength of the cyclonic circulation significantly. No substantial anomalies can be observed outside of the Nordic Seas. In the anticyclonic GS-scenario, presented on the right side panel of Figure 5.8, there is a positive anomaly of up to 6 Sv in the Nordic Seas. Although this is not enough to change the cyclonic circulation regime, the response is large enough to significantly weaken it. In the Subpolar North Atlantic there are a few patches of weak anticyclonic circulation anomalies, as well as a cyclonic anomaly in the Labrador Sea. There is essentially no response in the Arctic Ocean.

The perturbations modify the wind forcing field over sections bordering the Nordic Seas, and are therefore expected to influence the lateral oceanic fluxes into and out of its basin. The following figures present time series of net water and liquid freshwater fluxes across the Iceland-Scotland Channel, the Barents Sea Opening, and Fram Strait from the control run and from the perturbed runs.

Figure 5.9 shows time series of fluxes across the Iceland-Scotland Channel. According to the top panels of the figure, the applied wind forcing perturbations have an influence on the northward flow of Atlantic Water into the Nordic Seas. In the cyclonic GS+ experiment, the southwesterly winds across the channel do not modify the amount of water crossing it; there is only a slight increase of up to 0.5 Sv in some years. However, the northeasterly winds of the GS- scenario gradually reduce the amount of Atlantic Water entering the Nordic Seas. The decrease reaches about 1 Sv after 15 years. Considering that this northward flowing water is rather saline, changes in its volume impact the freshwater fluxes. The response of these are shown on the bottom panels of Figure 5.9. In the GS+ scenario no clear response can be observed, the anomalies range from +500 km^3 to -500 km^3. These values are rather small compared to the control values that show changes of up to 2000 km^3 within a few years. There is a more pronounced response in the GS- scenario, where a gradual increase takes place after about 10 years, reaching an anomaly of 1200 km^3 after 20 years following the step change in forcing. Then the anomaly gradually diminishes again towards the end of the simulation. This positive anomaly is explained by a reduced inflow of saline Atlantic Water, that decrease the Nordic Seas

freshwater content a little less in the GS- scenario. This appears as an inflow of freshwater in the balance.
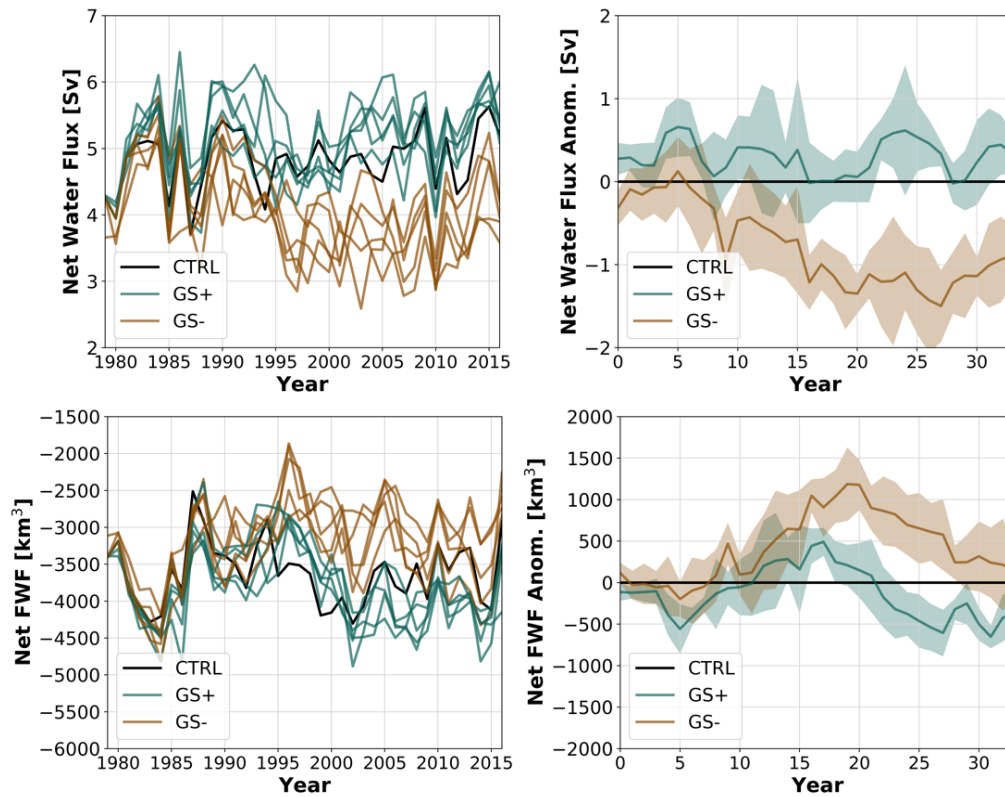

Figure 5.9. *Net oceanic lateral fluxes of water (top) and freshwater (bottom) through the Iceland-Scotland Channel. Response to the GS wind perturbations as absolute values in the control run and members of the GS+ and GS- ensemble (left), and as anomalies in comparison with the control run (right), where the solid line indicates the mean, the shaded area indicates the standard deviation of five-five ensemble members. Negative values indicate southward transport.*

Continuing along the pathway of Atlantic Water, Figure 5.10 presents time series of net water and liquid freshwater fluxes across the Barents Sea Opening. The applied wind forcing anomalies are parallel to this section in both scenarios, with southerly winds in the GS+, and northerly winds in the GS- experiment. The response in the amount of water transported across the opening is weak and shows no clear sign, as the anomalies are within +0.2 and -0.5 Sv in both scenarios. Similarly, no robust response can be seen in the freshwater time series on the bottom panels of Figure 5.10. The anomalies of liquid freshwater flux are small and nearly indistinguishable between the two scenarios.
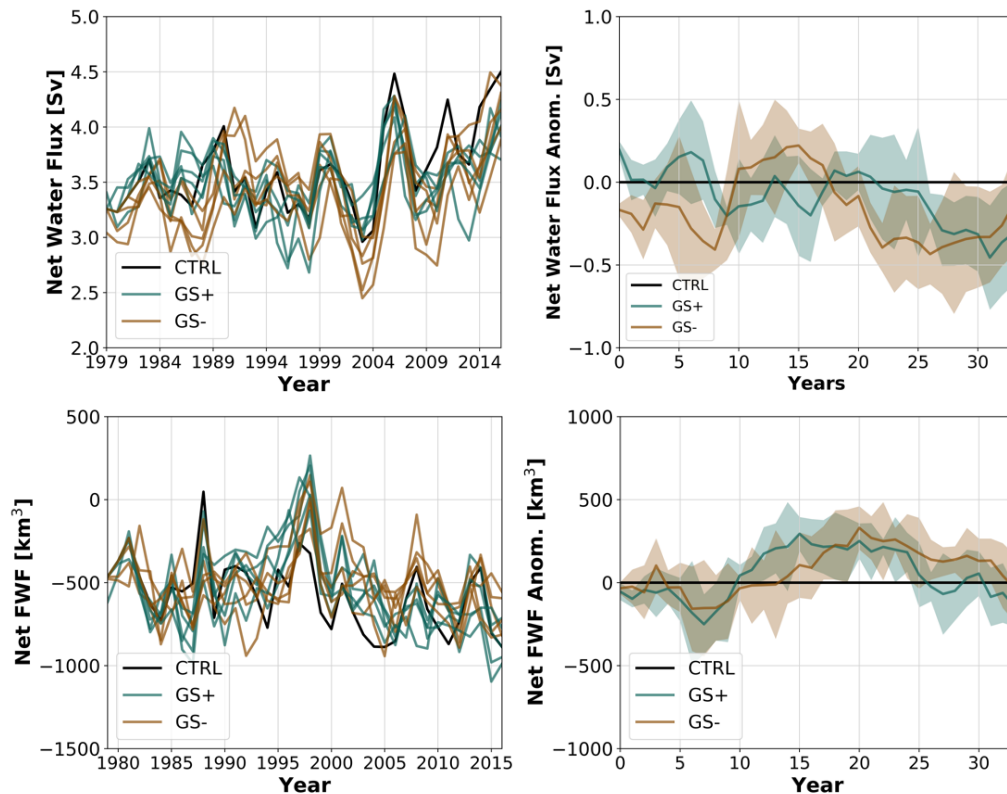
Figure 5.10. *Net oceanic lateral fluxes of water (top) and freshwater (bottom) through the Barents Sea Opening. Response to the GS wind perturbations as absolute values in the control run and members of the GS+ and GS- ensemble (left), and as anomalies in comparison with the control run (right), where the solid line indicates the mean, the shaded area indicates the standard deviation of five-five ensemble members. Negative values indicate southward transport.*

Time series of fluxes across Fram Strait are shown on Figure 5.11. The model simulates negative net fluxes of water, as this is one of the main southward export pathways of Arctic Water. The applied wind forcing anomalies around Fram Strait are northeasterly in the cyclonic GS+, and southwesterly in the anticyclonic GS- scenarios. Although the net water flux anomalies are not large, during the first 8 years following the perturbations the GS+ runs show somewhat lower values (i.e. stronger southward flow) than the GS- results. Then the sign of anomalies change, and the GS+ runs show higher values through the rest of the simulations, reaching +0.6 Sv, while the GS- response also increases, but does not exceed +0.2 Sv. The response in liquid freshwater flux (bottom panels of Figure 5.11) is a little clearer, although its values show a large interannual variability in the control simulation with a range of up to 2500 km^3 within a few years. There is no clear response of freshwater flux to the wind forcing anomalies in the first 10 years. After that, the GS+ results show an increase of up to 500 km^3, increasing to above 1000 km^3 in the last years of the simulations. The GS- results show a negative anomaly, as they are generally between 0 and -1000 km^3 during this time. Considering that positive values denote northwards flow, the responses mean a decreased liquid freshwater export

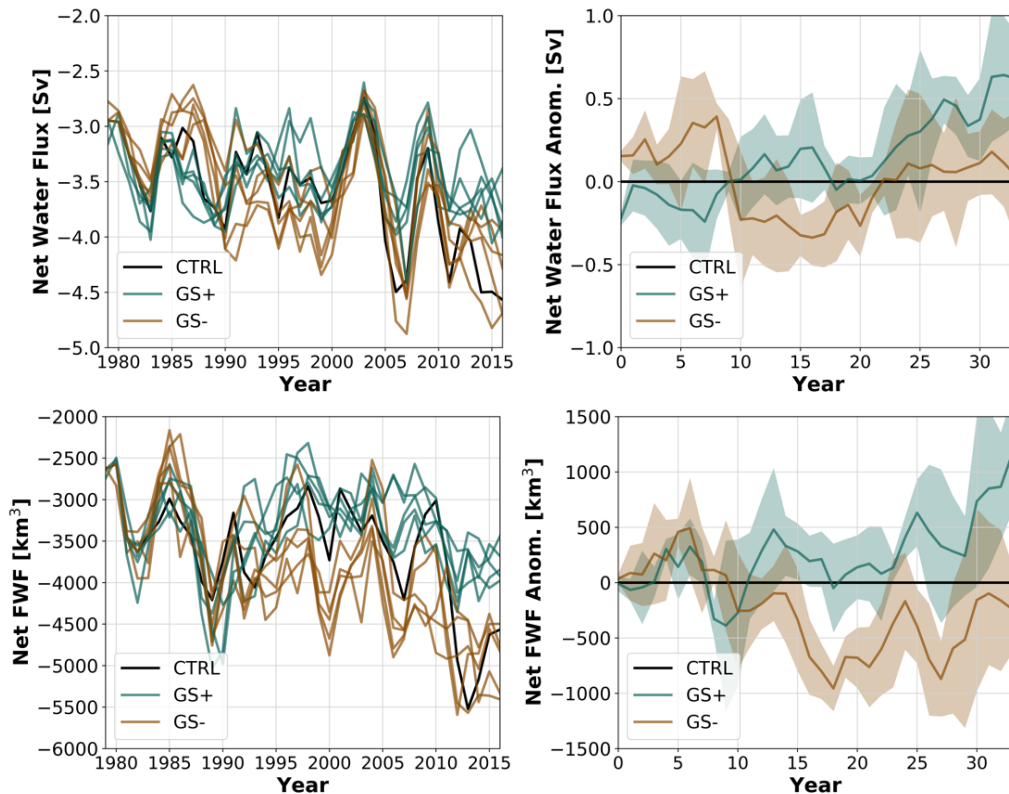from the Arctic through Fram Strait in the cyclonic GS+ scenario, and an increase in the anticyclonic GS- scenario.

Figure 5.11. *Net oceanic lateral fluxes of water (top) and freshwater (bottom) through Fram Strait. Response to the GS wind perturbations as absolute values in the control run and members of the GS+ and GS- ensemble (left), and as anomalies in comparison with the control run (right), where the solid line indicates the mean, the shaded area indicates the standard deviation of five-five ensemble members. Negative values indicate southward transport.*

The spatial evolution of liquid freshwater content response is presented on Figure 5.12. The panels of the figure show annual mean anomalies of sea ice thickness after 3, 10, and 30 years following the step change in forcing. From the results it is clear that there is a somewhat symmetric response in the Nordic Seas, especially along the East Greenland Current. The anomalies are much less robust outside of this region.

The upper panels of Figure 5.12 depict the response to the cyclonic GS+ scenario. The anomalies develop rather slowly, as no significant changes can be observed 3 years after the wind perturbation. In the following years, a positive anomaly of up to +4 meters develops north of Fram Strait in the Arctic by year 10, as well as a weak negative anomaly along part of the East Greenland Current. There is also an increase of liquid freshwater content in Baffin Bay. The latter two are rather stable in the following years, while the Arctic anomalies are not as robust. On the last snapshot shown here, by year 30, the Greenland Sea anomaly is greatly increased in extent and amplitude, reaching -5 meters. There is also a slight decrease in the Labrador Sea, and in the Arctic north of Fram Strait.
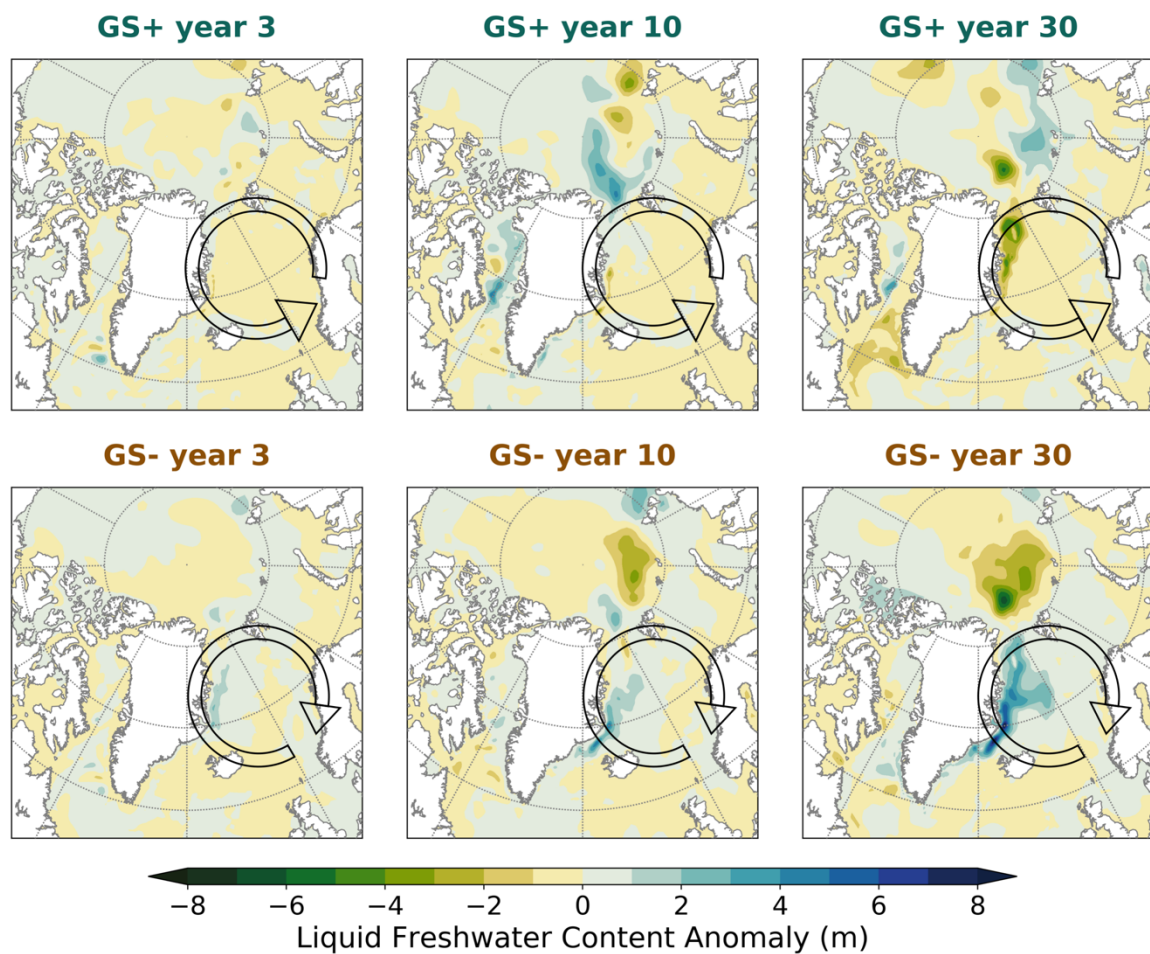
Figure 5.12. *Liquid freshwater content response to the GS wind perturbations (black contours). The panels show the ensemble mean anomalies of the GS+ (top row) and the GS- (bottom row) scenarios in comparison with the control run as annual means of the 3rd (left), the 10th (middle), and the 30th (right) year following the step change in forcing.*

On the lower panels of Figure 5.12 the response to the anticyclonic GS- scenario can be seen. The first years following the step change in forcing show no strong response, but even after 3 years there is already a small increase present in the East Greenland Current. This becomes stronger after 10 years, and by that time a response of opposite sign develops in the Arctic in the Eurasian Basin. These anomalies gradually increase in both size and strength, as it can be seen on the bottom right panel of the figure which shows the response 30 years after the perturbation. Liquid freshwater content increases in the Nordic Seas, by up to 7 meters in the East Greenland Current. In the Arctic, the negative anomaly also extends and reaches -6 meters. On a long time scale, no other robust response is simulated; other parts of the Arctic and also the Subpolar North Atlantic show no anomalies.

The following figures present the response of solid freshwater, that is, sea ice. Figure 5.13 shows time series of Arctic sea ice extent and volume. Considering sea ice extent shown on the top panels of the figure, there is a slight decrease in most of the years in the

cyclonic GS+ scenario: its anomalies range between +0.1 and -0.4 x 10⁶ km². The response in the anticyclonic GS- scenario is more robust. There is an increase of sea ice extent, reaching almost +0.4 x 10⁶ km² after 3 years, and then varying between +0.4 and +0.7 x 10⁶ km². The differences between the two scenarios are similar for sea ice volume as well. The GS+ scenario shows lower values than the GS- scenario, by 1000-1500 km³; however, the response is not that clear if it is compared to the control run. There are time periods where both perturbed runs show an increase of Arctic sea ice volume, and periods where both show no change or a loss of sea ice.
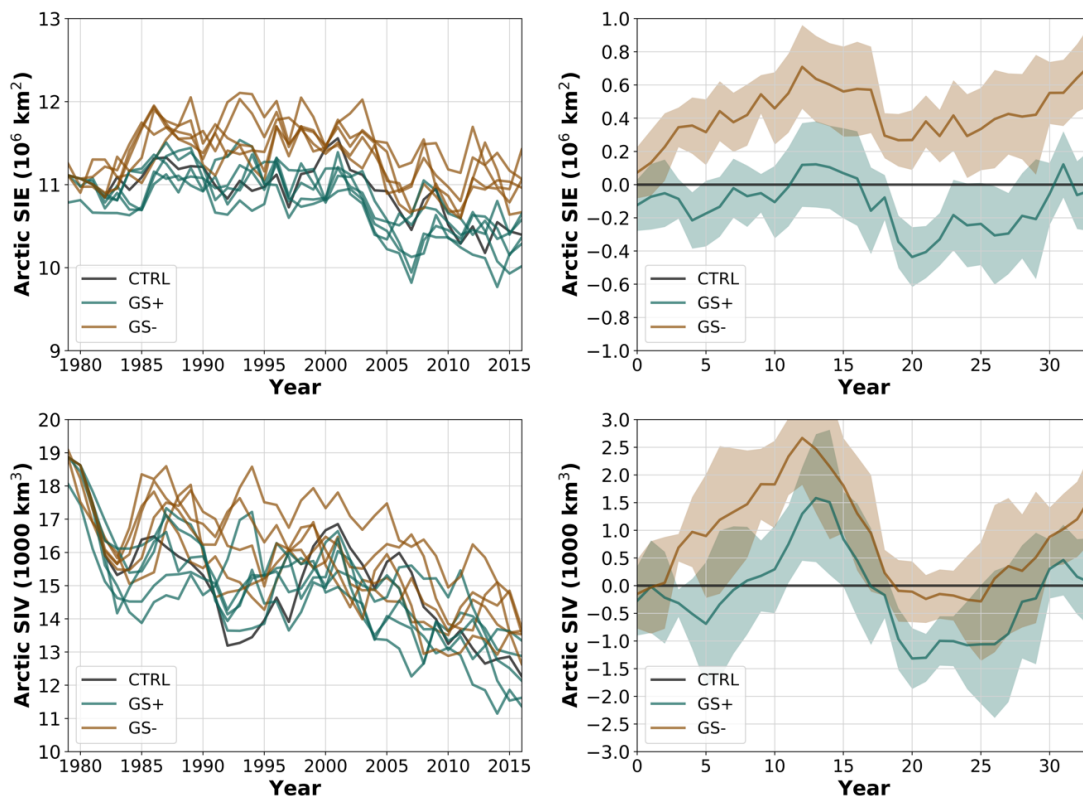

Figure 5.13. *Arctic sea ice extent (top) and volume (bottom) response to the GS wind perturbations as absolute values in the control run and members of the GS+ and GS- ensemble (left), and as anomalies in comparison with the control run (right), where the solid line indicates the mean, the shaded area indicates the standard deviation of five-five ensemble members.*

The spatial response of sea ice thickness is illustrated on Figure 5.14 that presents its anomalies after 3, 10, and 30 years following the perturbation of the winds associated with the Greenland Low. There is a robust response of sea ice thickness in the Greenland Sea and generally along the East Greenland Current, while other regions show no or not stable anomalies.

The top panels of Figure 5.14 depict changes in the cyclonic GS+ scenario. The wind forcing results in thinner ice in the Greenland Sea, where the anomaly reaches -0.3 meter after 3 years. There is also an anomaly of opposite sign just along the eastern shores of

Greenland. These changes become more apparent over time, as it can be seen on the top middle panel showing the response after 10 years. The thinning remains similar, and the thickening next to Greenland becomes stronger and a little more extended. Meanwhile there are smaller anomalies at higher latitudes in the Arctic, but these are not robust in time and partly can be explained by the large interannual variability of the model simulations. After 20 years the positive anomaly starts to diminish, and by year 30 it is barely visible, while the negative anomaly along the East Greenland Current extends both in space and in strength, exceeding -0.5 meter just south of Fram Strait.
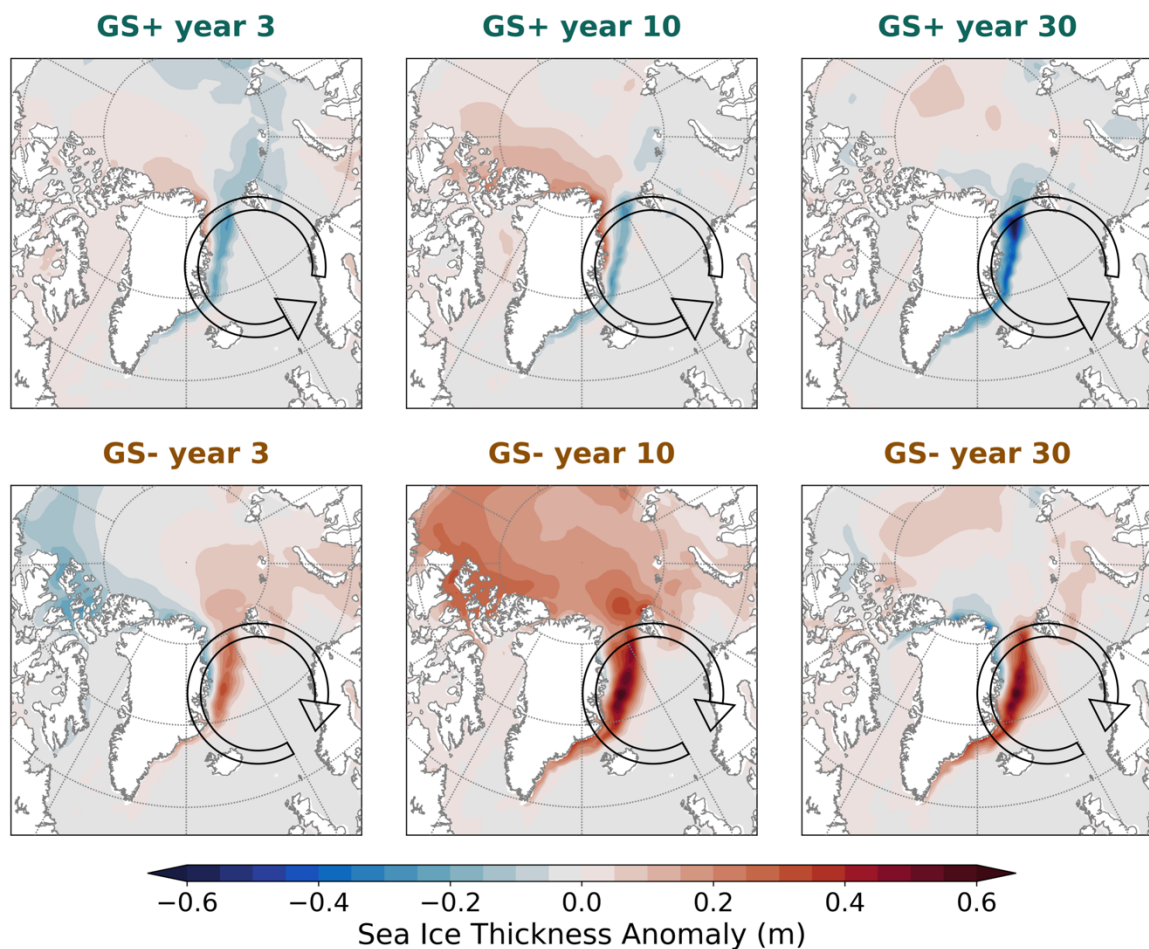

Figure 5.14. *Sea ice thickness response to the GS wind perturbations (black contours). The panels show the ensemble mean anomalies of the GS+ (top row) and the GS- (bottom row) scenarios in comparison with the control run as annual means of the 3rd (left), the 10th (middle), and the 30th (right) year following the step change in forcing.*

The response in the anticyclonic GS- scenario is roughly the opposite in the Nordic Seas. As seen on the bottom panels of Figure 5.14, there is a positive anomaly in the Greenland Sea, reaching +0.3 meter after 3 years, but close to the shores of Greenland the anomaly is negative. The latter remains more or less unchanged over time, but the positive anomaly strengthens considerably, exceeding 0.5 meter in some parts of the Greenland Sea after 10 years, and stabilizes around this value afterwards. Meanwhile, there are large

anomalies present also in the Arctic, but these are not as robust in time. In the first few years there is a decrease in ice thickness in the Canadian Arctic, but in the following years a strong positive anomaly develops almost everywhere in the Arctic, which is actually strongest around the Canadian Arctic Archipelago. A similar, but somewhat weaker positive anomaly is present in the GS+ simulations between years 10–18 (not shown). This then weakens in a few years, and then the years 20–28 are characterized by a negative anomaly in both scenarios (not shown). By year 30 this also reduces, and once again there is no significant anomaly visible in the Arctic, as seen on the right side panels of Figure 5.14. The temporal evolution of these changes can clearly be followed on the time series of Arctic Ocean sea ice extent and especially volume on Figure 5.13.
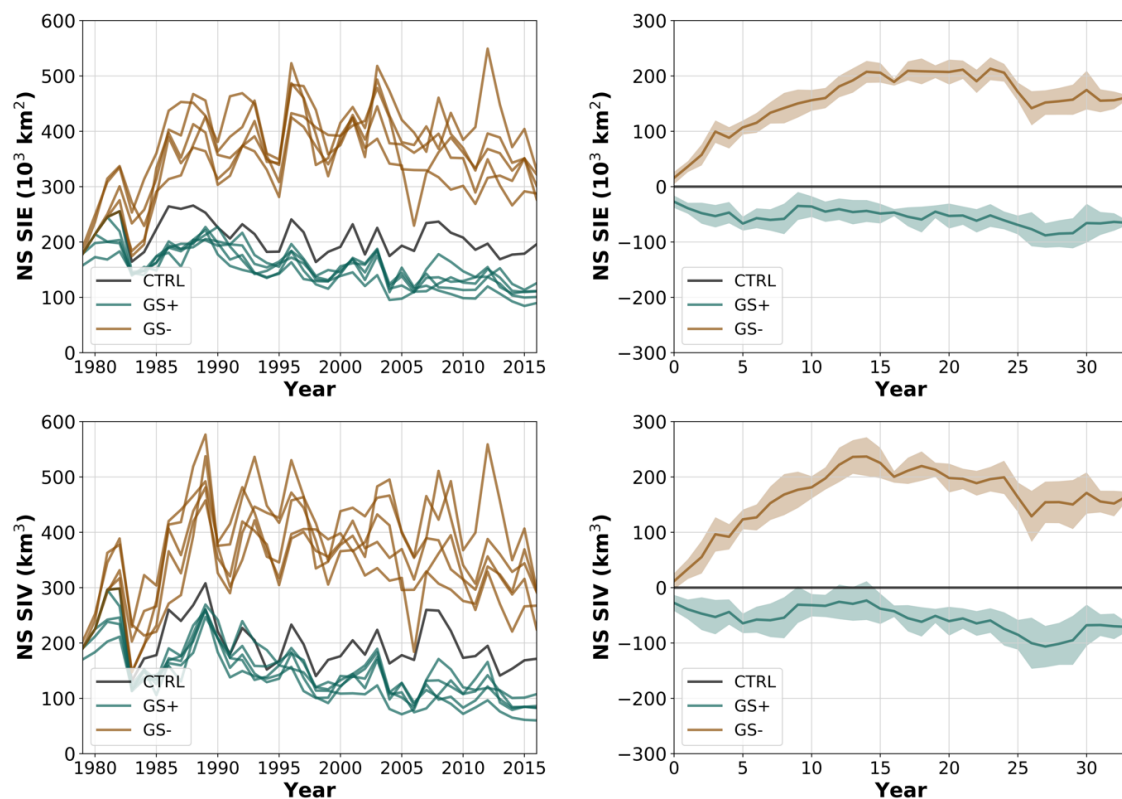

Figure 5.15. *Nordic Seas sea ice extent (top) and volume (bottom) response to the GS wind perturbations as absolute values in the control run and members of the GS+ and GS- ensemble (left), and as anomalies in comparison with the control run (right), where the solid line indicates the mean, the shaded area indicates the standard deviation of five-five ensemble members.*

As the only robust sea ice response is observed in the Nordic Seas, its development is examined in more detail on Figure 5.15, which presents the time series of its regional sea ice extent and volume. The response is similar for both measures. There is a smaller decrease in the cyclonic GS+ scenario, and a much larger increase in the anticyclonic GS-scenario that develops gradually over 10–15 years, and remains mostly stable afterwards. Considering the Nordic Seas ice extent, its mean values are about 200,000 km^2 in the control run, and range between 170,000 and 270,000 km^2. The GS+ response is

around -50,000 km², which translates to a decrease of approximately 25% from the mean. The GS- response reaches twice this size already after 3 years, and stabilizes between +150,000 and +200,000 km² after 10 years. This means a 100% increase in the Nordic Seas ice extent. The changes are very similar for the ice volume as well, which has a mean value of 200 km³, and ranges between 130 and 300 km³ in the control simulation. The decrease in the GS+ scenario is about -50 km³, and the increase in the GS- scenario reaches +100 km³ after 3 years, and stabilizes between +140 and +230 km³. The Nordic Seas ice volume thus also doubles as a response to the anticyclonic wind forcing anomaly. These local responses are rather robust in time, and also show a relatively small ensemble variability.

5.4.   Discussion

The model simulations show well pronounced responses to the applied wind forcing perturbations that help explaining the physical processes behind certain modes of atmosphere-driven freshwater variability identified in the previous chapter.

The results of the BG perturbations confirm the tight link between the strength of the anticyclonic winds associated with the Beaufort High, and the strength of the Beaufort Gyre. The applied wind perturbations lead to an inflation of the gyre in case of stronger anticyclonic winds, while a cyclonic wind anomaly results in its weakening. Although the perturbations are associated with a sea-level pressure anomaly of 4 hPa that is not unrealistic (Marshall et al., 2017), they are strong enough to alter not only the surface currents, but the entire vertical structure of the gyre. The cyclonic wind perturbations result in an inverted gyre structure with doming isopycnals and a cyclonic circulation.

The most striking response to the BG perturbations is the liquid freshwater anomalies centered in the Beaufort Gyre. The extent and the size of these anomalies are similar to those derived from the fully coupled experiments by the redundancy analysis of the previous chapter. That analysis suggested a liquid freshwater response of up to 1 meter to a persistent sea-level pressure change of 1 hPa. Here the response to the wind perturbations associated with a 4 hPa anomaly result in changes of about 3 meters after three years of continuous forcing, and about 7 meters after ten years. The response is not symmetric; it is somewhat stronger in the anticyclonic BG+ scenario, and weaker in the cyclonic BG- scenario. Overall, the response is very similar to what Marshall et al. (2017) reported to the same forcing perturbations in their reanalysis-forced ocean model.

The primary mechanism behind the response is wind-driven Ekman dynamics. A positive wind stress curl in the anticyclonic scenario leads to the convergence of the surface currents. Due to the resulting Ekman pumping inflating the gyre, which is balanced only by baroclinic instability (Manucharyan and Spall, 2016), there is an

accumulation of liquid freshwater. The surface divergence and Ekman suction leads to an opposite response in the cyclonic wind scenario. This simulated response is consistent with the theory of the wind-driven variability of the Beaufort Gyre (Manucharyan et al., 2016), that accumulates freshwater during a regime of anticyclonic winds, and releases it during a cyclonic regime (Proshutinsky et al., 2002).

The response of solid freshwater content to the BG wind perturbations is not as consistent compared to other results. Although its spatial structure is somewhat similar to its leading atmospheric-driven mode of variability based on the fully coupled experiments presented in the previous chapter, it is much weaker than that. The response here is about 0.2 meters after three years of forcing anomaly associated with a 4 hPa change, while the redundancy analysis suggested a response three times larger. However, the wind forcing perturbations applied here did not match the location of the driving patterns identified by the redundancy analysis, suggesting that the solid freshwater response varies greatly depending on the exact location of the forcing anomalies.

The total Arctic sea ice extent shows no response, similar to the results of Marshall et al. (2017), but unlike in their simulations, here the sea ice volume response is not clear. In the Modini-MPI-ESM simulation both scenarios show positive and negative sea ice volume anomalies as well, although the BG+ results are generally higher than the BG-results by 500–1,000 km^3. Still, a seesaw between the ice thickness in the Canadian and the Siberian Arctic is a robust response in time in the simulations presented here, and it can have implications to the accessibility of Arctic shipping routes, as it implies that an anticyclonic wind regime of the Arctic might favor the accessibility of the Northeast Passage with thinner ice in the shelf seas along its route, while a cyclonic regime is more likely to result in thinner is along the Northwest Passage.

The results of the BG scenarios show that a switch to cyclonic winds over the Beaufort Gyre leads to the release of its accumulated liquid freshwater into the Arctic Ocean, consistent with previous studies (Giles et al., 2012; Stewart and Haine, 2013). However, the results show no response outside of the Arctic Ocean. Considering that these scenarios were constructed by perturbing the wind field only locally, this implies that the redistribution of freshwater between the Arctic Ocean and the Subarctic North Atlantic is governed by a combination of different wind forcing patterns. This agrees with observations that suggest that the possible accumulation of freshwater in the Beaufort Gyre depends on the strength of the Beaufort High, but the availability of freshwater depends on the AO that can route it into the Amerasian Basin, or across the Arctic towards the North Atlantic (Mauritzen, 2012; Morison et al., 2012). The results of the redundancy analysis of the previous chapter also identified different modes of atmosphere-driven freshwater anomalies, and linked the North Atlantic anomalies to an atmospheric forcing pattern similar to the NAO. The northern center of action of this pattern, situated over the

Nordic Seas, is likely to play a key role in modulating the freshwater export from the Arctic (Horn, 2018). This was investigated here by perturbing the wind forcing over the Greenland Sea, following Marshall et al. (2017).

The perturbed wind field over the Greenland Sea causes freshwater anomalies in the Nordic Seas that anticorrelate with the strength of the cyclonicity both for the liquid and for the solid component. This response is asymmetric, as the freshwater anomalies are much larger in the anticyclonic GS- scenario, and more robust for the solid component. This asymmetry might be partly due to the fact that Greenland Sea ice extent is underestimated in the model (Jungclaus et al., 2006), and the ice edge thus has more potential to extend east than to recede further west. The observed Greenland Sea ice extent responds stronger to negative NAO (locally similar to GS-) forcing than to positive (Germe et al., 2011).

As the changes in the Nordic Seas ice cover are formed several years before an anomaly develops in the Fram Strait ice export, they are locally formed, due to a wind-driven displacement of the export pathway. The cyclonic (anticyclonic) wind forcing anomalies push the ice closer to (further away from) Greenland, reducing (increasing) the ice extent in the Greenland Sea.

The sea ice and sea surface changes in the Greenland Sea are directly driven by the changes in wind forcing, and they agree with the results of forced ocean models using the same wind perturbations (Muilwijk et al., 2019). The simulated spin-up (spin-down) of the cyclonic circulation in the Nordic Seas due to an overlying cyclonic (anticyclonic) wind anomaly is also in agreement with the barotropic model of Isachsen et al. (2003), and within the range of the multi-model ensemble of Muilwijk et al. (2019). But unlike in other models in their comparison, the oceanic fluxes across the Barents Sea Opening do not show a well-defined change in Modini-MPI-ESM, and the barotropic response does not extend into the Arctic Ocean.

A reason for these differences can be that the configuration of the Modini-MPI-ESM allows for the atmosphere to actively react to the Nordic Seas surface changes directly driven by the wind. This enables the model to simulate ocean-air feedbacks that can obscure the linear response of other parameters to the wind forcing perturbations. An example of such a feedback is presented in Kovács et al. (under review). Due to this, the results presented here are mostly inconsistent with the response of other models in Muilwijk et al. (2019) outside of the Nordic Seas.

5.5. Conclusions

The objective of the work presented in this chapter was to investigate the effect of certain wind forcing anomalies on freshwater variability by performing model experiments with perturbed wind forcing. The experiments were designed based on Marshall et al. (2017), and on the results of the previous chapter of this study. A total of four forcing scenarios were constructed to simulate the effect of wind forcing perturbations associated with the strength of the high atmospheric pressure system over the Beaufort Gyre, and the strength of the low-pressure system over the Greenland Seas.

The results showed a robust freshwater response to the wind perturbations over the Beaufort Gyre. According to the model results, stronger anticyclonic winds inflate the Beaufort Gyre due to Ekman dynamics. The inflated gyre can store more liquid freshwater, while in other parts of the Arctic Ocean there is a decrease of freshwater content. There is an almost symmetrical response to a cyclonic wind anomaly that deflates the gyre, causing it to release a large part of its liquid freshwater. This simulated wind-driven redistribution of Arctic liquid freshwater content confirms the leading redundancy mode of atmosphere-freshwater covariability identified by the statistical analysis in the previous chapter, and is consistent with theory (Proshutinsky et al., 2002; Manucharyan et al., 2016) and with the response simulated by Marshall et al. (2017).

The wind perturbations over the Beaufort Gyre influence Arctic sea ice distribution as well: an anticyclonic wind anomaly increases sea ice thickness in the Canadian Arctic, and decreases it along the Siberian coast, while a cyclonic wind anomaly has an opposite effect. This wind-driven seesaw may have implications on the accessibility of the Northeast and Northwest Passages, suggesting that the local atmospheric circulation over the Amerasian Basin might favor the accessibility of one against the other.

The freshwater response to wind anomalies over the Greenland Sea is mostly unclear, and does not confirm the results of the previous chapter that showed a link between an atmospheric dipole pattern and the liquid freshwater content of the Subpolar North Atlantic Ocean. The absence of this freshwater response is likely due to experiment design: the wind field was perturbed only near the northern center of action of the previously identified pattern of atmospheric variability. This suggests that the North Atlantic freshwater anomalies are likely driven by the wind changes associated with the interaction of both centers of action resembling the NAO.

A number of different forced ocean models with the same wind forcing anomalies over the Greenland Sea show robust anomalies in the heat transported northward by Atlantic Water, influencing Arctic circulation and sea ice cover (Muilwijk et al., 2019). However, the results presented here are inconsistent with their findings, and show no robust response in the Arctic Ocean either. Therefore it is also likely that the local wind-

induced changes in surface conditions introduce ocean-air feedbacks that are not simulated by forced ocean models, but are simulated by the partially coupled configuration of Modini-MPI-ESM. This obscures the linear response to the wind perturbations, and makes this experiment unsuitable for the evaluation of Arctic-Subarctic freshwater covariability. But within the Nordic Seas, the results are consistent with the response in other models analyzed by Muilwijk et al. (2019), and show a significant increase (decrease) of sea ice extent and volume in case of an anticyclonic (cyclonic) wind anomaly over the Greenland Sea.

The results of the targeted wind perturbation experiments confirmed the key role of the local atmospheric circulation over the Beaufort Gyre in modulating the spatial distribution of liquid freshwater content in the Arctic Ocean. The experiments showed that a change from an anticyclonic to a cyclonic regime releases freshwater accumulated in the gyre, but this local circulation change itself does not result in the export of this anomaly to the Subarctic North Atlantic. The export is hypothesized to be driven by the interaction of these circulation regimes and the circulation over the Nordic Seas, but the effect of the latter could not be evaluated, due to the inconsistencies of the response.

6. Summary and Outlook

The aim of this study was to examine the hypothesized link between Arctic and North Atlantic salinity anomalies, expressed as changes in their freshwater content, and to investigate the role of wind stress forcing in driving these changes. This was done by performing numerical experiments with different coupling configurations of the global Max Planck Institute Earth System Model (MPI-ESM), and by analyzing oceanic and atmospheric variability in the model output.

As the currently available measurements still do not cover a long enough time, and are often incomplete, numerical model simulations provide the only way to analyze the Arctic and the Subarctic North Atlantic (comprising the Subpolar North Atlantic Ocean and the Nordic Seas) freshwater covariability over a centennial time period. The model results presented in this study show repeating large freshwater content anomalies in both domains that are often comparable in size, but rarely in timing, suggesting a rather unstable relationship. This is unexpected, because in the same simulations, the anomalies in both basins are driven by changes in the oceanic lateral fluxes across sections bordering them. As the two domains share most of their borders, an Arctic freshwater content anomaly is expected to be balanced by an anomaly of opposite sign in the Subarctic North Atlantic, as indeed seen in observations from recent decades. The analysis presented here revealed the reason why this opposing variability is not persistent enough to result in a stable anticorrelation over a time scale longer than a few decades: the sign of freshwater redistribution between the two domains is actually very stable, but most of the time it is obscured by large anomalies in the North Atlantic that are advected from the south, and are not directly related to the freshwater exchange with the Arctic Ocean. This suggests that the observed anticorrelation is not likely to persist in the future, but episodic periods with a seesaw of Arctic-Subarctic freshwater content will possibly occur again even if most of the sea ice disappears, as their link is dominated by the exchange of liquid freshwater.

Comparing model results from two different configurations of MPI-ESM showed that the freshwater anomalies are driven mainly by wind stress forcing. The simulated Arctic and North Atlantic freshwater anomalies had similar amplitudes in all members of the fully coupled ensemble, but their timing was not synchronized, as each of these unconstrained simulations were in a different state of their internal variability. Repeating the simulations with constrained wind forcing by using prescribed wind data based on observations yielded different results: the ensemble variability was greatly reduced, and all members could similarly reproduce the timing of the observed freshwater anomalies

of the 1990s, even though these runs were identical to the unconstrained fully coupled runs, except for their wind forcing. This confirmed the fundamental role of wind stress forcing, but did not explain how does it shape the freshwater distribution between the Arctic and the Subarctic North Atlantic. The next step was therefore to analyze the covariability of freshwater content and atmospheric circulation.

A comprehensive statistical analysis showed that the basin-scale freshwater anomalies are the combined results of different components of liquid and solid freshwater variability. These have different sizes and time scales, and can be linked to different patterns of atmospheric variability. A key result of this study is that although the Arctic Oscillation (AO) or the North Atlantic Oscillation (NAO) describe the main statistical modes of large-scale atmospheric variability, they do not represent those modes that are best connected to the freshwater anomalies in the Arctic Ocean and in the Subarctic North Atlantic. Instead, a tripole atmospheric mode with one center of action over the central Arctic was found to be connected to large liquid freshwater anomalies in the Arctic Ocean, and another mode reminiscent of (but not identical) to the NAO was found to be the driver of anomalies in the Subpolar North Atlantic Ocean. These two anomaly patterns describe about a third of the total liquid freshwater variability. The major modes of solid freshwater variability show a redistribution between opposing shelves of the Arctic Ocean, primarily driven by atmospheric patterns local to the Arctic.

The identified modes of atmospheric circulation and freshwater variability suggest that the Arctic-Subarctic freshwater variability is dominated by the redistribution of the liquid component, driven by different atmospheric circulation regimes. During times when these regimes are in opposing phases, there is a higher potential for an anticorrelation between the freshwater content of the Arctic Ocean and the Subarctic North Atlantic.

For the freshwater anomalies in the Arctic Ocean, the most important wind regime is situated over the Beaufort Gyre, regulating its strength. Additional model simulations constructed by perturbing this wind regime showed that during an anticyclonic regime the gyre inflates and accumulates freshwater due to Ekman dynamics, and releases it when the wind switches to a cyclonic regime. This explains the main mode of freshwater variability within the Arctic Ocean, consistent with previous studies and with the results of the statistical analysis as well. Changes in this wind regime were found to redistribute sea ice between the Canadian and the Siberian Arctic, suggesting that the accessibility of either the Northeast or Northwest Passage may be favored against the other, depending on the prevailing wind regime over the Amerasian Basin. However, no significant response to changes in the circulation over the Beaufort Gyre was found outside of the Arctic Ocean. This suggests that this regime influences the amount of freshwater available

for export to the Subarctic North Atlantic, but it does not control the export itself, and is therefore not a direct driver of North Atlantic freshwater anomalies.

Freshwater anomalies in the Subarctic North Atlantic were found to be driven by wind forcing associated with an atmospheric pressure dipole between the area of the Nordic Seas and the western North Atlantic around 45°N. From these two centers of action, the atmospheric circulation over the Nordic Seas was hypothesized to play a key role in regulating the Arctic freshwater export due to its proximity to the main export pathways. Therefore, additional experiments were designed by perturbing the wind regime over the Greenland Sea. The results showed that an anomalous cyclonic or anticyclonic perturbation causes significant freshwater anomalies in the Nordic Seas. The increase of sea ice extent and volume in case of an anticyclonic wind anomaly was particularly robust. But the linear response outside of the Nordic Seas was obscured by the effect of ocean-air feedbacks simulated by the partially coupled model configuration. Because of this, this last experiment was found to be unsuitable for evaluating the response of Arctic-Subarctic freshwater covariability to changes in wind forcing over the Greenland Sea.

The results of this work demonstrated that in order to study the salinity anomalies in the Arctic Ocean and in the Subarctic North Atlantic, regular observations are needed in both domains, but the continuous monitoring of the fluxes between them is equally important. Sufficiently long and high quality measurements are essential in order to understand the formation and propagation of these anomalies.

Based on the characteristic time scale of the observed freshwater anomalies and on the high level of internal variability in the atmosphere-freshwater system, the currently available measurement history is still too short, and cannot be used to properly assess the robustness of the opposing freshwater variability observed in recent decades between the Arctic and the Subarctic North Atlantic. Coupled model simulations with a dynamic atmosphere can provide sufficiently long time series of both freshwater and atmospheric circulation. Due to the key role of wind stress forcing, the proper representation of cross boundary fluxes is very important in these models; not only the simulations of air-ocean momentum exchange, but of moisture and heat as well.

This work has answered several questions regarding freshwater covariability and wind forcing; however, much more can be done even by just applying the same tools as used here. This study focused on basin-scale freshwater anomalies, but it would be interesting to analyze the propagation of anomalies, and the link of different pathways to different atmospheric forcing conditions. Extending the analysis using simulations stretching until the end of the 21st century could provide useful insights on how the freshwater variability is expected to change under a rapidly changing Arctic climate.

It could also be interesting to analyze the oceanic response to further scenarios of wind forcing anomalies, positioned for example over the Barents Sea, and to evaluate their effect on the flow of Atlantic Water and the resulting changes in the Arctic Ocean. More complex scenarios with a fluctuating sign of wind anomalies over the Beaufort Gyre could provide additional insights to the accumulation and release of freshwater. The perturbation of multiple centers would be particularly interesting, for example to prescribe simultaneous changes in the wind field over the Beaufort Gyre and over the Nordic Seas, to investigate the effects of their coordinated changes. The influence of wind forcing associated with the changes of the NAO could be evaluated by perturbing the winds associated with both the Icelandic Low and the Azores High. Alternatively, a wind forcing anomaly could be created based on the full field of the NAO pattern.

The partially coupled configuration of the Modini method allows the representation of ocean-air feedbacks, and thus can provide an opportunity to investigate the indirect atmospheric response to wind-induced changes in sea surface conditions. An example of a possible wind feedback mediated by sea ice in the Nordic Seas is presented in Kovács et al. (under review). Further analysis of the model results from the Greenland Sea wind perturbations revealed that the ice edge in the Greenland Sea extends eastwards due to local southerly winds associated with an overlying anticyclonic forcing anomaly. This leads to the stabilization of the marine atmospheric boundary layer over newly ice-covered waters due to reduced ocean-atmosphere heat fluxes. The spatial pattern of the resulting sea-level pressure changes is so that it generates geostrophic winds that are locally comparable to the initially applied forcing, suggesting a positive feedback (Kovács et al., under review). Future experiments focusing on the indirect atmospheric response to wind-induced changes in sea surface conditions could provide useful insights on atmosphere-ocean coupling on different time and spatial scales in other regions as well.

The Modini method was developed also for the higher resolution configuration of the MPI-ESM, which can provide a better representation of atmospheric processes, that could be beneficial for the simulation of a wind feedback. The Modini method could be adapted to other coupled models as well, in order to broaden its applicability.

Bibliography

Aagaard, K., and E. C. Carmack, 1989: The Role of Sea Ice and Other Fresh-Water in the Arctic Circulation, Journal of Geophysical Research: Oceans, 94 (C10), 14485-14498, doi:10.1029/JC094iC10p14485.

Aagaard, K., J. H. Swift, and E. C. Carmack, 1985: Thermohaline circulation in the Arctic Mediterranean Seas, Journal of Geophysical Research: Oceans, 90 (C3), 4833-4846, doi:10.1029/JC090iC03p04833.

Aksenov, Y., M. Karcher, A. Proshutinsky, R. Gerdes, B. de Cuevas, E. Golubeva, F. Kauker, A. T. Nguyen, G. A. Platov, M. Wadley, E. Watanabe, A. C. Coward, and A. J. G. Nurser, 2016: Arctic pathways of Pacific Water: Arctic Ocean Model Intercomparison experiments, Journal of Geophysical Research: Oceans, 121 (1), 27-59, doi:10.1002/2015JC011299.

Amante, C., and B. W. Eakins, 2009: ETOPO1 arc-minute global relief model: procedures, data sources and analysis, NOAA Technical Memorandum. National Oceanic and Atmospheric Administration, doi:10.7289/V5C8276M.

Ambaum, M. H. P., B. J. Hoskins, and D. B. Stephenson, 2001: Arctic oscillation or North Atlantic oscillation?, Journal of Climate, 14 (16), 3495-3507, doi:10.1175/1520-0442(2001)014<3495:Aoonao>2.0.Co;2.

Bakalian, F., H. Ritchie, K. Thompson, and W. Merryfield, 2010: Exploring Atmosphere–Ocean Coupling Using Principal Component and Redundancy Analysis, Journal of Climate, 23 (18), 4926-4943, doi:10.1175/2010JCLI3388.1.

Barnston, A. G., and R. E. Livezey, 1987: Classification, Seasonality and Persistence of Low-Frequency Atmospheric Circulation Patterns, Monthly Weather Review, 115 (6), 1083-1126, doi:10.1175/1520-0493(1987)115<1083:Csapol>2.0.Co;2.

Belkin, I. M., 2004: Propagation of the "Great Salinity Anomaly" of the 1990s around the northern North Atlantic, Geophysical Research Letters, 31 (8), doi:10.1029/2003gl019334.

Belkin, I. M., S. Levitus, J. Antonov, and S. A. Malmberg, 1998: "Great Salinity Anomalies" in the North Atlantic, Progress in Oceanography, 41 (1), 1-68, doi:10.1016/S0079-6611(98)00015-9.

Bersch, M., I. Yashayaev, and K. P. Koltermann, 2007: Recent changes of the thermohaline circulation in the subpolar North Atlantic, Ocean Dynamics, 57 (3), 223-235, doi:10.1007/s10236-007-0104-7.

Beszczynska-Möller, A., E. Fahrbach, U. Schauer, and E. Hansen, 2012: Variability in Atlantic water temperature and transport at the entrance to the Arctic Ocean, 1997–2010, ICES Journal of Marine Science, 69 (5), 852-863, doi:10.1093/icesjms/fss056.

Blindheim, J., and S. Østerhus, 2005: The Nordic Seas, Main Oceanographic Features, The Nordic Seas: An Integrated Perspective, 11-37, doi:10.1029/158GM03.

Boyer, T., S. Levitus, J. Antonov, R. Locarnini, A. Mishonov, H. Garcia, and S. A. Josey, 2007: Changes in freshwater content in the North Atlantic Ocean 1955-2006, Geophysical Research Letters, 34 (16), doi:10.1029/2007gl030126.

Carmack, E. C., M. Yamamoto-Kawai, T. W. N. Haine, S. Bacon, B. A. Bluhm, C. Lique, H. Melling, I. V. Polyakov, F. Straneo, M. L. Timmermans, and W. J. Williams, 2016: Freshwater and its role in the Arctic Marine System: Sources, disposition, storage, export, and physical and biogeochemical consequences in the Arctic and global oceans, Journal of Geophysical Research: Biogeosciences, 121 (3), 675-717, doi:10.1002/2015jg003140.

Condron, A., P. Winsor, C. Hill, and D. Menemenlis, 2009: Simulated Response of the Arctic Freshwater Budget to Extreme NAO Wind Forcing, Journal of Climate, 22 (9), 2422-2437, doi:10.1175/2008jcli2626.1.

Cox, G. F. N., and W. F. Weeks, 1974: Salinity Variations in Sea Ice, Journal of Glaciology, 13 (67), 109-120, doi:10.3189/S0022143000023418.

Curry, B., C. M. Lee, and B. Petrie, 2011: Volume, Freshwater, and Heat Fluxes through Davis Strait, 2004-05, Journal of Physical Oceanography, 41 (3), 429-436, doi:10.1175/2010jpo4536.1.

Curry, B., C. M. Lee, B. Petrie, R. E. Moritz, and R. Kwok, 2014: Multiyear Volume, Liquid Freshwater, and Sea Ice Transports through Davis Strait, 2004-10*, Journal of Physical Oceanography, 44 (4), 1244-1266, doi:10.1175/Jpo-D-13-0177.1.

Curry, R. G., and C. Mauritzen, 2005: Dilution of the Northern North Atlantic Ocean in Recent Decades, Science, 308 (5729), 1772-1774, doi:10.1126/science.1109477.

Curry, R. G., and M. S. McCartney, 2001: Ocean gyre circulation changes associated with the North Atlantic Oscillation, Journal of Physical Oceanography, 31 (12), 3374-3400, doi:10.1175/1520-0485(2001)031<3374:Ogccaw>2.0.Co;2.

Davini, P., and C. Cagnazzo, 2014: On the misinterpretation of the North Atlantic Oscillation in CMIP5 models, Climate Dynamics, 43 (5), 1497-1511, doi:10.1007/s00382-013-1970-y.

Davini, P., C. Cagnazzo, R. Neale, and J. Tribbia, 2012: Coupling between Greenland blocking and the North Atlantic Oscillation pattern, Geophysical Research Letters, 39, doi:10.1029/2012gl052315.

Deser, C., 2000: On the teleconnectivity of the "Arctic Oscillation", Geophysical Research Letters, 27 (6), 779-782, doi:10.1029/1999GL010945.

Deshayes, J., R. Curry, and R. Msadek, 2014: CMIP5 Model Intercomparison of Freshwater Budget and Circulation in the North Atlantic, Journal of Climate, 27 (9), 3298-3317, doi:10.1175/Jcli-D-12-00700.1.

Dickson, R., J. Lazier, J. Meincke, P. Rhines, and J. Swift, 1996: Long-term coordinated changes in the convective activity of the North Atlantic, Progress in Oceanography, 38 (3), 241-295, doi:10.1016/S0079-6611(97)00002-5.

Dickson, R., J. Meincke, S. A. Malmberg, and A. J. Lee, 1988: The Great Salinity Anomaly in the Northern North-Atlantic 1968-1982, Progress in Oceanography, 20 (2), 103-151, doi:10.1016/0079-6611(88)90049-3.

Dickson, R., T. J. Osborn, J. W. Hurrell, J. Meincke, J. Blindheim, B. Adlandsvik, T. Vinje, G. Alekseev, and W. Maslowski, 2000: The Arctic Ocean response to the North Atlantic oscillation, Journal of Climate, 13 (15), 2671-2696, doi:10.1175/1520-0442(2000)013<2671:Taortt>2.0.Co;2.

Dickson, R., B. Rudels, S. Dye, M. Karcher, J. Meincke, and I. Yashayaev, 2007: Current estimates of freshwater flux through Arctic and subarctic seas, Progress in Oceanography, 73 (3–4), 210-230, doi:10.1016/j.pocean.2006.12.003.

Ding, Y. N., J. A. Carton, G. A. Chepurin, M. Steele, and S. Hakkinen, 2016: Seasonal heat and freshwater cycles in the Arctic Ocean in CMIP5 coupled models, Journal of Geophysical Research: Oceans, 121 (4), 2043-2057, doi:10.1002/2015jc011124.

Drange, H., T. Dokken, T. Furevik, R. Gerdes, W. Berger, A. Nesje, K. Arild Orvik, Ø. Skagseth, I. Skjelvan, and S. Østerhus, 2005: The Nordic Seas: An Overview, The Nordic Seas: An Integrated Perspective, 1-10, doi:10.1029/158GM02.

Ekman, V. W., 1905: On the influence of earth's rotation on ocean currents, Arkiv för Matematik, Astronomi och Fysik, 2, 1-53.

Environmental Working Group (EWG), 1997: Joint U.S.-Russian Atlas of the Arctic Ocean for the Winter Period. National Snow and Ice Data Center, CD-ROM.

Environmental Working Group (EWG), 1998: Joint U.S.-Russian Atlas of the Arctic Ocean for the Summer Period. National Snow and Ice Data Center, CD-ROM.

Fichot, C. G., K. Kaiser, S. B. Hooker, R. M. W. Amon, M. Babin, S. Belanger, S. A. Walker, and R. Benner, 2013: Pan-Arctic distributions of continental runoff in the Arctic Ocean, Scientific Reports, 3, 1053, doi:10.1038/srep01053.

Fieg, K., R. Gerdes, E. Fahrbach, A. Beszczynska-Möller, and U. Schauer, 2010: Simulation of oceanic volume transports through Fram Strait 1995–2005, Ocean Dynamics, 60 (3), 491-502, doi:10.1007/s10236-010-0263-9.

Gerdes, R., M. Karcher, C. Köberle, and K. Fieg, 2008, Simulating the Long-Term Variability of Liquid Freshwater Export from the Arctic Ocean, in Arctic–Subarctic Ocean Fluxes: Defining the Role of the Northern Seas in Climate, edited by R. R. Dickson, J. Meincke and P. Rhines, pp. 405-425, Springer Netherlands, Dordrecht, doi:10.1007/978-1-4020-6774-7_18.

Gerdes, R., and C. Koberle, 1999: Numerical simulation of salinity anomaly propagation in the Nordic seas and the Arctic Ocean, Polar Research, 18 (2), 159-166, doi:10.1111/j.1751-8369.1999.tb00288.x.

Germe, A., M.-N. Houssais, C. Herbaut, and C. Cassou, 2011: Greenland Sea sea ice variability over 1979–2007 and its link to the surface atmosphere, Journal of Geophysical Research: Oceans, 116 (C10), doi:10.1029/2011JC006960.

Giles, K. A., S. W. Laxon, A. L. Ridout, D. J. Wingham, and S. Bacon, 2012: Western Arctic Ocean freshwater storage increased by wind-driven spin-up of the Beaufort Gyre, Nature Geoscience, 5 (3), 194-197, doi:10.1038/Ngeo1379.

Greatbatch, R. J., 2000: The North Atlantic Oscillation, Stochastic Environmental Research and Risk Assessment, 14 (4-5), 213-242, doi:10.1007/S004770000047.

Gregor, D., H. Loeng, and L. Barrie, 1998: The influence of physical and chemical processes on contaminant transport into and within the Arctic. In: AMAP Assessment Report: Arctic Pollution Issues; Arctic Monitoring and Assessment Programme: Oslo, Norway; Chapter 3.

Grosfeld, K., R. Treffeisen, J. Asseng, A. Bartsch, B. Bräuer, B. Fritzsch, R. Gerdes, S. Hendricks, W. Hiller, and G. Heygster, 2016: Online sea-ice knowledge and data platform <www.meereisportal.de>, Polarforschung, 85 (2), 143-155.

Haak, H., J. Jungclaus, U. Mikolajewicz, and M. Latif, 2003: Formation and propagation of great salinity anomalies, Geophysical Research Letters, 30 (9), doi:10.1029/2003gl017065.

Hagemann, S., A. Loew, and A. Andersson, 2013: Combined evaluation of MPI-ESM land surface water and energy fluxes, Journal of Advances in Modeling Earth Systems, 5 (2), 259-286, doi:10.1029/2012MS000173.

Haine, T. W. N., B. Curry, R. Gerdes, E. Hansen, M. Karcher, C. Lee, B. Rudels, G. Spreen, L. de Steur, K. D. Stewart, and R. Woodgate, 2015: Arctic freshwater export: Status, mechanisms, and prospects, Global and Planetary Change, 125, 13-35, doi:10.1016/j.gloplacha.2014.11.013.

Häkkinen, S., 1993: An Arctic Source for the Great Salinity Anomaly - a Simulation of the Arctic Ice-Ocean System for 1955-1975, Journal of Geophysical Research: Oceans, 98 (C9), 16397-16410, doi:10.1029/93jc01504.

Häkkinen, S., and C. A. Geiger, 2000: Simulated low-frequency modes of circulation in the Arctic Ocean, Journal of Geophysical Research: Oceans, 105 (C3), 6549-6564, doi:10.1029/2000JC900003.

Häkkinen, S., and A. Proshutinsky, 2004: Freshwater content variability in the Arctic Ocean, Journal of Geophysical Research: Oceans, 109 (C3), doi:10.1029/2003jc001940.

Hansen, B., and S. Østerhus, 2000: North Atlantic–Nordic Seas exchanges, Progress in Oceanography, 45 (2), 109-208, doi:10.1016/S0079-6611(99)00052-X.

Hibler, W. D., 1979: Dynamic Thermodynamic Sea Ice Model, Journal of Physical Oceanography, 9 (4), 815-846, doi:10.1175/1520-0485(1979)009<0815:Adtsim>2.0.Co;2.

Hilmer, M., and T. Jung, 2000: Evidence for a recent change in the link between the North Atlantic Oscillation and Arctic sea ice export, Geophysical Research Letters, 27 (7), 989-992, doi:10.1029/1999gl010944.

Holfort, J., and J. Meincke, 2005: Time series of freshwater-transport on the East Greenland Shelf at 74°N, Meteorologische Zeitschrift, 14 (6), 703-710, doi:10.1127/0941-2948/2005/0079.

Horn, M. (2018), Freshwater variability in the Arctic Ocean and subarctic North Atlantic, Ph.D. thesis, Universität Bremen.

Houssais, M. N., C. Herbaut, P. Schlichtholz, and C. Rousset, 2007: Arctic salinity anomalies and their link to the North Atlantic during a positive phase of the Arctic Oscillation, Progress in Oceanography, 73 (2), 160-189, doi:10.1016/j.pocean.2007.02.005.

Hunkins, K., 1966: Ekman drift currents in the Arctic Ocean, Deep Sea Research and Oceanographic Abstracts, 13 (4), 607-620, doi:10.1016/0011-7471(66)90592-4.

Hurrell, J. W., 1995: Decadal Trends in the North-Atlantic Oscillation - Regional Temperatures and Precipitation, Science, 269 (5224), 676-679, doi:10.1126/Science.269.5224.676.

Hurrell, J. W., Y. Kushnir, G. Ottersen, and M. Visbeck, 2003, An Overview of the North Atlantic Oscillation, In: The North Atlantic Oscillation: Climatic Significance and Environmental Impact, pp. 1-35, American Geophysical Union, Washington, DC, doi:10.1029/134GM01.

Huth, R., 2007: Arctic or North Atlantic Oscillation? Arguments based on the principal component analysis methodology, Theoretical and Applied Climatology, 89 (1-2), 1-8, doi:10.1007/s00704-006-0257-1.

IHO (2002), International Hydrographic Organization: S-23 'Limits of Oceans and Seas', draft 4th version.

Ionita, M., P. Scholz, G. Lohmann, M. Dima, and M. Prange, 2016: Linkages between atmospheric blocking, sea ice export through Fram Strait and the Atlantic Meridional Overturning Circulation, Scientific Reports, 6, doi:10.1038/srep32881.

Isachsen, P. E., J. H. LaCasce, C. Mauritzen, and S. Häkkinen, 2003: Wind-Driven Variability of the Large-Scale Recirculating Flow in the Nordic Seas and Arctic Ocean, Journal of Physical Oceanography, 33 (12), 2534-2550, doi:10.1175/1520-0485(2003)033<2534:WVOTLR>2.0.CO;2.

Jahn, A., B. Tremblay, L. A. Mysak, and R. Newton, 2010: Effect of the large-scale atmospheric circulation on the variability of the Arctic Ocean freshwater export, Climate Dynamics, 34 (2-3), 201-222, doi:10.1007/s00382-009-0558-z.

Johnson, H., C. S. B., Y. Kostov, E. Beer, and C. Lique, 2018: Arctic Ocean Freshwater Content and Its Decadal Memory of Sea-Level Pressure, Geophysical Research Letters, 45 (10), 4991-5001, doi:10.1029/2017GL076870.

Jones, E. P., 2001: Circulation in the Arctic Ocean, Polar Research, 20 (2), 139-146, doi:10.1111/j.1751-8369.2001.tb00049.x.

Jungclaus, J. H., N. Fischer, H. Haak, K. Lohmann, J. Marotzke, D. Matei, U. Mikolajewicz, D. Notz, and J. S. von Storch, 2013: Characteristics of the ocean simulations in the Max Planck Institute Ocean Model (MPIOM) the ocean component of the MPI-Earth system

model, Journal of Advances in Modeling Earth Systems, 5 (2), 422-446, doi:10.1002/jame.20023.

Jungclaus, J. H., N. Keenlyside, M. Botzet, H. Haak, J. J. Luo, M. Latif, J. Marotzke, U. Mikolajewicz, and E. Roeckner, 2006: Ocean Circulation and Tropical Variability in the Coupled Model ECHAM5/MPI-OM, Journal of Climate, 19 (16), 3952-3972, doi:10.1175/JCLI3827.1.

Jungclaus, J. H., K. Lohmann, and D. Zanchettin, 2014: Enhanced 20th-century heat transfer to the Arctic simulated in the context of climate variations over the last millennium, Climate of the Past, 10 (6), 2201-2213, doi:10.5194/cp-10-2201-2014.

Karcher, M., R. Gerdes, F. Kauker, C. Koberle, and I. Yashayaev, 2005: Arctic Ocean change heralds North Atlantic freshening, Geophysical Research Letters, 32 (21), doi:10.1029/2005gl023861.

Kauker, F., and H. E. M. Meier, 2003: Modeling decadal variability of the Baltic Sea: 1. Reconstructing atmospheric surface data for the period 1902–1998, Journal of Geophysical Research: Oceans, 108 (C8), doi:10.1029/2003JC001797.

Köberle, C., and R. Gerdes, 2003: Mechanisms Determining the Variability of Arctic Sea Ice Conditions and Export, Journal of Climate, 16 (17), 2843-2858, doi:10.1175/1520-0442(2003)016<2843:MDTVOA>2.0.CO;2.

Koenigk, T., U. Mikolajewicz, H. Haak, and J. Jungclaus, 2006: Variability of Fram Strait sea ice export: causes, impacts and feedbacks in a coupled climate model, Climate Dynamics, 26 (1), 17-34, doi:10.1007/s00382-005-0060-1.

Koenigk, T., U. Mikolajewicz, J. H. Jungclaus, and A. Kroll, 2009: Sea ice in the Barents Sea: seasonal to interannual variability and climate feedbacks in a global coupled model, Climate Dynamics, 32 (7-8), 1119-1138, doi:10.1007/s00382-008-0450-2.

Kovács, T., R. Gerdes, J. Marshall: Wind feedback mediated by sea ice in the Nordic Seas, manuscript under review at the Journal of Climate.

Kushnir, Y., 1994: Interdecadal Variations in North-Atlantic Sea-Surface Temperature and Associated Atmospheric Conditions, Journal of Climate, 7 (1), 141-157, doi:10.1175/1520-0442(1994)007<0141:Ivinas>2.0.Co;2.

Kwok, R., 2000: Recent changes in Arctic Ocean sea ice motion associated with the North Atlantic Oscillation, Geophysical Research Letters, 27 (6), 775-778, doi:10.1029/1999gl002382.

Kwok, R., G. F. Cunningham, and S. S. Pang, 2004: Fram Strait sea ice outflow, Journal of Geophysical Research: Oceans, 109 (C1), doi:10.1029/2003jc001785.

Kwok, R., G. F. Cunningham, M. Wensnahan, I. Rigor, H. J. Zwally, and D. Yi, 2009: Thinning and volume loss of the Arctic Ocean sea ice cover: 2003–2008, Journal of Geophysical Research: Oceans, 114 (C7), doi:10.1029/2009JC005312.

Kwok, R., G. Spreen, and S. Pang, 2013: Arctic sea ice circulation and drift speed: Decadal trends and ocean currents, Journal of Geophysical Research: Oceans, 118 (5), 2408-2425, doi:10.1002/jgrc.20191.

Lique, C., M. M. Holland, Y. B. Dibike, D. M. Lawrence, and J. A. Screen, 2016: Modeling the Arctic freshwater system and its integration in the global system: Lessons learned and future challenges, Journal of Geophysical Research: Biogeosciences, 121 (3), 540-566, doi:10.1002/2015jg003120.

Lique, C., A. M. Treguier, M. Scheinert, and T. Penduff, 2009: A model-based study of ice and freshwater transport variability along both sides of Greenland, Climate Dynamics, 33 (5), 685-705, doi:10.1007/s00382-008-0510-7.

Lohmann, K., J. H. Jungclaus, D. Matei, J. Mignot, M. Menary, H. R. Langehaug, J. Ba, Y. Gao, O. H. Ottera, W. Park, and S. Lorenz, 2014: The role of subpolar deep water formation and Nordic Seas overflows in simulated multidecadal variability of the Atlantic meridional overturning circulation, Ocean Science, 10 (2), 227-241, doi:10.5194/os-10-227-2014.

Manucharyan, G. E., and M. A. Spall, 2016: Wind-driven freshwater buildup and release in the Beaufort Gyre constrained by mesoscale eddies, Geophysical Research Letters, 43 (1), 273-282, doi:10.1002/2015gl065957.

Manucharyan, G. E., M. A. Spall, and A. F. Thompson, 2016: A Theory of the Wind-Driven Beaufort Gyre Variability, Journal of Physical Oceanography, 46 (11), 3263-3278, doi:10.1175/Jpo-D-16-0091.1.

Marnela, M., B. Rudels, M. N. Houssais, A. Beszczynska-Möller, and P. B. Eriksson, 2013: Recirculation in the Fram Strait and transports of water in and north of the Fram Strait derived from CTD data, Ocean Science, 9 (3), 499-519, doi:10.5194/os-9-499-2013.

Marshall, J., Y. Kushner, D. Battisti, P. Chang, A. Czaja, R. Dickson, J. Hurrell, M. McCartney, R. Saravanan, and M. Visbeck, 2001: North Atlantic climate variability: Phenomena, impacts and mechanisms, International Journal of Climatology, 21 (15), 1863-1898, doi:10.1002/Joc.693.

Marshall, J., and F. Schott, 1999: Open-ocean convection: Observations, theory, and models, Reviews of Geophysics, 37 (1), 1-64, doi:10.1029/98rg02739.

Marshall, J., J. Scott, and A. Proshutinsky, 2017: "Climate response functions" for the Arctic Ocean: a proposed coordinated modelling experiment, Geoscientific Model Development, 10 (7), 2833-2848, doi:10.5194/gmd-10-2833-2017.

Marsland, S. J., H. Haak, J. H. Jungclaus, M. Latif, and F. Roske, 2003: The Max-Planck-Institute global ocean/sea ice model with orthogonal curvilinear coordinates, Ocean Modelling, 5 (2), 91-127, doi:10.1016/S1463-5003(02)00015-X.

Mauritzen, C., 2012: Arctic freshwater, Nature Geoscience, 5 (3), 162-164, doi:10.1038/ngeo1409.

Mauritzen, C., A. Melsom, and R. T. Sutton, 2012: Importance of density-compensated temperature change for deep North Atlantic Ocean heat uptake, Nature Geoscience, 5 (12), 905-910, doi:10.1038/NGEO1639.

Moreno-Chamarro, E., D. Zanchettin, K. Lohmann, and J. H. Jungclaus, 2017: An abrupt weakening of the subpolar gyre as trigger of Little Ice Age-type episodes, Climate Dynamics, 48 (3-4), 727-744, doi:10.1007/s00382-016-3106-7.

Morison, J., R. Kwok, C. Peralta-Ferriz, M. Alkire, I. Rigor, R. Andersen, and M. Steele, 2012: Changing Arctic Ocean freshwater pathways, Nature, 481, 66, doi:10.1038/nature10705.

Muilwijk, M., M. Ilicak, S. B. Cornish, S. Danilov, R. Gelderloos, R. Gerdes, V. Haid, T. W. N. Haine, H. L. Johnson, Y. Kostov, T. Kovács, C. Lique, J. M. Marson, P. G. Myers, J. Scott, L. H. Smedsrud, C. Talandier, and Q. Wang, 2019: Arctic Ocean response to Greenland Sea wind anomalies in a suite of model simulations, Journal of Geophysical Research: Oceans, 124, 6286-6233, doi:10.1029/2019JC015101.

Müller, W. A., D. Matei, M. Bersch, J. H. Jungclaus, H. Haak, K. Lohmann, G. P. Compo, P. D. Sardeshmukh, and J. Marotzke, 2014: A twentieth-century reanalysis forced ocean model to reconstruct the North Atlantic climate variation during the 1920s, Climate Dynamics, 44 (7), 1935-1955, doi:10.1007/s00382-014-2267-5.

Münchow, A., 2015: Volume and Freshwater Flux Observations from Nares Strait to the West of Greenland at Daily Time Scales from 2003 to 2009, Journal of Physical Oceanography, 46 (1), 141-157, doi:10.1175/JPO-D-15-0093.1.

Munk, W. H., 1950: On the wind-driven ocean circulation, Journal of Meteorology, 7 (2), 80-93, doi:10.1175/1520-0469(1950)007<0080:OTWDOC>2.0.CO;2.

Mysak, L. A., 2001: Oceanography - Patterns of Arctic circulation, Science, 293 (5533), 1269-1270, doi:10.1126/science.1064217.

Nansen, F., 1902: The oceanography of the North Polar Basin. The Norwegian North Polar Expedition 1893-1896, Scientific Results, 3 (9).

Notz, D., F. A. Haumann, H. Haak, J. H. Jungclaus, and J. Marotzke, 2013: Arctic sea-ice evolution as modeled by Max Planck Institute for Meteorology's Earth system model, Journal of Advances in Modeling Earth Systems, 5 (2), 173-194, doi:10.1002/jame.20016.

Peterson, I., J. Hamilton, S. Prinsenberg, and R. Pettipas, 2012: Wind-forcing of volume transport through Lancaster Sound, Journal of Geophysical Research: Oceans, 117 (C11), doi:10.1029/2012JC008140.

Prinsenberg, S. J., J. Hamilton, I. Peterson, and R. Pettipas (2009), Observing and interpreting the seasonal variability of the oceanographic fluxes passing through Lancaster Sound of the Canadian Arctic Archipelago, paper presented at Influence of Climate Change on the Changing Arctic and Sub-Arctic Conditions, Springer Netherlands, Dordrecht, 2009.

Proshutinsky, A. Y., R. H. Bourke, and F. A. McLaughlin, 2002: The role of the Beaufort Gyre in Arctic climate variability: Seasonal to decadal climate scales, Geophysical Research Letters, 29 (23), doi:10.1029/2002gl015847.

Proshutinsky, A. Y., D. Dukhovskoy, M.-L. Timmermans, R. Krishfield, and J. L. Bamber, 2015: Arctic circulation regimes, Philosophical Transactions of the Royal Society A: Mathematical, Physical and Engineering Sciences, 373 (2052), doi:10.1098/rsta.2014.0160

Proshutinsky, A. Y., and M. A. Johnson, 1997: Two circulation regimes of the wind driven Arctic Ocean, Journal of Geophysical Research: Oceans, 102 (C6), 12493-12514, doi:10.1029/97jc00738.

Proshutinsky, A. Y., R. Krishfield, M.-L. Timmermans, J. Toole, E. Carmack, F. McLaughlin, W. J. Williams, S. Zimmermann, M. Itoh, and K. Shimada, 2009: Beaufort Gyre freshwater reservoir: State and variability from observations, Journal of Geophysical Research: Oceans, 114 (C1), doi:10.1029/2008JC005104.

Proshutinsky, A. Y., I. V. Polyakov, and M. A. Johnson, 1999: Climate states and variability of Arctic ice and water dynamics during 1946-1997, Polar Research, 18 (2), 135-142, doi:10.1111/J.1751-8369.1999.Tb00285.X.

Rabe, B., P. A. Dodd, E. Hansen, E. Falck, U. Schauer, A. Mackensen, A. Beszczynska-Moller, G. Kattner, E. J. Rohling, and K. Cox, 2013: Liquid export of Arctic freshwater components through the Fram Strait 1998-2011, Ocean Science, 9 (1), 91-109, doi:10.5194/os-9-91-2013.

Rabe, B., M. Karcher, F. Kauker, U. Schauer, J. M. Toole, R. A. Krishfield, S. Pisarev, T. Kikuchi, and J. Su, 2014: Arctic Ocean basin liquid freshwater storage trend 1992-2012, Geophysical Research Letters, 41 (3), 961-968, doi:10.1002/2013GL058121.

Rogers, J. C., and M. J. McHugh, 2002: On the separability of the North Atlantic oscillation and Arctic oscillation, Climate Dynamics, 19 (7), 599-608, doi:10.1007/s00382-002-0247-7.

Rossby, T., 1996: The North Atlantic Current and surrounding waters: At the crossroads, Reviews of Geophysics, 34 (4), 463-481, doi:10.1029/96RG02214.

Rudels, B., 2009, Arctic Ocean Circulation, in Encyclopedia of Ocean Sciences, edited by J. H. Steele, K. K. Turekian and S. A. Thorpe, pp. 211-225, Elsevier, doi:10.1016/B978-012374473-9.00601-9.

Rudels, B., G. Björk, J. Nilsson, P. Winsor, I. Lake, and C. Nohr, 2005: The interaction between waters from the Arctic Ocean and the Nordic Seas north of Fram Strait and along the East Greenland Current: results from the Arctic Ocean-02 Oden expedition, Journal of Marine Systems, 55 (1), 1-30, doi:10.1016/j.jmarsys.2004.06.008.

Rudels, B., and D. Quadfasel, 1991: Convection and deep water formation in the Arctic Ocean-Greenland Sea System, Journal of Marine Systems, 2 (3), 435-450, doi:10.1016/0924-7963(91)90045-V.

Saha, S., S. Moorthi, H. L. Pan, X. R. Wu, J. D. Wang, S. Nadiga, P. Tripp, R. Kistler, J. Woollen, D. Behringer, H. X. Liu, D. Stokes, R. Grumbine, G. Gayno, J. Wang, Y. T. Hou, H. Y. Chuang, H. M. H. Juang, J. Sela, M. Iredell, R. Treadon, D. Kleist, P. Van Delst, D. Keyser, J. Derber, M. Ek, J. Meng, H. L. Wei, R. Q. Yang, S. Lord, H. Van den Dool, A. Kumar, W. Q. Wang, C. Long, M. Chelliah, Y. Xue, B. Y. Huang, J. K. Schemm, W. Ebisuzaki, R. Lin, P. P. Xie, M. Y. Chen, S. T. Zhou, W. Higgins, C. Z. Zou, Q. H. Liu, Y. Chen, Y. Han, L. Cucurull, R. W. Reynolds, G. Rutledge, and M. Goldberg, 2010: The Ncep Climate Forecast System Reanalysis, Bulletin of the American Meteorological Society, 91 (8), 1015-1057, doi:10.1175/2010BAMS3001.1.

Schmitz, W. J., 1996: On the world ocean circulation: Volume I, Some global features / North Atlantic Circulation, WHOI-96-03, Woods Hole Oceanographic Institution.

Schulzweida, U., 2017: CDO User Guide, Version 1.8.1, Max Planck Institute for Meteorology.

Serreze, M. C., and A. P. Barrett, 2011: Characteristics of the Beaufort Sea High, Journal of Climate, 24 (1), 159-182, doi:10.1175/2010JCLI3636.1.

Serreze, M. C., A. P. Barrett, A. G. Slater, R. A. Woodgate, K. Aagaard, R. B. Lammers, M. Steele, R. Moritz, M. Meredith, and C. M. Lee, 2006: The large-scale freshwater cycle of the Arctic, Journal of Geophysical Research: Oceans, 111 (C11), doi:10.1029/2005JC003424.

Skagseth, Ø., 2008: Recirculation of Atlantic Water in the western Barents Sea, Geophysical Research Letters, 35 (11), doi:10.1029/2008GL033785.

Smedsrud, L. H., R. Ingvaldsen, J. E. Ø. Nilsen, and Ø. Skagseth, 2010: Heat in the Barents Sea: transport, storage, and surface fluxes, Ocean Science, 6 (1), 219-234, doi:10.5194/os-6-219-2010.

Spreen, G., S. Kern, D. Stammer, and E. Hansen, 2009: Fram Strait sea ice volume export estimated between 2003 and 2008 from satellite data, Geophysical Research Letters, 36, doi:10.1029/2009gl039591.

Steele, M., R. Morley, and W. Ermold, 2001: PHC: A Global Ocean Hydrography with a High-Quality Arctic Ocean, Journal of Climate, 14 (9), 2079-2087, doi:10.1175/1520-0442(2001)014<2079:PAGOHW>2.0.CO;2.

Stevens, B., M. Giorgetta, M. Esch, T. Mauritsen, T. Crueger, S. Rast, M. Salzmann, H. Schmidt, J. Bader, K. Block, R. Brokopf, I. Fast, S. Kinne, L. Kornblueh, U. Lohmann, R. Pincus, T. Reichler, and E. Roeckner, 2013: Atmospheric component of the MPI-M Earth System Model: ECHAM6, Journal of Advances in Modeling Earth Systems, 5 (2), 146-172, doi:10.1002/jame.20015.

Stewart, K. D., and T. W. N. Haine, 2013: Wind-driven Arctic freshwater anomalies, Geophysical Research Letters, 40 (23), 6196-6201, doi:10.1002/2013gl058247.

Sverdrup, H. U., M. W. Johnson, and R. H. Fleming, 1942: The Oceans: Their physics, chemistry, and general biology, Prentice-Hall New York.

Thoma, M., R. Gerdes, R. J. Greatbatch, and H. Ding, 2015a: Partially coupled spin-up of the MPI-ESM: implementation and first results, Geoscientific Model Development, 8 (1), 51-68, doi:10.5194/gmd-8-51-2015.

Thoma, M., R. J. Greatbatch, C. Kadow, and R. Gerdes, 2015b: Decadal hindcasts initialized using observed surface wind stress: Evaluation and prediction out to 2024, Geophysical Research Letters, 42 (15), 6454-6461, doi:10.1002/2015GL064833.

Thompson, D. W. J., and J. M. Wallace, 1998: The Arctic Oscillation signature in the wintertime geopotential height and temperature fields, Geophysical Reserach Letters, 25 (9), 1297-1300, doi:10.1029/98gl00950.

Tietsche, S., D. Notz, J. H. Jungclaus, and J. Marotzke, 2013: Predictability of large interannual Arctic sea-ice anomalies, Climate Dynamics, 41 (9-10), 2511-2526, doi:10.1007/s00382-013-1698-8.

Tonboe, R. T., S. Eastwood, T. Lavergne, A. M. Sørensen, N. Rathmann, G. Dybkjær, L. T. Pedersen, J. L. Høyer, and S. Kern, 2016: The EUMETSAT sea ice concentration climate data record, The Cryosphere, 10 (5), 2275-2290, doi:10.5194/tc-10-2275-2016.

Tsubouchi, T., S. Bacon, A. C. N. Garabato, Y. Aksenov, S. W. Laxon, E. Fahrbach, A. Beszczynska-Moller, E. Hansen, C. M. Lee, and R. B. Ingvaldsen, 2012: The Arctic Ocean in summer: A quasi-synoptic inverse estimate of boundary fluxes and water mass transformation, Journal of Geophysical Research: Oceans, 117, doi:10.1029/2011jc007174.

Tyler, D. E., 1982: On the optimality of the simultaneous redundancy transformations, Psychometrika, 47 (1), 77-86, doi:10.1007/BF02293852.

Valcke, S., A. Claubel, D. Declat, and L. Terray, 2003: OASIS ocean atmosphere sea ice soil user's guide.

Vinje, T., 2001: Fram strait ice fluxes and atmospheric circulation: 1950-2000, Journal of Climate, 14 (16), 3508-3517, doi:10.1175/1520-0442(2001)014<3508:Fsifaa>2.0.Co;2.

Voet, G., D. Quadfasel, K. A. Mork, and H. Søiland, 2010: The mid-depth circulation of the Nordic Seas derived from profiling float observations, Tellus A: Dynamic Meteorology and Oceanography, 62 (4), 516-529, doi:10.1111/j.1600-0870.2009.00444.x.

von Storch, H., and F. W. Zwiers, 1998: Statistical Analysis in Climate Research, Cambridge University Press.

Wang, X. L., F. W. Zwiers, and V. R. Swail, 2004: North Atlantic Ocean Wave Climate Change Scenarios for the Twenty-First Century, Journal of Climate, 17 (12), 2368-2383, doi:10.1175/1520-0442(2004)017<2368:NAOWCC>2.0.CO;2.

Wang, Z. L., J. Hamilton, and J. Su, 2017: Variations in freshwater pathways from the Arctic Ocean into the North Atlantic Ocean, Progress in Oceanography, 155, 54-73, doi:10.1016/j.pocean.2017.05.012.

Woodgate, R. A., 2018: Increases in the Pacific inflow to the Arctic from 1990 to 2015, and insights into seasonal trends and driving mechanisms from year-round Bering Strait mooring data, Progress in Oceanography, 160, 124-154, doi:10.1016/j.pocean.2017.12.007.

Wu, B. Y., J. Wang, and J. E. Walsh, 2006: Dipole anomaly in the winter Arctic atmosphere and its association with sea ice motion, Journal of Climate, 19 (2), 210-225, doi:10.1175/Jcli3619.1.

Wu, P., and R. Wood, 2008: Convection induced long term freshening of the subpolar North Atlantic Ocean, Climate Dynamics, 31 (7), 941-956, doi:10.1007/s00382-008-0370-1.

Yang, J., 2006: The Seasonal Variability of the Arctic Ocean Ekman Transport and Its Role in the Mixed Layer Heat and Salt Fluxes, Journal of Climate, 19 (20), 5366-5387, doi:10.1175/JCLI3892.1.

Zhang, J. L., M. Steele, K. Runciman, S. Dewey, J. Morison, C. Lee, L. Rainville, S. Cole, R. Krishfield, M. L. Timmermans, and J. Toole, 2016: The Beaufort Gyre intensification and stabilization: A model-observation synthesis, Journal of Geophysical Research: Oceans, 121 (11), 7933-7952, doi:10.1002/2016jc012196.

Zhang, X. D., M. Ikeda, and J. E. Walsh, 2003: Arctic sea ice and freshwater changes driven by the atmospheric leading mode in a coupled sea ice-ocean model, Journal of Climate, 16 (13), 2159-2177, doi:10.1175/2758.1.

Appendix

Appendix A – Empirical Orthogonal Function Analysis

The following basic introduction of the EOF analysis is taken from von Storch and Zwiers (1998) who also gives an exhaustive description of the method and provide details about its calculation.

The basic concept of the EOF analysis is to describe the variability of a random vector $\vec{X}$ with dimension m. The time variability of $\vec{X}$, written as $\vec{X}'_t = \vec{X}_t - \hat{\vec{\mu}}$, where $\hat{\vec{\mu}}$ is the time mean of $\vec{X}$, is expanded into a finite series

$$\vec{X}'_t = \sum_{i=1}^{k} \hat{\alpha}_{i,t} \hat{\vec{e}}^i \qquad (A.1)$$

with time coefficients $\hat{\alpha}_{i,t}$ and fixed patterns $\hat{\vec{e}}^i$. The variance of $\hat{\alpha}_{i,t}$ usually decreases quickly with increasing index i, therefore a sufficient approximation of the equation is usually possible for $k << m$. The patterns are chosen to be orthogonal so that optimal coefficients $\hat{\alpha}_{i,t}$ are obtained by simply projecting the anomalies $\vec{X}'_t$ onto the patterns $\hat{\vec{e}}^i$. The patterns are specified such that the error $\sum_t (\vec{X}'_t - \sum_{i=1}^{k} \hat{\alpha}_{i,t} \hat{\vec{e}}^i)$ is minimal. The lag-0 sample cross-correlations of the optimal time coefficients are all zero ($\sum_t \hat{\alpha}_{i,t} \hat{\alpha}_{j,t} = 0$ for $i \neq j$).

The patterns $\hat{\vec{e}}^i$ are the estimated Empirical Orthogonal Functions, and the coefficients $\hat{\alpha}_i$ are the EOF coefficients or principal components. For every i, each expansion $\vec{Y}_t = \hat{\alpha}_{i,t} \hat{\vec{e}}^i$ represents $p\%$ of the variance of $\vec{X}$, which means that the variance of $\vec{Y}_t - \vec{X}$ is $(100 - p)\%$ of the variance of $\vec{X}$.

The interpretation of the results is that the first EOF $\hat{\vec{e}}^1$ of $\vec{X}$ gives the scalar product $\vec{X}^T \vec{e}^1$ of elements of $\vec{X}$ with the greatest variance. The second EOF $\hat{\vec{e}}^2$ provides the scalar product $\vec{X}^T \vec{e}^2$ with greatest variance that is uncorrelated with $\vec{X}^T \vec{e}^1$, and so on.

In this study, the EOF analysis was performed using the Climate Data Operators (CDO) package of Schulzweida (2017). CDO defines the EOFs as the eigenvectors of the covariance matrix of $\vec{X}'_t$, and the principal coefficients are calculated as the projection of an EOF onto a time step of $\vec{X}'_t$. In this study, the eigenvectors are presented in their weighted forms; that is, the EOF patterns carry the units of $\vec{X}$, and represent a 'typical'

anomaly pattern related to a standard change in their principal coefficients, whose time series are presented in a normalized form.

Appendix B – Redundancy Analysis

The EOF analysis is a powerful tool to identify dominant patterns in sea level pressure; however, these patterns represent the major statistical modes of its variability, and they do not necessarily correspond to those modes of sea level pressure variability that are best connected to changes in freshwater content. In order to identify such patterns, a method should be used that is able to take into account the freshwater variability too. There are different statistical methods that allow such investigation, for example the Canonical Correlation Analysis (CAA) or the Singular Value Decomposition (SVD) analysis.

As von Storch and Zwiers (1998) write, the EOF analysis is used to study the variability of a vector $\vec{X}$, but the CAA is used to analyze the correlation structure of a pair of vectors $\vec{X}$ and $\vec{Y}$. The objective of the CAA is to identify a pair of patterns $\vec{e}_X^1$ and $\vec{e}_Y^1$ so that the correlation between the scalar products $\vec{X}^T \vec{e}_X^1$ and $\vec{Y}^T \vec{e}_Y^1$ is maximized. The second pair of patterns $\vec{e}_X^2$ and $\vec{e}_Y^2$ is found so that $\vec{X}^T \vec{e}_X^2$ and $\vec{Y}^T \vec{e}_Y^2$ are the most strongly correlated scalar products of $\vec{X}$ and $\vec{Y}$ that are not correlated with $\vec{X}^T \vec{e}_X^1$ and $\vec{Y}^T \vec{e}_Y^1$, and so on. The SVD analysis is very similar, but there what is maximized is the covariance of $\vec{X}^T \vec{e}_X^1$ and $\vec{Y}^T \vec{e}_Y^1$.

However, CAA and SVD treats both variables equally. This means that for this study, where the aim is to identify patterns in sea level pressure (the predictor) that drive the changes in freshwater content (the predictand), these methods are still of suboptimal use. If the objective is a prediction, then the properties of the predictor patterns, such as the variance of the predictor, are irrelevant. The ideal result is those modes of the predictor, that are most tightly linked to the main modes of the predictand variability. This can be achieved by performing a Redundancy Analysis.

The Redundancy Analysis (RDA) was developed by Tyler (1982). The method can be used to identify pairs of predictor and predictand patterns that are strongly linked through a regression model, while maximizing the predictand variance. The RDA was introduced to climate research by von Storch and Zwiers (1998), and since has been applied to study the link between the variability of sea level pressure and other parameters (Kauker and Meier, 2003; Wang et al., 2004; Bakalian et al., 2010). The following brief introduction is taken from von Storch and Zwiers (1998).

Let us consider a predictor $\vec{X}$ with dimension m_X, and a predictand $\vec{Y}$ with dimension m_Y. Let us assume further that there is a linear operator represented by an $m_X \times k$ matrix Q_k. How much variance in $\vec{Y}$ can be accounted for by a regression of $Q_k^T \vec{X}$ on $\vec{Y}$? The regression model that relates $Q_k^T \vec{X}$ is given by

$$\vec{Y} = R(Q_k^T \vec{X}) + \vec{\epsilon} \tag{A.2}$$

where R is an $m_Y \times k$ matrix of regression coefficients. The variance represented by $(Q_k^T \vec{X})$ is maximized when $R = \Sigma_{Y,QX}(\Sigma_{QX,QX})^{-1}$, where $\Sigma_{Y,QX} = \text{Cov}(\vec{Y}, Q_k^T \vec{X}) = \Sigma_{Y,X} Q_k$ and $\Sigma_{QX,QX} = Q_k^T \Sigma_{X,X} Q_k$. Tyler (1982) named the proportion of variance represented by the above regression the redundancy index, and labeled it as follows:

$$R^2(\vec{Y}: Q_k^T \vec{X}) = \frac{\text{tr}\left(\text{Cov}(\vec{Y}, \vec{Y}) - \text{Cov}\left(\vec{Y} - \widehat{\vec{Y}}, \vec{Y} - \widehat{\vec{Y}}\right)\right)}{\text{tr}\left(\text{Cov}(\vec{Y}, \vec{Y})\right)} \tag{A.3}$$

where $\widehat{\vec{Y}}$ is the estimated value of $\vec{Y}$. The redundancy index $R^2(\vec{Y}: Q_k^T \vec{X})$ is considered as a measure of how redundant the information in the predictand is, if only the information provided by the predictor is known. Or in other words, it is the maximized (for any $k = 1, \ldots, \min(m_X, m_Y)$) amount of $\vec{Y}$ variance explained through the regression of $B_k^T \vec{X}$ on $\vec{Y}$, where the matrix B_k contains the first k columns of B, for which there is a non-singular transformation $B = (\vec{b}^1 | \vec{b}^2 | \ldots | \vec{b}^{m_X})$.

The redundancy analysis determines the k-dimensional subspace that allows for the most efficient regression on $\vec{Y}$ by identifying a B_k that maximizes R^2 for every k. Moreover, a second set of patterns $A = (\vec{a}^1 | \vec{a}^2 | \ldots | \vec{a}^k)$ can be identified that represent an orthogonal partitioning of the variance of $\vec{Y}$ that is accounted for by the regression of $\vec{X}$ on $\vec{Y}$, such that

$$\text{Cov}(B^T \vec{X}, B^T \vec{X},) = I \tag{A.4}$$

$$\text{Cov}(A^T \vec{Y}, B^T \vec{X},) = D \tag{A.5}$$

where D is a diagonal matrix of $m_Y \times m_X$ dimension with elements $d_{jj} = \sqrt{\lambda_j}$ for every $j \le \min(m_X, m_Y)$. The equations can be rewritten as two eigen-equations:

$$\Sigma_{YX} \Sigma_{XX}^{-1} \Sigma_{XY} \vec{a}^j = \lambda_j \vec{a}^j \tag{A.6}$$

$$\Sigma_{XX}^{-1} \Sigma_{XY} \Sigma_{YX} \vec{b}^j = \lambda_j \vec{b}^j \tag{A.7}$$

The final theorem given by Tyler (1982) states that the redundancy index $R^2(\vec{Y}: Q_k^T \vec{X})$ is maximized by setting $Q_k = B_k$, where B_k is the $m_X \times k$ matrix that contains the k eigenvectors satisfying equation (A.5) that correspond to the k largest eigenvalues. This statement holds for all $k \le m_X$.

Since B is non-singular, $\vec{X}$ can be expanded as

$$\vec{X} = \sum_{j=1}^{m_X} (\vec{X}^T \vec{b}^j) \vec{p}^j \tag{A.8}$$

where the adjoint patterns $P = (\vec{p}^1|\vec{p}^2|\ldots|\vec{p}^{m_X})$ are given by $P^T = B^{-1}$. Similarly, since A is orthonormal, $\widehat{\vec{Y}}$ (the part of $\vec{Y}$ that can be represented by $\vec{X}$) can be expanded as

$$\widehat{\vec{Y}} = \sum_j \left(\widehat{\vec{Y}}^T \vec{a}^j \right) \vec{a}^j \tag{A.9}$$

for which the expansion coefficients are given by

$$\widehat{\vec{Y}}^T \vec{a}^j = \sqrt{\lambda_j} \vec{X}^T \vec{b}^j \tag{A.10}$$

In summary, the redundancy analysis can be used to find the best predicted components of $\vec{Y}$ by identifying the eigenvectors $\vec{a}$ of $\Sigma_{YX} \Sigma_{XX}^{-1} \Sigma_{XY}$, and then finding the patterns $\vec{p}$ of $\vec{X}$ variations that carry this information. For this study, it means that it can provide an efficient way of specifying the maximum of variance in freshwater content from the information contained in the sea level pressure field, and can also specify pairs of patterns that are mapped onto each other, and thus can be considered redundant.

For this study, the predictor vector $\vec{X}$ was chosen as the time-varying spatial distribution of sea level pressure north of 20°N, and the predictand vector $\vec{Y}$ as of Arctic and North Atlantic freshwater content. The number of columns (patterns) in the matrix Q_k was constructed with $k = 20$ columns (patterns) by an EOF truncation. This is much smaller than the dimension of the predictor $\vec{X}$, therefore its phase space represented by the operation $\vec{X} \rightarrow Q_k^T \vec{X}$ was reduced.

Acknowledgements

Finally, I would like to express my gratitude to my family for their moral support. The most special thanks go to Evgenia Galytska. Without your motivation I never would have challenged myself to start this project. Thank you for your unconditional support and for always believing in me.